Cranfield University

Naseem Akhtar

Control System Development for Autonomous Soaring

School of Engineering

PhD Thesis

Cranfield University

Department of Aerospace Sciences
School of Engineering

PhD Thesis

Academic Year 2010-11

Naseem Akhtar

Control System Development for Autonomous Soaring

Supervisor(s): Dr Alastair K. Cooke and Dr James F. Whidborne

January 2010

Abstract

Thermal and dynamic soaring are two techniques commonly used by birds to extract energy from the atmosphere. This enables them to reduce, energy used during flight and increases their endurance. The thermal soaring technique involves extraction of energy from thermal updrafts and in dynamic soaring energy is extracted from wind shear. These techniques are investigated in this thesis using point mass and non-linear 6DoF models of an unmanned powered sailplane.

The key challenges of autonomous thermal soaring are the ability to identify remote thermal activity using on-board sensors and to position correctly in a thermal. In dynamic soaring, a real-time fuel saving trajectory generation technique along with a trajectory following control system is needed.

A hand held IR camera was used to assess the feasibility to observe hot spots associated with thermals. The thermal positioning capability was demonstrated in a 6DoF model using a positioning algorithm. The inverse Dynamics Virtual Domain (IDVD) technique was used to generate real-time trajectories for dynamic soaring applications using a point mass model of a powered unmanned sailplane and the fuel saving trajectories were validated using a high fidelity 6DoF model and a classical controller.

An important outcome of the research is the fact that energy saved during dynamic soaring flight was also realized due to a sinusoidal manoeuvre using reduced thrust. In this manoeuvre the kinetic energy is converted into potential energy by gaining altitude and by reducing airspeed. Then initial values of altitude and speed are gained by loosing the altitude. In this process a horizontal distance is travelled by using reduced thrust.

Acknowledgements

I would like to thank my supervisor Dr Alastair Cooke and co-supervisor Dr James Whidborne for their guidance and support throughout my PhD studies. I am also indebted to Dr Alastair Cooke for arranging Strategy Courses at the Cranfield Management School and also various Engineering Courses for my professional development. Dr James Whidborne provided me invaluable support in understanding real-time trajectory generation and controller synthesis methods.

I am also grateful to BAE Systems and EPSRC for funding the PhD.

At the end I would like to thank my family members, specially my mother and brothers for continuous support during my PhD. My wife Erem helped me with proof reading and also showed a lot of patience during PhD studies. My son Badar and daughter Huma also showed a lot of support by allowing me to work over the weekends.

Contents

List of Tables

List of Figures

Symbols

A	Coefficient of non linear wind model polynomial, reference area.
a	Core radius of thermal.
$a_{x_{0...7}}$	Coefficients of the polynomial.
c	Cosine.
C	Coefficient.
D	Drag, Transformation matrix, diameter of propeller.
d_p	Distance from the centre of thermal.
$dist_x$	Horizontal distance from the center of the thermal.
dy	Length of the section for the strip element.
$d(th/w(y))$	Distance between the center of thermal to the middle of any wing section with length dy.
$\bar{e}_T$	The normalized total air relative energy.
$\dot{\bar{e}}_T$	The normalized energy rates.
E	Air relative energy.
$\bar{E}$	Normalised air relative energy.
G	Wind gradient.
g	Acceleration due to gravity.
h	Altitude gained.
$\bar{h}$	Normalised altitude.
h_{tr}	Transition altitude.
K	Gain.
L	Lift.
m	Mass.
$N_p(w)$	Cross derivative.
$N_r(w)$	Damping in yaw derivative.
n	Load factor.
N	RPM of engine.
p	roll rate.
P	Angular velocity, position, power.
R	Radius.
r	Radial distance.
r_{TH}	Thermal radius.
s	Sine.
S	Wing span.
T	Time constant, thrust.
t	Time.
τ	The virtual arc.
u	Forward component of induced speed.
v	Lateral component of induced speed.
V	Speed.

w	Normal component of induced speed.
W	Weight of sailplane, wind speed.
x, y, h	Position relative to earth axis.
X	Vector of known value sequences.
y	Span wise location.
Y	Vector of measurement sequences.

α	Angle of attack.
θ	Angle of pitch.
ϕ	Angle of bank.
ρ	Air density.
β	Angle of side-slip.
λ	Speed factor.
ς	Bank command.
Γ	Circulation of air in thermal.
ϵ	Error.
γ	Flight path angle.
ψ	Heading angle.
$\dot{(\cdot)}$	Normalized derivatives.
$\bar{\rho}$	Normalized wind shear parameter.
σ	Normalized time.
η	Planes parallel to the thermal core, efficiency factor, pitch command.
ζ	Rudder command.
ξ	Roll command.
Θ	Vector of unknowns.
$\widehat{\Theta}$	Estimate of unknowns.

Subscripts

alt	Altitude.
a	Actuator.
ari	Interlink gain between heading and rudder command.
be	Body to earth axis.
c	Climb.
cg	Center of gravity.
D	Drag, Transformation matrix.
D_0	Zero Lift Drag.
E	Earth axis.
e	Effective velocity.
eb	Earth to body axis.
f	Final.

g	Gravity, geometric.
I	Induced, integral.
L	Lift.
N	North axis.
opt	Optimal.
0	Initial.
p	Proportional, point roll rate.
q	Pitch rate.
r	Dihedral.
S	Sink.
T	Total.
t	Trajectory.
tr	Transition.
TH	Thermal.
th	Up draft.
u	UAV.
We	Wing coordinates.
w	Wing.
$x_{0...7}$	No of coefficients.
y	Strip element.
Λ	Dihedral.

Superscripts

e	Earth.
b	Body.

Chapter 1

Introduction

1.1 Project Background

A previous study of autonomous soaring undertaken by Cook [CCW06] demonstrated the feasibility of an energy extraction controller. It was recommended that for optimal energy management, the remote thermal sensing and autonomous soaring control functions should be integrated with a total energy variometer to develop an integrated control system.

The research described in this thesis, builds on the previous work of Cook and Amrane [Amr05] and demonstrates an autonomous soaring capability in a simulated environment. A 6DoF model of a high performance sailplane was used. The key to this was a representative mathematical model of atmospheric thermal lift, the aerodynamic interaction between the air vehicle wing and rising column of air. This model was developed by Amrane [Amr05]. A positioning algorithm was extensively tested in the simulated environment that autonomously positions a sailplane in a thermal.

A dynamic soaring capability was also demonstrated by using the IDVD (Inverse Dynamics Virtual Domain) method, that generated fuel saving trajectories in real-time. The trajectories were then followed in the 6DoF model using a trajectory following controller.

The success of an autonomous thermal soaring system depends on the system's ability to detect and locate atmospheric thermal activity remotely. An infra red camera was used to observe hot spots associated with the built up areas, greenery, trees and clouds etc. An ability to identify greenery and motorway using visual sensors and an IR camera along with an on-board pattern recognition system has been demonstrated[1].

1.2 Problem Description

The key problems associated with autonomous thermal soaring and dynamic soaring capability development are:

[1] In collaboration with the Applied Maths and Computing Group

- Detection of the thermal activity by identifying landmarks and clouds associated with thermals by using on-board sensors and image recognition capability.
- Using appropriate thermal model in 6DoF simulations.
- Autonomous positioning of an unmanned sailplane in a thermal.
- A real-time trajectory generation technique for dynamic soaring applications.
- Estimation of the wind shear strength and wind direction for dynamic soaring applications.
- A trajectory following controller, which can track the fuel-saving trajectories.

‘

1.3 Objectives

The objectives of the project can be summarized as:

- Testing of IR sensors system and demonstrating its capability in hot spots detection.
- Identification and use of appropriate thermal models.
- Use of a realistic model of atmospheric thermals in 6DoF simulations.
- A real-time trajectory generation technique for dynamic soaring, and also ability to estimate wind shear and wind direction.
- An optimal atmospheric energy management control system for autonomous soaring applications.

1.4 Methodology

1.4.1 Thermal Soaring

1.4.1.1 Positioning Algorithm

An algorithm based on the Piggott [Pig95] method was used to autonomously position the unmanned sailplane in a thermal. Logic was introduced to work out the orientation of the sailplane relative to the thermal centre. Which helped to turn it in the right direction once a thermal had been identified by a variometer. The algorithm was also designed to reposition the sailplane should the thermal be lost while it was trying to execute turns.

1.4.1.2 Integrated Atmospheric Energy Control System

Classical control methods were used to design the soaring control system which was integrated with a variometer. The controller would follow bank angle and speed commands generated by the positioning algorithm. The inner stability augmentation loop of the controller was based on the work of Cook [CCW06] and the bank and speed controller were based on a PI control scheme.

1.4.1.3 6DoF Model

A 6DoF model developed by Amrane [Amr05] was used. A soaring controller was added with an ability to position the sailplane in a thermal and to follow fuel saving trajectories. The model was extensively used for testing thermal soaring capability and for validation of the fuel saving trajectories obtained from the optimization program using the point mass model.

1.4.2 Dynamic Soaring

1.4.2.1 Fuel Saving Trajectories Generation

The IDVD (Inverse Domain Virtual Dynamics) approach [Yak00] was used to generate trajectories by means of polynomials where the boundary conditions were specified and a jerk parameter was introduced for additional flexibility. The control inputs were determined from the inverse dynamics. This method can rapidly generate the trajectories and would be suitable for real-time dynamic soaring applications because numerical integration of the equations of motion is avoided.

1.4.2.2 Trajectory Following Controller

The trajectory following controller was designed using classical control methods. It follows the trajectories generated by the optimization program. The off and along-track errors are controlled by using bank and speed controllers and the altitude error is passed to an attitude controller.

1.5 Thesis Outline

A literature review is provided in Chapter 2, that covers the techniques used in this thesis and also describes the relevant work done by other researchers including thermal soaring, dynamic soaring and sinusoidal cruising techniques.

Chapter 3 describes the proposed architecture for thermal soaring and the results of an IR field trial. In Chapter 4, atmospheric thermals, thermal models, two dimensional strip theory to determine the impact of thermals on the sailplane and soaring controller are described.

In Chapter 5 results of dynamic soaring are described. The IDVD technique along with the wind shear model used and results for crosswind travelling and loitering are described.

In Chapter 6, the 6DoF model is described and all the changes made in the model are explained in detail. The changes include, controller, wind effects, wind model, thermal model and airfoil drag. The results of thermals soaring and validation of fuel saving trajectories using the 6DoF model are also presented. Conclusions, future work and contribution to knowledge are presented in Chapter 7. The nomenclature section in the beginning of the thesis applies for the main body of the thesis and not all the appendices.

1.6 Contributions to Knowledge

The contributions to knowledge was made in the following areas:

An architecture for the autonomous thermal soaring was recommended that integrates the image recognition capability with an autopilot, positioning algorithm and a variometer. The positioning algorithm with a turning logic was tested in at least two sizes of thermals and extracted energy by positioning the sailplane in thermals. The sailplane was made to approach thermals from the centre, left and right sides. A sophisticated 6DoF aerodynamic model of the sailplane that calculated the impact of thermals on the wing sections using two dimensional strip theory was used for the positioning algorithm testing.

Estimated wind heading and strength in real-time using least squares method for trajectory generation applications. The IDVD technique resulted in rapid generation of trajectories so this method is suitable for real-time applications. The sailplane extracted energy from wind shear and saved fuel in crosswind, loitering, upwind and downwind modes. Results of the fuel saving trajectories generated using a point mass model were validated by using the non-linear 6DoF model of the sailplane.

An interesting outcome of the results included the sinusoidal cruise technique that results in lower fuel consumption for UAVs. This technique does not require thermals or wind gradients and is also applicable to fighter jets and large aeroplanes.

1.7 Patent and Publications

A patent filing process has been initiated for a fuel saving system that is applicable to UAVs, missiles and military aeroplanes.

The following publications have been presented:

1. N. Akhtar, A.K. Cooke, and J.F. Whidborne. Fuel saving benefits of soaring UAVs. *Cranfield Multi-strand Conference*, Cranfield, U.K., May 2008.

2. N. Akhtar, J.F. Whidborne, and A.K. Cooke. Real-time trajectory generation technique for dynamic soaring UAVs. *UKACC Int. Conf. CONTROL 2008*, CDROM paper 115, Manchester, U.K., September 2008.

3. N. Akhtar, J.F. Whidborne, and A.K. Cooke. Wind shear energy extraction using dynamic soaring techniques. *Proc 47th AIAA Aerospace Sciences Meeting*, Orlando, FA, January 2009.

4. N. Akhtar, A.K. Cooke, and J.F. Whidborne. An integrated control system for atmospheric energy extraction. *Proc 24th International Conference on Unmanned Air Vehicle Systems*, pages 33.1-33.11, Bristol, U.K., March 2009.

   The following publications are under preparation:

5. N.Akhtar, J.F. Whidborne and A.K. Cooke. Fuel saving techniques for UAVs in wind shear. *Submitted to Proc. IMechE J. Aero Eng.*

6. N.Akhtar, A.K. Cooke and J.F. Whidborne. A positioning algorithm for autonomous thermal soaring. *Submitted to Journal of Aircraft.*

7. N.Akhtar, T. Breckon, A.K. Cooke and J.F. Whidborne. A soaring controller architecture for high endurance UAVs. *Being prepared for The Aeronautical Journal.*

Chapter 2

Literature Review

In this chapter, the previous work done on thermal and dynamic soaring is briefly described. Thermal soaring models, positioning controllers, experiments to measure thermal strength and efforts to demonstrate autonomously soaring practically by using model aeroplanes are discussed. On dynamic soaring techniques, optimization methods and various control techniques for trajectory following along with simulation results are explained.

2.1 Thermal Soaring

Thermal soaring involves the extraction of energy from the atmosphere to gain altitude. The design and development of an efficient algorithm for autonomous soaring requires the construction of accurate models of the thermal structure as well as the sailplane.

2.1.1 Thermal Models and Structure

Carmichael models, that classify thermals as narrow/strong, narrow/weak and wide [Car54], have been widely used. An improved set of standard thermals obtained from a systematic analysis of numerous in-flight investigations was proposed by Hortsmann [Hor76]. These models are more realistic representations of typical European weather conditions. Although according to Thomas [Tho99] there is no unanimity of opinion concerning which are the most appropriate.

Laboratory experiments showed that motion of an isolated thermal resembles a vortex ring Woodward [Woo58]. It was written that the center of the thermal rises at 2.2 times the velocity of the thermal cap and the buoyant fluid at the edge moves downwards. Mixing with the outside air takes place as the thermal rises, approximately 60% at the front side and 40% at the rear. The thermal radius increases as it ascends and it takes the shape of a cone. Experiments also provided a detailed absolute thermal velocity distribution.

In this thesis, the Hortsmann model was is to calculate the suitable turn radius and speed within the thermal. These turn, bank and speed values were used to extract energy from Carmichael models. Then Carmichael model was populated with absolute velocities of updraft

determined experimentally by Woodward. The absolute values were used because a column structure of the thermal model was assumed.

A development of updraft model for autonomous soaring UAVs was described by Allen [All06]. The model was developed at NASA Dryden Flight Research Center by using balloon for surface measurements. The convective velocity statistical representation and the convective mixing layer thickness were created. Then updraft size, vertical velocity profile, spacing and maximum hight were worked out. The convective mixing-layer thickness is defined as the maximum height above ground that updrafts can reach. It was calculated using a predawn rawinsonde balloon data and measured ground temperatures. A typical height for the convective mixing layer thickness was determined to be 6000 m.

The meteorological aspects of thermals that can be used to design an efficient soaring aircraft were discussed in detail by Cone [Con61]. The performance equation in such thermals was also derived. He also described the motion of free thermals and mechanisms of equilibrium flight. Cone described the structure of vortex type thermal model and distribution of updraft as a function of the distance from the center and also its variation with the vertical distance from the center.

2.1.2 Applications of Two Dimensional Strip Theory

The effect of thermals on a sailplane within a 6-DoF model, using two dimensional strip theory was implemented by Amrane [Amr05]. A key part of this work was a representative mathematical model of atmospheric thermal lift, and the aerodynamic interaction between the air vehicle wing and the column of rising air. Cook [CCW06] described a control system architecture, which was used as the basis for the design of the soaring controller described in this thesis.

2.1.3 Thermal Soaring Simulation and Control

The atmospheric energy harnessing technique was looked at by Cowling [CRW+08]. He considered the hot spots developed by uneven heating of the known surface locations and used them in a guidance algorithm to increase the likelihood of encountering a thermal. To extract energy once a thermal has been located, a UAV must position itself in the thermal. Reichmann and Piggott's techniques for thermal centring using five different models of thermals were tested. It was found that success of a particular thermal centring technique depends on the response time of on board sensors. Five different thermal models used are, Cylindrical, Sinusoid, Simplified Bradbury Model, Gaussian, Complex Bradbury Model. A commercial glider simulation package was used to demonstrate the control architecture and simulate an autonomous flight.

A theoretical analysis of the stability and convergence of heuristic controller used for centring thermals was carried out by Andersson [AK09]. A thermal updraft field was represented by an exponential Gaussian function. The analysis provided the effect of varying feedback gains of the controller for various strengths and sizes of thermals.

A reinforced learning technique in the design of adaptive control system for soaring aircraft was used by Wharington [Wha98] in his thesis. The reinforcement learning was pursued by using self-optimizing control system. The control architecture shares features of both reinforcement learning and model predictive control. This controller was used to fly at the desired speed and also to maximize height gain. His work also included a specialized neural network used to estimate the size and location of thermals near the vehicle.

In the thesis a positioning algorithm was used to place the air vehicle in the thermal. The positioning algorithm had a logic that determined the orientation of the sailplane with respect to the thermal center and turned the sailplane towards the center on detection of the thermal. Further investigation using the thermal center estimation techniques has been recommended and this would provide comparison with the algorithm used in this project. In our simulations to test the positioning algorithm's capability a more sophisticated aerodynamic model of the air vehicle was used. This model used two dimensional strip theory for calculating the forces and moments induced by the thermal at individual strip of the wing.

An optimal energy-efficient flight trajectories of a generic UAV was calculated by Qi [QZ05]. The flights through a thermal are formulated as a non-linear optimal control problem that minimized the average thrust per unit of time. Fuel efficiencies of these optimal thermal soaring flights are compared with those without utilizing thermals. A significant improvements in fuel usage are achieved if thermals are used. An optimal control trajectory results if compared with the thermal soaring by positioning controller would be more meaningful as this would quantify the improvement in energy extraction by following optimal trajectories. To do that a more realistic thermal updraft model and thermal center information would be required. This could form part of the future work and once tested in the simulated environment it should be tested on a small model aeroplane to validate the results.

A novel convective air updraft locating and guidance algorithm for glider based unmanned aerial vehicle systems had been developed and implemented by Edwards [Edw08]. The local air vehicle motion was estimated using the vehicle energy rate of change and the vehicle speed polar. Initially updrafts were geo-located with a centroid-based center estimator using local air motion estimates. Then an improved estimation of the center was carried out using an adaptive grid. However he mentioned a need for remote thermal sensing of updrafts which will result in a wider data set that will help in locating center of updrafts. To save time, work on a high fidelity simulator was by-passed and effort was concentrated on flight testing.

2.1.4 Thermal Soaring Practical Demonstration

At NASA Dryden Flight Research Center, Allen [All06] used an electric-powered motor-glider with a wing span of 4.27 m. An outer loop soaring guidance and control was added in an auto pilot. The total energy of the aircraft was used for thermal detection and soaring. The guidance commands were generated using the estimated thermal size and position and static pressure sensor estimated the airspeed. The total energy obtained using the kinetic and potential energies was filtered to get a specific energy. The impact of motor energy was subtracted to account for the energy added by the aircraft motor. The energy acceleration

was also calculated. Thermal identification was carried out to estimate location, size and strength. The values of aircraft position and energy rates were stored. Thermal drift was calculated by position of the thermal given by the first set of entries with the last set of entries. The thermal vertical velocity was approximated from the aircraft energy rate history. It was assumed that the maximum thermal velocity is 10 percent greater than the maximum energy rate experienced. The radius of the thermal was estimated using a gradient descent method to fit an assumed thermal shape to the data collected. The predicted thermal velocity at each point was done by Wharington [Wha98] but modified to account for the environment sink rate. Then a measure of the fit between the assumed thermal shape and the stored measured energy rate values was carried out. The estimated thermal radius was limited between the values of 40m and 80m. This was done to avoid a high bank angles required in a small thermal and to make a soaring algorithm robust to the variations in position and strength of large thermal. The data in the queue was used to estimate the thermal center location using a Centroid equation. The estimation of the thermal radius was carried out using an iterative fit to an assumed thermal vertical profile.

A quantitative analysis of a small electric-powered UAV using thermals to increase its endurance was described by Allen [All06]. A three degree of freedom simulation was used to find out the yearly effect of thermals on the performance of the vehicles. Rawinsonde balloon measurements and surface radiation was used to find out the updraft size, strength, spacing, shape and maximum height for the simulation. The results showed an endurance of 14 hours achieved for a UAV with a nominal endurance of 12 hours in the summer and 8 hours in the winter. Goodwin [GEC06] explained a technique for turn of direction of a UAV to soar upon any vertical air caused by a ridge in an unknown environment.

Autonomous soaring using a surrogate manned sailplane showed the potential capability that soaring provides with in local atmosphere was explored by Irvine [IIB+07]. Ridge lift and thermal lift were considered to increase the endurance. The ridge lift exploration was based on a meteorological forecast of vertical air speeds at various altitude above points on an area of interest. The thermal search was conducted using observation and detection of clouds using a digital camera and its correlation with the tables of probabilities based on the land type. It was stressed that identification of falling air region was also required so it can be avoided.

The implementation details and flight test results of an autonomous soaring controller were provided by Edwards [Edw08]. An autonomous soaring glider using energy initially from a 140m launch covered over 48 km and stayed aloft for 1.5 hours, by using thermals. The vehicle energy rate change and the vehicle speed polar were used to estimate the vertical air movement. The local air motion estimates were used by a centroid based center estimator. An adaptive grid of nodes was created in real life. The node with highest non-linear regression correlation was chosen. This was done at each node by computing a curve fit parameter, as if the node was an actual thermal center. The node with the highest curve fit parameter was chosen as the new center and its value was saved.

An approach for planning long distance trajectories for small UAVs was described by Langelaan [Lan09]. A trajectory was found between start and finish point.

2.1.5 Thermal search Using On-board Sensors

The search for thermals requires on-board image recognition ability that can identify landmarks from IR and visual cameras. Dennis [DABL08] explored a vision based solution for sense and avoid system for small UAVs. The solution consisted using a small light weight, low power and commercially available camera, special purpose computational platform based on Helios and a custom FPGA based circuit board developed in Brigham Young University's Robotic Vision Laboratory. This system provides a significant computational power and has been successfully used on small ground vehicles, fixed wing aircraft and quad rotors. A MICRON MT9V023 CMOS image sensor was used on-board and connected to Helios via a custom daughter board. It used a global shutter which eliminates motion artefacts that show up in images from cameras that use rolling shutters. The detection algorithm detected an aeroplane in the scene, even in the presence of the background clutter. The algorithm also detected a semi-trailer truck.

A vision based real-time target localization for single antenna GPS guided UAV is used by Sohn [SLKK08]. A real-time method to calculate the three dimensional location of a fixed target using a gimballed camera on a UAV is proposed. The analog output from the camera is passed to the ground station. The image processing software was developed using the OpenCV, which is an open source library for computer vision.

In the thesis an architecture is recommended that uses on-board image processing capability that would identify landmarks associated with thermals and then would use a variometer to confirm the presence of thermals and a positioning algorithm would place the sailplane in the thermal.

A Doppler LIDAR to make the measurements of vertical wind of an atmospheric thermal was used by Koch [Koc05]. He presented a direct observation of a thermal structure. LIDAR operates at a short infra-red wavelength as opposed to radars that operate at long radio wavelengths. Radars are effective for the large target like birds and rain drops where as LIDARS are used for micrometer sized aerosol particles. The Doppler LIDAR measured the wind fields of a thermal. The thermal was 700m in height and 900m in horizontal extend. The horizontal wind speed of the thermal was 4m/s and vertical speed was 3m/s.

2.1.6 Multi-agent architecture for predicting soaring possibilities

A multi-agent architecture has been described by [HFPW07] to predict the soaring possibilities within the local atmosphere. A GPS and a radio modem fitted surrogate sailplane was used to receive ground based observation data about cloud formation and evolution. The multi-agent architecture could receive data from a variety of sources and use this data for journey planning.

A reasoning system used in reference [HFPW07] is based on an approach where multiple agents communicate with each other via a shared blackboard. The agents can be distributed on other airborne platforms and also on the ground based platforms. The blackboard agents

contains information about the sailplane itself, any peers, areas of lift, sink, ridges and boundaries of restricted areas. This agent can answer questions like what areas of thermal lift updraft exists between the path A to B?

The number of agents that interact with physical sensors on-board and pass results to the black board include:

1. GPS agent for monitoring location.
2. Altitude/climb/descent monitoring agent.
3. Battery energy monitoring agent.
4. Agent for lift prediction.
5. Thermal prediction agent.
6. Local knowledge agent.
7. Mission requirement agent.
8. Strategic planner agent.
9. Tactical planner agent.

The trials indicated that there was a good agreement between the areas where lift was predicted and the variometer display.

2.2 Dynamic Soaring

Dynamic soaring is a technique used by many species of birds, such as the albatross, to reduce their energy expenditure. Albatrosses travel great distances with very little wing flapping by exploiting the wind shear effect, which is particularly strong and consistent over the ocean, to extract energy from the atmosphere. To do this, the bird dives downwards to gain speed and to take energy out of the gradient, until it is very close to the water. It then makes a climbing turn into wind through the gradient until it is close to stall. The gain in airspeed from climbing into a progressively stronger wind tends to reduce the normal loss of speed associated with climbing [Pig95]. At the top of the climb, the bird turns downwind and repeats the cycle. This process is also used by glider pilots, albeit at high altitudes where wind gradients are less predictable. It is possible to maintain a ground position using this technique; travel laterally relative to the wind direction or even travel upwind.

Autonomous soaring flight had been looked at previously: in fact the first attempt to analyse the problem of albatross flight was made by Lord Rayleigh in 1883 [Ray83]. More recently, Kiceniuk [Kic01] proposed some heuristic techniques for the soaring trajectory, but Wharington [Wha04] concluded that it was very hard to obtain useful trajectories for autonomous soaring with this approach and recommended using optimal control methods.

2.2.1 Optimization Methods

Boslough [Bos02] proposed solving the problem using genetic algorithms. A simulated annealing method for parameter search was used by Wharington [Wha98]. The optimization procedure was found to be fast enough for off-line implementation, but such methods are generally regarded as being unsuitable for real-time applications.

The problem of optimizing trajectories for ridge soaring was considered by Sachs and da Costa [SC03]. The trajectories were constrained to follow an oval path, thus restricting the solution space. Similarly, Deittert and Toomer [DTP06] constrained the vehicle to fly a circular path, an even more restrictive constraint. However both strategies gave very promising results.

The most promising method for real-time implementation was provided by Zhao [Zha04a, Zha04b]. The optimal control problems were converted into parameter optimization with a collocation method and solved numerically using standard non-linear optimization software. However no indication of the efficiency of the methods was provided. The approach proposed in this project draws on Zhao in the modelling and problem formulation.

A new non linear guidance logic was worked on by Park [PDH04]. The method involved approximating a PID control when following a straight line having an element of anticipatory control for flight tracking when following curved paths.

The dynamic soaring was investigated by constraining the vehicle to fly circular trajectories by Deittert [DTP06]. He concluded that a UAV requires a high wind loading, needs to fly fast and turn hard and have a low zero lift drag coefficient for dynamic soaring. A chart of wing loadings and corresponding wind gradients are discussed. An albatross sized UAV will require a wind gradient in the area of 0.16/s to 0.25/s. Wind gradients of this size regularly appear in the earth's boundary layer. The largest wind gradients occur over city centres due to a large friction between air and the ground.

The trajectory optimization using differential flatness technique was also carried out by Deittert [DRTP09b]. The idea was to find a closed form of the system's inverse dynamics based on a new set of outputs. Numerical integration of the equation of the motion was also avoided. An albatross model was used to investigate the influence of maximum bank angle, minimum trajectory height, maximum airspeed, maximum lift coefficient and mass on the minimal and maximal wind conditions required using closed trajectories. The lift coefficient limit showed that minimum wind air speed requirement goes up for the lower values of C_{Lmax}. The maximum permissible wind strength increased when C_{Lmax} increased more than the value at which best glide ratio was achieved (0.578). The higher bank limit resulted in lower time to complete a trajectory. Less energy was lost to drag and as a result less energy was need to be extracted from the wind gradient. Bank angles of 70 to 90° were most desirable from the performance point of view. The dynamic soaring force grows linearly with the UAV airspeed and the reference wind speeds. The combination of increased airspeed limit and increased wind speed was able to compensate for the drag losses. Increasing the UAV wing loading resulted in improved maximal wind conditions up to a maximum value corresponding 7.5 kg mass and after that it reduced. The minimum wind conditions were achieved when a

mass of 3 kg was used. The amount of energy extracted and drag losses effect the values of maximal and minimal wind conditions. In the minimal wind conditions case, a higher mass values resulted in higher C_L values and this causes more induced drag. The reduction of the minimal at higher wing loadings was due to the increased induced drag. The dynamic soaring force's magnitude is linearly proportional to the UAVs mass and the reference wind speed [DRTP09b]. Therefore low mass values require a flight in high speed wind. The combination of these two effects result in the minima of the wind condition curve. In case of maximal wind conditions, strong winds require fast flying to compensate for the drift. However drag goes up and the flight becomes expensive in terms of energy. The extractable energy is limited at low mass values, and a UAV cannot fly in strong winds. However high mass values cause increase in drag because of lift coefficients are high. The drag depends on lift coefficient and airspeed and the combination of two results in high drag losses and hence reduce the maximal wind conditions.

For cross country trajectories, the maximal wind speeds for downwind direction are higher than the permissible wind speeds for the stationary trajectories.

The impact of turbulence on the dynamic soaring flight of a generic 3m wing span UAV was also investigated by Deittert [DRTP09a]. He also investigated the feasibility of controlled flight for wind speeds between 8 m/s and 24 m/s.

2.2.2 Decision Making Tools for Dynamic Soaring

A system for small UAVs for long distance travelling was described by Langelaan [Lan09]. A decision making tool consisted of a prediction of wind field with a trajectory planner, GPS, air data sensors and a low level flight controllers. Major focus was exploitation of slope or ridge lift and paper described a trajectory optimization method to utilize the vertical component of the wind.

2.2.3 Scope of PhD Work

A need was identified to after literature review that a sophisticated simulation that models the impact of thermals on a sailplane should be used to define the interaction between a thermal and a sailplane wing. Optimum values of a radius of turn, bank angle and speed should be calculated to maximise the energy extraction from an atmospheric thermal. These values along with a controller to detect a thermal centre and position a sailplane autonomously in thermal would be used in a simulated environment. A vision based system for autonomous thermal soaring applications should be investigated as most of the practical demonstration on thermal soaring was passed on flying a model aeroplane over a location with thermals. This project was funded by BAE Systems and their requirement was to use only passive sensors for thermals soaring applications and therefore it was decided to consider only visual and IR sensors.

In case of dynamic soaring a need was identified to use a real time technique for generating fuel saving trajectories in wind shear as the techniques mentioned in the literature could not

be used for real time applications. A more realistic quantification of the fuel saving benefits was required by comparing the fuel used when the same distance was covered by flying a UAV at a minimum drag speed. There was also a need to validate the fuel saving results in a more sophisticated 6DoF model by following the trajectories using point mass models. This validation was required to compare the results predicted and realized in 6DoF environment. To calculate fuel saving trajectories in real-time the values of wind gradient, wind speed and direction and these should be estimated before a UAV completes its current soaring cycle.

Chapter 3

Systems Architecture

3.1 Thermal Soaring Architecture

In this Chapter the various strands of technology that can be put together to form an autonomous thermal soaring system are described. The architecture was developed by first considering how pilots search for thermals and then identifying how the various steps could be automated using existing technology.

On a day when the sky is clear glider pilots look for landmarks typically associated with thermals such as crop fields or urbanised areas. Once located they fly over the area downwind of these landmarks. A variometer is then used to confirm the presence of a rising air mass. Glider pilots look for at the shapes of cumulus clouds for clues of thermal presence. Clouds that are triangular in shape indicate presence of thermals under them. As cumulus clouds evolve they become square in shape and finally inverse triangular in shape. Glider pilots ignore inverse triangular shaped clouds as thermals are no longer present under them. They also look for other soaring birds for clues. Once a triangular or squared shaped cloud is identified they circle there sailplanes underneath to search for thermals.

The architecture is shown in Figure 3.1. Existing vision based technology, using a combination of IR and visual cameras, would be used to detect urbanised areas at a range of approximately three miles.

Buildings of known height can be used to calculate how far a UAV is from them. This distance information is passed to the decision system that commands the autopilot to fly there for thermal search. Secondary sensor inputs are required for identifying and tracking clouds by using data from satellites and also from the ground based cloud tracking stations. Similarly global terrain database should be used to locate hills that are source of lift along with a database containing local area knowledge of places where likelihood of presence of thermals is high. IR sensors should detect whether conditions are right for thermal presence by identifying any hot spots. This information is again passed to the decision system and it decides by looking at all this information that indicate likelihood of thermal presence and then depending on the mission and fuel requirements could command a UAV to search for thermals, Figure 3.1.

The pattern recognition module identifies landmarks associated with thermals from images provided by IR and visual cameras. Once the landmarks have been identified this information is passed to the decision system module; which has secondary inputs that provide information about wind speed and direction, local terrain, weather and local areas where thermal likelihood is high. The secondary information could come from ground based stations. This information along with the operational requirements is used to send a command signal to a controller instructing it to either search for a thermal by circling or move to another location.

When thermal search command is received the sailplane using its on-board total energy variometer searches for a thermal. (A capability to identify objects in real time has been demonstrated by the image processing group at Cranfield University.)They have used on-board visual and IR cameras to identify objects by looking downward on the ground. The objects included cars, motor ways and greenery.

3.2 Variometer

A variometer is a very important sensor for soaring flight. It is used to measure rate of climb or descent by sensing the changes in atmospheric pressure caused by vertical motion[Pig95]. The instrument consists of a flow meter connected to an accumulator. While climbing, the atmospheric pressure drops and air flows out of the capacitor. However in the level flight the pressure in the accumulator equals the surrounding air, so no flow occurs and the variometer reads zero.

The mechanical instrument consists of a vane mounted on jewelled bearings. A hair spring is used to keep it centralized. As air flows in or out of the accumulator it is directed in a jet towards the vane causing it to move. The air escapes from the slots below the vane. The instrument is precise and has a very little lag. In this type of instruments the time lag and inconsistencies associated with overcoming the friction of the vane are avoided and it allows to measure very small and very large flow rates. Figure 3.2 shows a variometer embedded in the glider. Where A is the accumulator, B is the variometer dial that indicates the climb rate and C is the venturi head. The venturi head is fitted to convert it into a total energy variometer as described below.

Electrically operated variometers have quicker response and better sensitivity in comparison with the mechanical instruments. A switch is used to change the amplification to suit the strength of the lift. This helps to vary the range of an instrument. An audible indication can be given by using a small loudspeaker.

Most pilots prefer to use both mechanical and electrical variometers. A vane type with a speed to fly ring is used in cruising flights between thermals and an electrical instrument with an audio for centring in the lift.

The total energy variometer is a variometer that corrects any lift or sink caused by changes of airspeed to give absolute values [Pig95]. (An instrument can be converted to a total energy by fitting a Brunswick tube or venturi, see Figure 3.2). For example, if the glider is accelerating

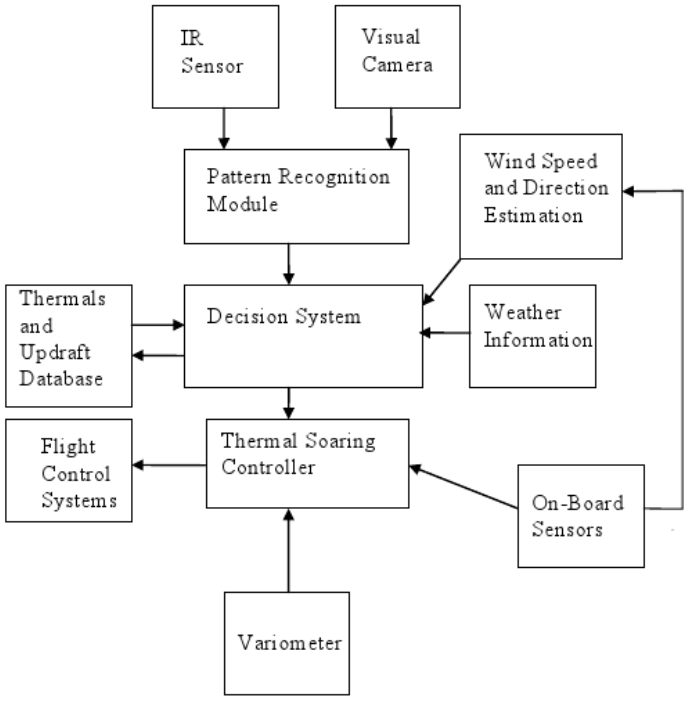

Figure 3.1: Thermal soaring architecture

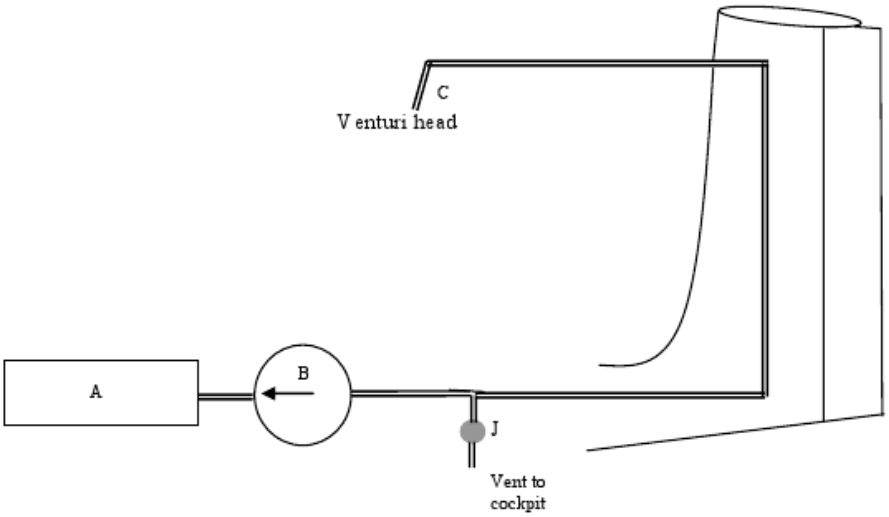

Figure 3.2: Variometer embedded in glider [Pig95]

at any particular moment, the nose will be lower than the normal position for steady state at that airspeed and a higher rate of descent would be sensed. In a total energy variometer, the increase in airspeed also increases the suction at the venturi and this compensates for the descent rate.

When a glider is hit by a horizontal gust disturbance, the total energy variometer indicates a

higher rate of climb. This problem is avoided by fitting a restriction or gust filter between the venturi tube, C and the flow meter, B. A time lag of several seconds also helps to eliminates those effects.

In the 6DoF model, described later, the total energy is monitored and obtained from the following equation:

$$E_T = \frac{1}{2}mV^2 + mgh. \tag{3.1}$$

Where h is altitude value obtained from the navigation module, see Appendix F and V, the total velocity relative to a fixed earth datum is defined as

$$V = \sqrt{u_{cg}^2 + v_{cg}^2 + w_{cg}^2}. \tag{3.2}$$

where u_{cg},v_{cg} and w_{cg} are the body velocity components at the sailplane's centre of gravity.

3.3 On-board Vision based Sensors

A visual sensor along with IR sensors will be used on-board the UAV to search for landmarks associated with thermals, clouds and also soaring birds or gliders for clues. In this section examples are given that describe how visual sensors have been used on-board by various researchers for target detection and sense and avoid applications. The object recognition techniques developed at image processing group at Cranfield University use information from both visual and IR cameras for image recognition.

Dennis [DABL08] explored a vision based solution for sense and avoid system for small UAVs. The solution consisted using a small light weight, low power and commercially available camera, special purpose computational platform based on Helios and a custom FPGA based circuit board developed in Brigham Young University's Robotic Vision Laboratory. This system provides a significant computational power and has been successfully used on small ground vehicles, fixed wing aircraft and quad rotors.

A vision based real-time target localization for single antenna GPS guided UAV is used by Sohn [SLKK08]. A real-time method to calculate the three dimensional location of a fixed target using a gimballed camera on a UAV. The analog output from the camera is passed to the ground station. The image processing software was developed using the OpenCV, which is an open source library for computer vision.

3.4 IR Sensor - Initial Test Results

An IR camera is used in the architecture because it can provided data that can be used to identify the hot spots associated with thermals. As described earlier it is a key sensor in the integrated thermal soaring controller. In this section results of a brief field trial are presented to indicate the feasibility of observing hot spots from some distance away.

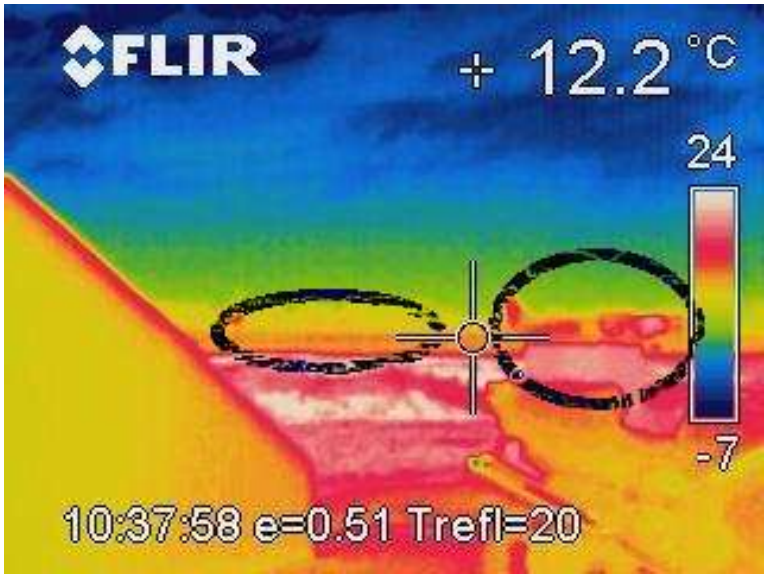

Figure 3.3: IR view of airport

Figure 3.4: View of airport

Figure 3.3 shows an infra red picture taken of Cranfield airport; an aeroplane is clearly visible and is marked by an ellipse. The runway is also distinguishable from the surroundings and the heat coming out of houses approximately one mile away are also noticeable and they are marked in the figure. Figure 3.4 shows the visual image taken of the airport and the houses in the background The houses are identifiable and this image along with the IR image would be used for pattern recognition.

Figures 3.5 and 3.6 show pictures taken of clouds at different times. The temperature bar on the right side of Figure 3.5 shows temperature variations from -19 to 13°C. The black (blue) area, which is the coldest, represents the sky. The patch of clouds are represented by yellow colour. The area of the clouds represented by white and red colour is the hottest and

appears on the bottom of the picture. The sky appearing at the edge is represented by black colour in the top of the figure. The heat signature on all the two pictures makes the clouds visible. This information in combination with visual camera would be used to identify the clouds.

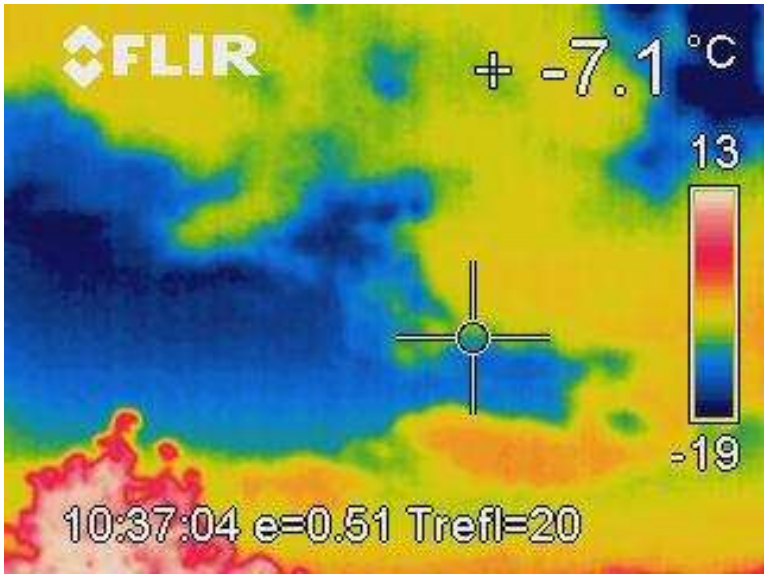

Figure 3.5: First IR view of clouds

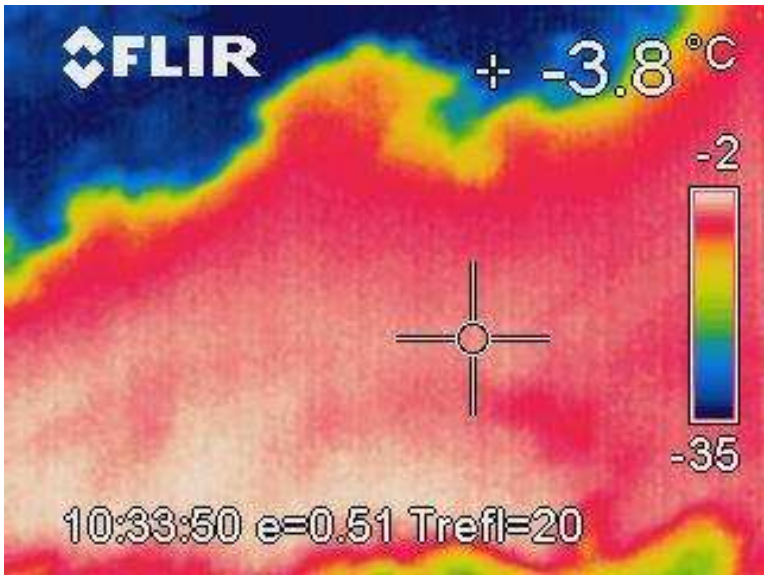

Figure 3.6: Second IR view of clouds

In Figure 3.7 an image of a flying aeroplane is shown, the aircraft is circled. The heat signature of the aircraft appears near the plus mark on the figure. The signature on the left side is that of a cloud. A visible camera will make further classification possible. The clouds once identified with triangular shapes could be used as clues for the presence of thermals as described earlier.

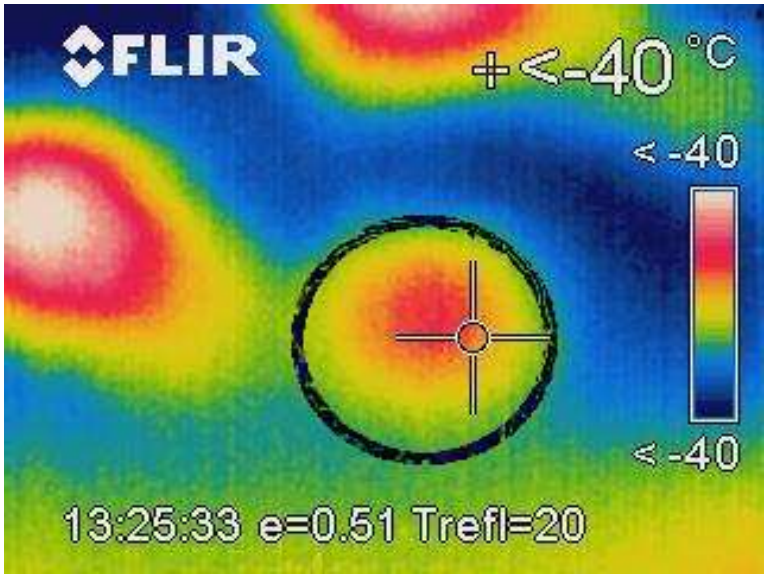

Figure 3.7: IR view of flying aeroplane

Images of distant objects will be required to identify remote thermal activity. Figure 3.8, shows an image taken of the suburbs of Milton Keynes at a distance of approximately ten miles. The image of a building in the suburbs is circled. In Figure 3.8, a hot spot represented by a red patch is a cultivated field. The greenery and heat radiated by a few buildings further away is represented by green and yellow colours. The horizon is represented by light blue colour, which makes hotter buildings and greenery identifiable. Figure 3.9 shows the visual image of the same area. The building that is earlier pointed out is clearly visible.

The ability of the system to observe any thermal activity many miles away by observing ground hot spots would benefit the thermal search.

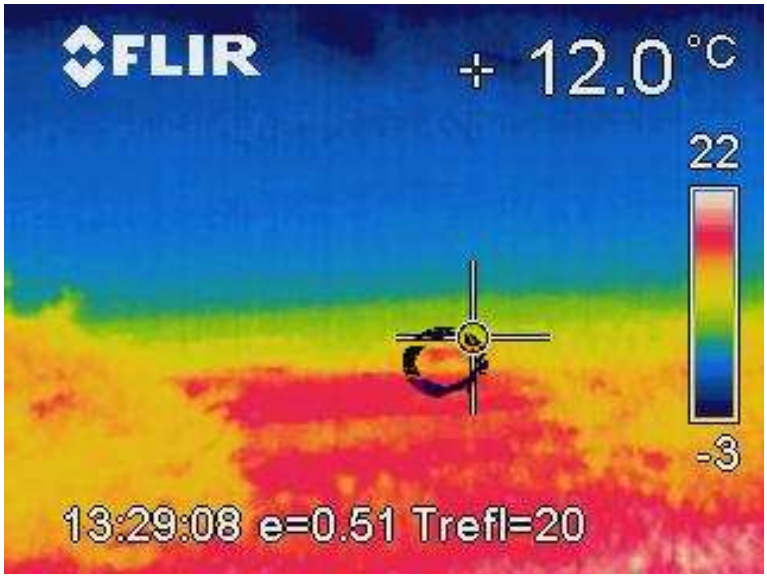

Figure 3.8: IR view of Milton Keynes

Figure 3.9: View of Milton Keynes

Chapter 4

Thermal Soaring

4.1 Introduction

In this chapter the work done on thermal soaring is briefly discussed, it comprises: a brief description of formation of thermals, autonomous motion within thermals, their structure and strength, controller architecture, air vehicle and modelling of the interaction of air vehicle with thermals.

The techniques for a sailplane positioning in a thermal, modelling of its interaction with the thermal and controller design that are used in the thesis include the following.

- Reichmann's technique [CRW+08] for thermal soaring involves using between 25° and 30° bank angle for turning when the climb rate improves. Should the climb rate deteriorate the bank angle is increased to 50° but if remains constant the bank angle is kept between 25° and 30°. Piggott's technique [Pig90] differs somewhat in this, during a gentle turn, if a surge of lift is experienced, tightening the turn will move the aircraft toward the place where the strong lift was experienced. These thermal entering techniques were tested by Cowling [CRW+08] using five different thermal models. For the point mass model, where perfect knowledge was available, Piggott's technique performed better whereas in the full simulation, Reichmann's technique performed better according to the analysis done by Cowling [CRW+08].

- Amrane [Amr05] implemented the effect of thermals on a sailplane within a 6-DoF model, using two dimensional strip theory. A key part of this work was a representative mathematical model of atmospheric thermal lift, and the aerodynamic interaction between the air vehicle wing and the column of rising air. Cook [CCW06] described a control system architecture, which was used as the basis for the design of the soaring controller.

- In this Chapter the suitable bank angle and airspeed for thermal soaring are obtained using Horstmann model [Hor76] and used to program the controller. Carmichael's wide and narrow thermal models [Tho99], populated with Woodward's [Woo58] velocity distribution were used to test a positioning algorithm, using Amrane's 6DoF sailplane

model and a soaring controller based on Cook's [CCW06] controller architecture. The positioning algorithm, which builds on the work of Piggott [Pig90] are used to position the sailplane in a thermal. A logic is also introduced that used information from the aileron control signals to determine the location of the thermal center relative to the aircraft. As a sailplane enters a thermal a roll is experienced on the wings and the sailplane is turned out of the thermal. However an autopilot keeps the sailplane level by generating a control signal to ailerons. The signal generated is used to determine the orientation of the thermal centre with respect to the sailplane.

4.2 Atmospheric Thermals

4.2.1 Sources of Buoyant Convections

According to Cone [Con61], the convection that develops as a result of surface heating, can either have a continuous column air or a discrete air mass. A continuous heating of a fixed point on the surface when a large supply of warm air is available results in the continuous column. However it is rare to have a continuous column as calm air conditions are required. The column of heated air from the source constantly breaks up into discrete masses which the wind carries away. His observation shows that atmospheric thermals form vortex ring from initial clouds, only in a few seconds and within a few hundred feet of altitude.

4.2.2 Structure and Motion of Free Thermals

Warm air, resulting from the sun's heating, rises and acquires the structure of a vortex ring [Wal77] with the upward velocity in the center usually greater than the rate of ascent of the whole thermal. According to Cone [Con64] a free thermal closely approximates to a buoyant vortex ring system in which the ring to core radius ratio (R/a) is less than 10. As the ring rises, it is accompanied by an enclosing body, or shell, of cooler air which it has gathered from its surroundings. Figure 4.1 illustrates the internal structure of such a thermal.

Cooler air continuously circulates in closed stream lines around the vortex core resulting in a continuous upward current in the central region of the shell. The speed with which the thermal rises relative to the atmosphere is given by [Con64]:

$$V' = \frac{r}{4\Gamma R}\left(\ln\frac{8R}{a} - \frac{1}{4}\right); \tag{4.1}$$

Note that the entire velocity field can be specified if the circulation, Γ, the ring radius, R, and core radius, a, are given. A plot of the vertical component of velocity, v_{th} within a shell, a thermal diagram, can be concluded. The diagram is one dimensional and applies to any size of thermal, see Figure 4.2.

A dimensional thermal diagram could be obtained by multiplying the vertical and horizontal scales of Figure 4.2 by the values V' and R respectively. Note that the absolute vertical velocity of the air at any point in the thermal, in still air, relative to the earth is given by

$$w_{th}^{e} = -V' \left(\frac{v_{th}}{V'} + 1 \right); \tag{4.2}$$

Although radial velocity components exist, the vertical motion of the air within the shell is of primary interest as these currents govern the availability of thermal energy for soaring. It is important to remember that the up-gust strength becomes large only near the boundary of the thermal shell and directly above the vortex core.

4.2.3 Flight within a Thermal Shell

If a sailplane enters the top half of a thermal shell and is at some distance (r) from the thermal center, then it will rise or sink relative to the core until v_{th} is equal to the aerodynamic sinking velocity ($V_{s\phi}$) at that radius. At that moment an equilibrium has been reached and the shell will carry the sailplane upwards. Equilibrium can only be reached if the thermal is large enough to satisfy both the aerodynamic and energy requirements of the sailplane. If a thermal is too weak ($V_{s\phi} > v_{th}$) then the sailplane will sink within it but while doing so the aircraft may gain altitude ($V' + v_{th} > V_{s\phi}$).

An important factor in a sailplane's ability to reach equilibrium is if its execution of turns is of small radius. If a certain sailplane can fly at a radius of $r/R = 1.0$, inside a thermal with a minimum sinking velocity of $V_{s\phi}/V' = 0.1$, then from Figure 4.2 equilibrium cannot be reached because v_{th} value is very small. If it circles with a radius of $r/R = 0.3$ then the resulting values of v_{th} are high enough to provide equilibrium even if the sinking velocity could increase 14 times of its original value. In the lower half of the thermal shell the equilibrium flight would still be possible but the motion would be unstable since v_{th} increases continuously toward the core (η)=0 with v/V' (variation with vertical distance (η/R)), (η)-planes are defined as parallel to the core plane, see Figure 4.3. Thus a slight deviation from the equilibrium position would send the craft climbing to the upper half or out of the thermal, see Figure 4.3.

In this thesis, a simplified model of the vortex ring is used for testing the positioning algorithm. Only the inner core is considered and the down draft that occurs in outer layer is ignored. The distribution of vertical velocity is obtained from Woodward's [Woo58] absolute vertical velocity profile. An infinite column structure was assumed to avoid the need to model the upward motion of the shell with time.

4.3 Thermal Model

As mentioned above, the thermal velocity variations used in the study are based on Woodward's absolute vertical velocity distribution, Table 4.3. Thermal sizes are based on Carmichael's strong narrow and wide models, see Table 6.4. A simplistic model of a thermal with regard to growth of the thermal with time is used. The simulations have restricted modelling the head of the thermal but as a constant core, which is invariant with altitude. A mathematical model of an updraft acceleration is described in Appendix C.

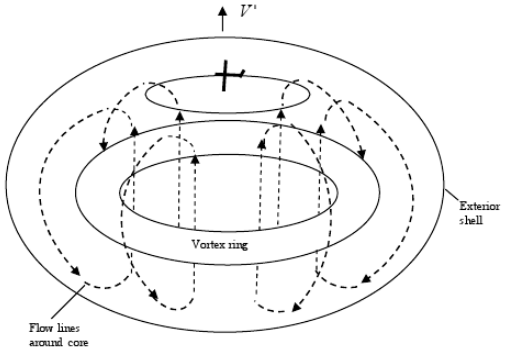

Figure 4.1: Internal structure of thermal [Con64]

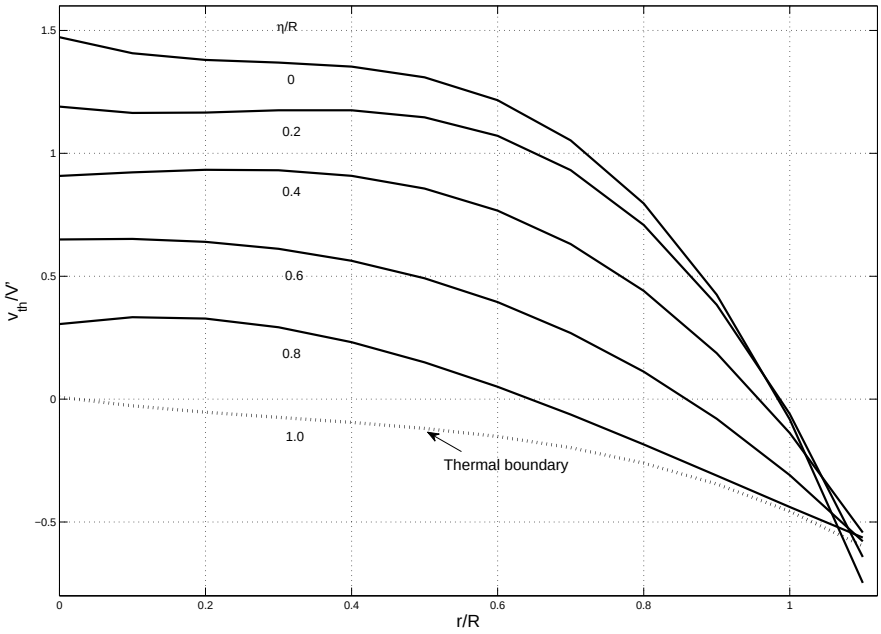

Figure 4.2: Thermal diagram for vertical field [Con64]

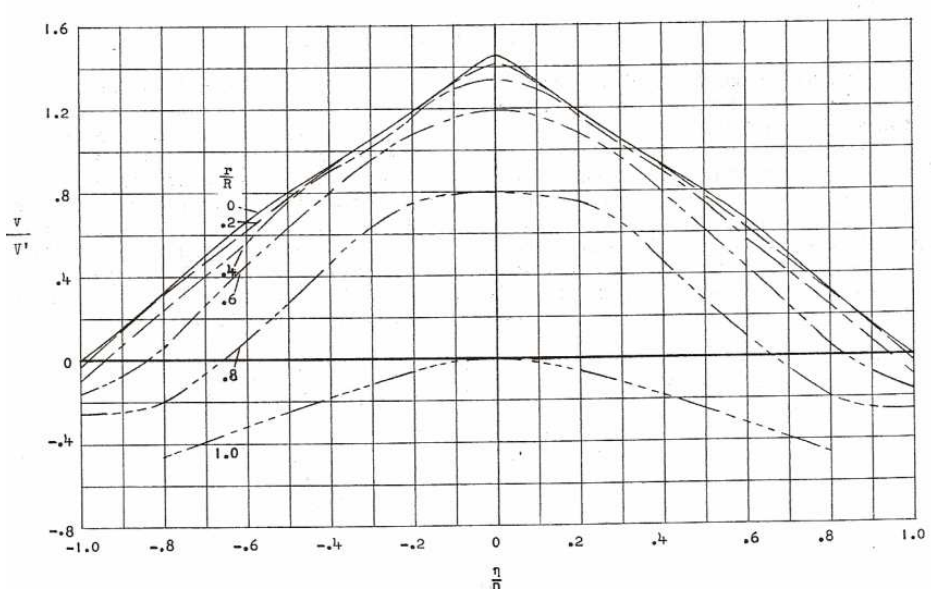

Figure 4.3: Equilibrium stability diagram [Con64]

$R_N(m)$	$R_W(m)$	w (m/s)
0	0	2.45
25	15	2.20
50	30	1.80
75	45	1.40
100	60	1.00
125	75	0.60
145	90	0.00

Table 4.1: Woodward Thermal Model

4.4 Determination of Local Air Angles

4.4.1 Contribution from Thermal Up-gust

Teh mathematical implementation of thermal impact on the sailplane is summarised in Figure 4.4. The magnitude of the updraft velocity (v_{th}) induced by a thermal at any location on the wing, tail or fin is found by determining its distance from the thermal center (d_P), see Figure 4.5. Consider a point, P, on the aircraft located some distance (x_P, y_P, z_P) from the center of gravity and assume that the cg is positioned at $(P_{N_{cg}}, P_{E_{cg}}, h_{cg})$. As the aircraft orientation is known via the Euler angles (ψ, θ, ϕ) the following transformation matrix can be constructed:

$$D^{be} = \begin{bmatrix} c_\theta c_\psi & c_\theta s_\psi & -s_\theta \\ s_\phi s_\theta c_\psi - c_\phi s_\psi & s_\phi s_\theta s_\psi + c_\phi c_\psi & s_\phi c_\theta \\ c_\phi s_\theta c_\psi + s_\phi s_\psi & c_\phi s_\theta s_\psi - s_\phi c_\psi & c_\phi c_\theta \end{bmatrix} \tag{4.3}$$

$R_W(m)$	w (m/s)	$R_N(m)$	w (m/s)
0.00	4.63	0.00	6.20
25.00	4.42	15.00	6.10
50.00	3.39	30.00	5.50
75.00	3.33	45.00	4.25
100.00	2.26	60.00	2.80
125.00	0.95	75.00	1.00
145.00	0.00	90.00	0.00

Table 4.2: Carmichael Thermal Models

and used to find the co-ordinates of the point in earth axes

$$\begin{bmatrix} P_{N_P} \\ P_{E_P} \\ h_P \end{bmatrix} = \left[D^{be}\right]^T \begin{bmatrix} x_P \\ y_P \\ z_P \end{bmatrix} + \begin{bmatrix} P_{N_{cg}} \\ P_{E_{cg}} \\ h_{cg} \end{bmatrix} \tag{4.4}$$

The distance between the center of the thermal and this point is then found by taking only the NED plan coordinates such that [1]:

$$d_P = \sqrt{(P_{N_P} - P_{N_{th}})^2 + (P_{E_P} - P_{E_{th}})^2} \tag{4.5}$$

If $d_P < R_{th}$ then the thermal updraft is assumed to influence that part of the aircraft and the local updraft v_{th_P} is obtained by interpolation from the model data given in Table 6.4 as appropriate. Body air velocities induced by the updraft are then given by:

$$\begin{bmatrix} u^b_{th_P} \\ v^b_{th_P} \\ w^b_{th_P} \end{bmatrix} = D^{be} \begin{bmatrix} 0 \\ 0 \\ v_{th_P} \end{bmatrix} \tag{4.6}$$

Figure 4.4 summarizes this process.

4.4.2 Implementation of the Influence of Perturbed States

As the aerodynamic surfaces have been modelled using strip theory it is necessary to estimate all contributions to the local air velocities. These include changes in angle of attack, α, and side-slip, β, caused by the rotational motion of the aircraft as well as those produced by dihedral and the thermal effects mentioned above [Amr05]. Assuming that the body velocities at the cg are given by u^b_{cg}, v^b_{cg} and w^b_{cg}, than at the arbitrary point P the total body velocities will be:

$$u^b_P = u^b_{cg} + u^b_{th_P} + qz - ry \tag{4.7}$$

$$v^b_P = v^b_{cg} + v^b_{th_P} + rx - pz \tag{4.8}$$

$$w^b_P = w^b_{cg} + w^b_{th_P} + py - qx + w^b_\Lambda \tag{4.9}$$

[1] As the velocity profile of thermal is invariant with height the altitude of the aircraft is not considered.

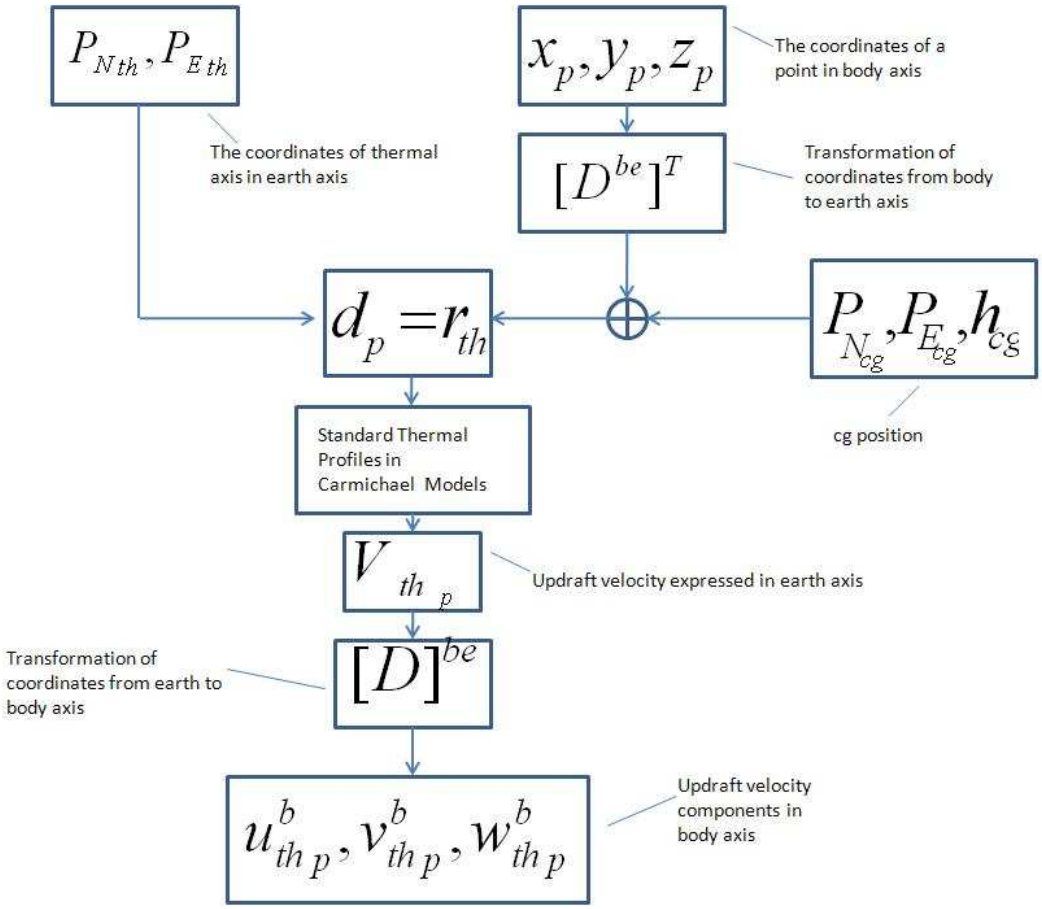

Figure 4.4: Mathematical implementation of thermal [Amr05]

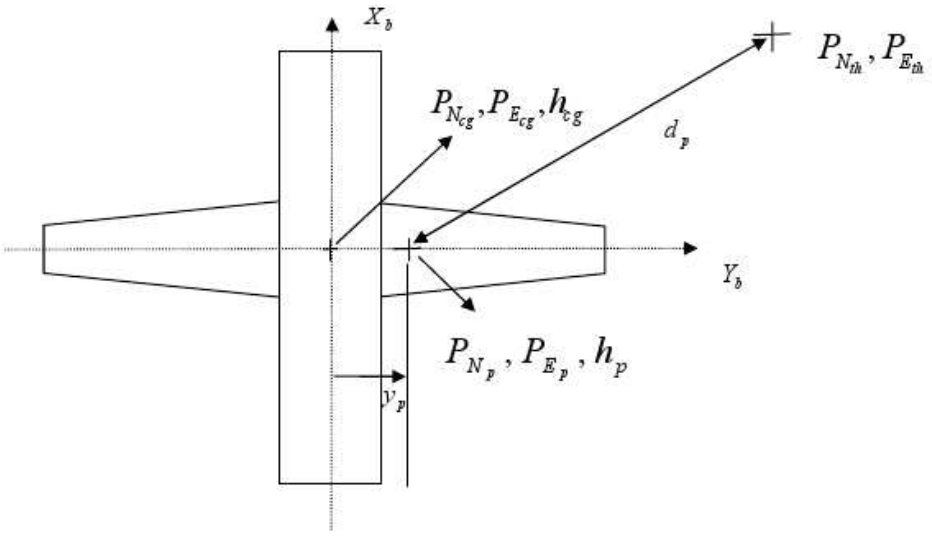

Figure 4.5: Thermal implementation [Amr05]

The local change in vertical velocity caused by dihedral is opposite for each wing but constant across the span, thus:

$$w_\Lambda^b = \Lambda \frac{y}{|y|} v_{cg}^b \tag{4.10}$$

4.4.3 Local Air Data

If the air mass is assumed to be stationary outside any thermal activity then local body velocities given by equations (4.7) - (4.9) represent the air velocities at that location, so:

$$V_P = \sqrt{[u_P^b]^2 + [v_P^b]^2 + [w_P^b]^2} \tag{4.11}$$

and:

$$\tan \alpha_P = \frac{w_P^b}{u_P^b} \qquad \sin \beta_P = \frac{v_P^b}{V_P} \tag{4.12}$$

4.5 Soaring Controller

As the sailplane must orbit within the column of rising air if it is to gain energy from a thermal, it was important to select the optimum target airspeed and bank angle for the soaring controller. The relationship between airspeed, sink speed and radius of turn can be obtained by analysing an aircraft in a stabilized spiral glide [Con64]:

$$L \cos \phi = W \cos \gamma \tag{4.13}$$

$$D = W \sin \gamma \tag{4.14}$$

$$L \sin \phi = \frac{m V_{h\phi}^2}{R\phi} \tag{4.15}$$

Provided $C_D^2 \ll C_L^2 \cos^2 \phi$ then:

$$V_\phi = \sqrt{\frac{2W}{\rho S} \frac{1}{C_L \cos \phi}} \tag{4.16}$$

$$V_{s\phi} = \frac{C_D}{(C_L \cos \phi)^{3/2}} \sqrt{\frac{2W}{\rho S}} \tag{4.17}$$

and:

$$R_\phi = \frac{1}{C_L \sin \phi} \left(\frac{2W}{\rho g S} \right) \tag{4.18}$$

The drag polar for the whole aircraft was obtained by adding zero-lift contributions from the stabilizer, fin and fuselage. A global value for the induced drag was estimated assuming an elliptical lift distribution, thus:

$$\begin{aligned} C_D &= \frac{1}{10^4} \left(28 C_L^3 - 40 C_L^2 + 35 C_L + 132 \right) + \frac{C_L^2}{\pi A}, \\ C_D &= \frac{1}{10^4} \left(28 C_L^3 + 79 C_L^2 + 35 C_L + 132 \right). \end{aligned} \tag{4.19}$$

It is clear from equation (4.17) that, for a given wing loading (W/S) and density altitude, the sink speed is proportional to $C_D/\left(C_L \cos\phi\right)^{3/2}$. Where the mass of the sailplane is 430kg and its wing span is 18m. It can be shown using the drag polar given in Equation 4.19 that the lift coefficient for minimum sink rate is 1.48. Given this value the corresponding bank angle, sink rate and airspeed at any turn radius can be found from equations (4.16) - (4.18). It can be seen, using the Horstmann profiles [Hor76], that the optimum turn radius varies with the type of thermal encountered but always lies between 55m and 85m, see Figure 4.6. As in practice, the size of thermal will be unknown an average turn radius of 60m was chosen which yields a target speed and bank angle of 25m/s and 42° respectively. In Figure 4.7 climb and sink rate in profile A2 of Hortsmann profiles as function of turn radius are plotted. Where Figure 4.8 shows the true air speed and bank angle values required to maintain various radius of turns and the optimum values for airspeed and bank angle lead to 23.2 m/s and 42.5° for the chosen radius of turn. An auto stabilization system consisting of an inner loop was used, see Figure 4.9, to provide sufficient margins of stability and an outer loop for speed and bank control, see Figure 4.10, using classical methods [CCW06]. The positioning algorithm uses a variometer to decide whether a thermal is present and then demands a bank angle to execute turns into the thermal.

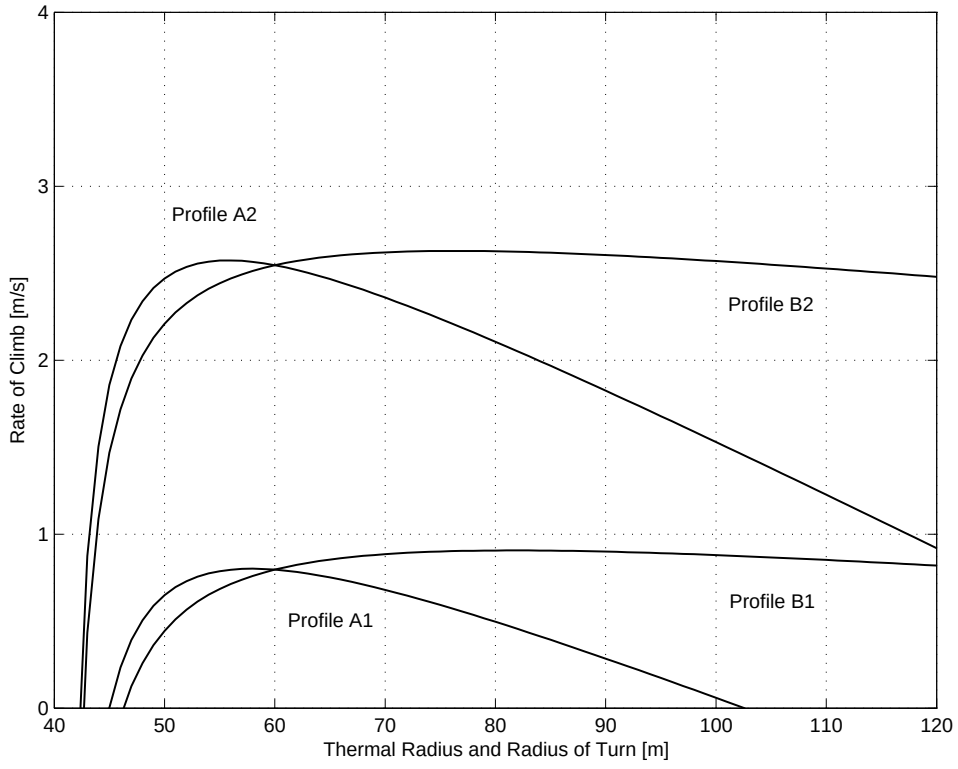

Figure 4.6: Optimum turn radius

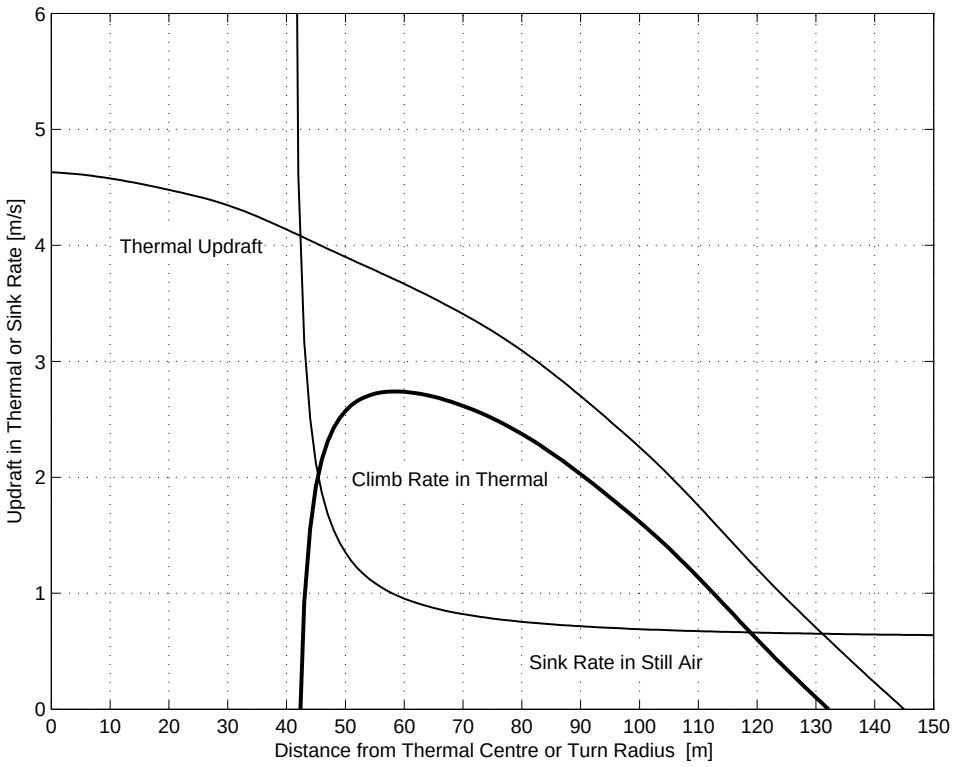

Figure 4.7: Effect of turn radius on climb rate in a thermal

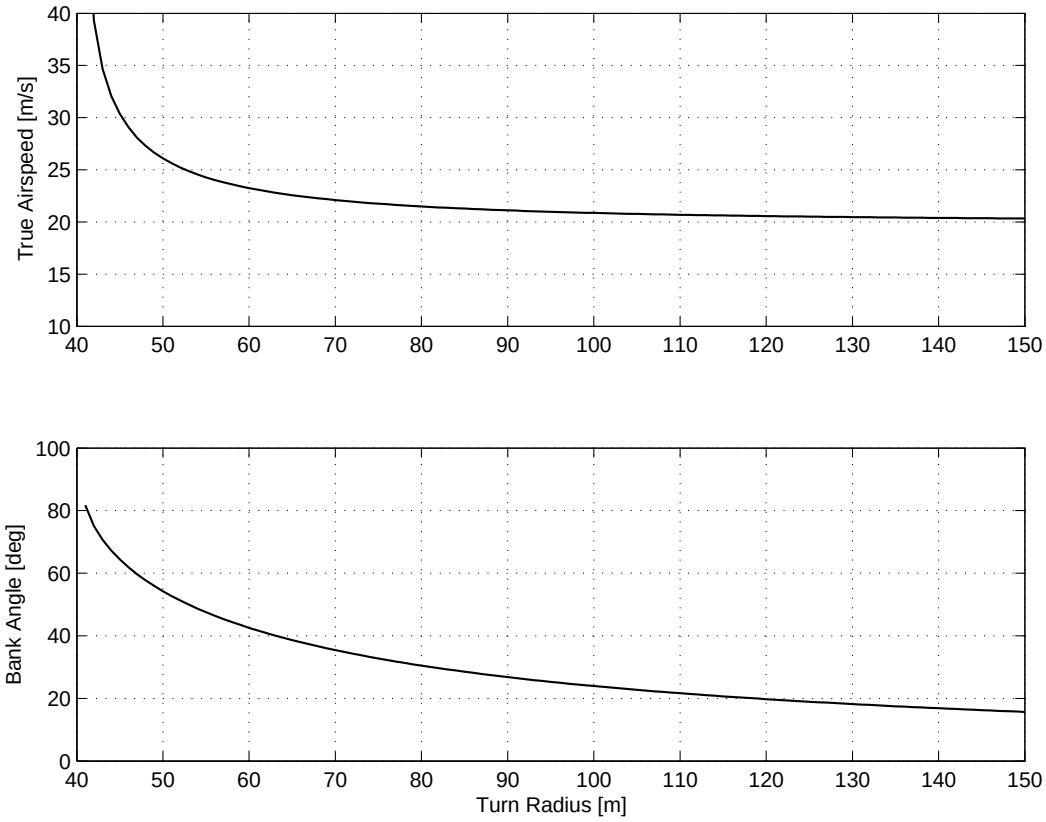

Figure 4.8: Bank angle and airspeed for minimum sink rate

According to reference [CRW+08] Piggott's technique requires pilot's quick reaction where a Reichmann's technique response time was slow and was used by novice pilots. Therefore Piggott's method [Pig90] was used as a basis for developing the following positioning algorithm:

- If a thermal is detected, an angle of 42° is commanded.
- If sink is detected then the sailplane continues to circle but after a heading change of 154° the controller reduces the bank for three seconds to 0° before resuming turns as before. This should move the orbit center closer to the thermal center.

A second order filter was used to smooth out the input bank command, so that large step command of bank input was avoided. Trial and error yields a heading angle of 154°. Piggott's method where a heading angle of 180° which contrast with the bank angle of 30°, was used [CCW06].

4.6 Conclusions

- Optimum values of speed, bank and radius of turn were calculated to maximise the energy extraction from a thermal.
- A heading change of 154° was identified as suitable for reducing the bank when a thermal is lost as it brings back the sailplane for the sizes of the thermals considered.
- The outer loop of the control system was retuned to reduce the oscillations in speed tracking and also to decrease the lag time for bank command tracking.
- The values of speed, turn radius, bank and heading angle chosen also reduced the oscillations experienced due to edge cutting as the sailplane managed to execute tighter turns inside thermals and minimized edge cutting.

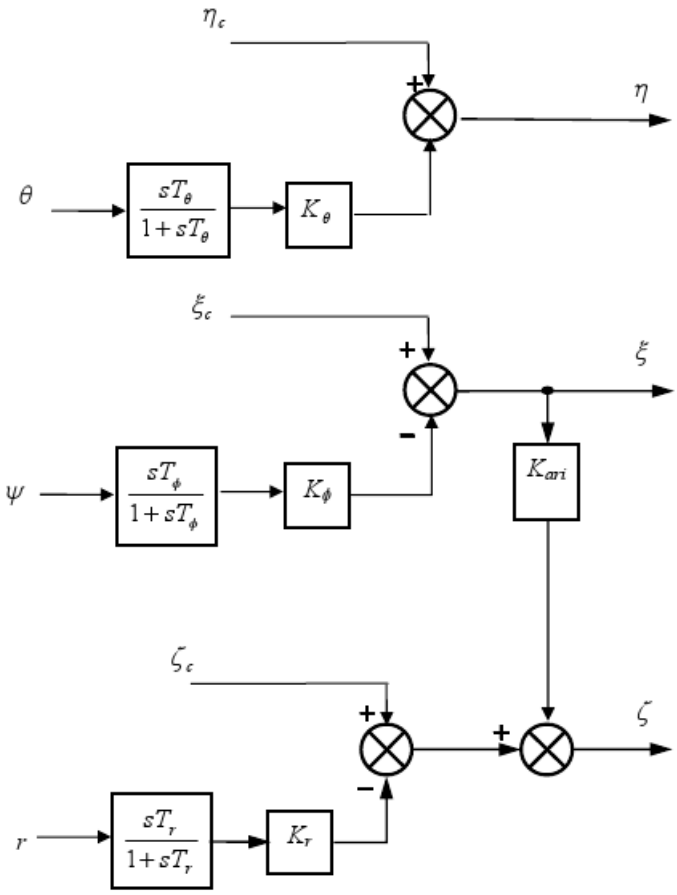

Figure 4.9: Autostabilization system architecture [CCW06]

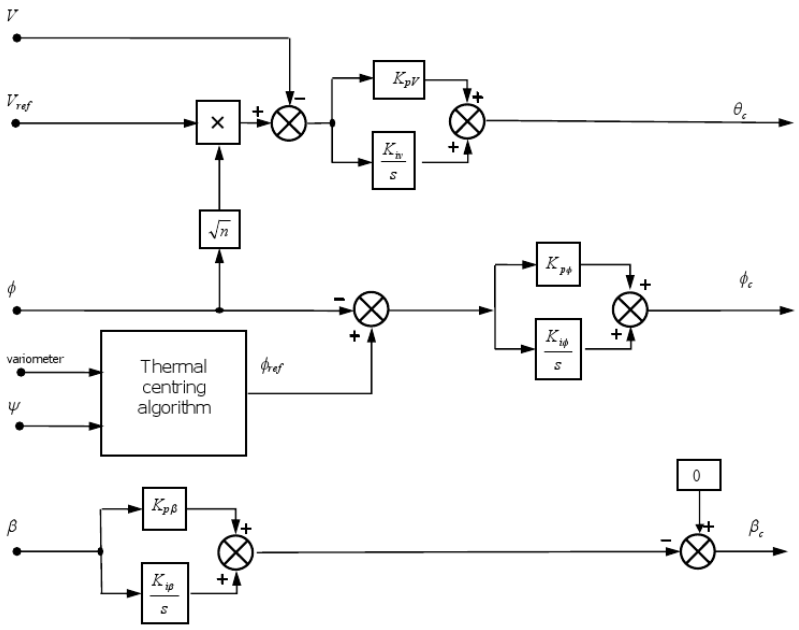

Figure 4.10: Thermal soaring controller architecture

Chapter 5

Dynamic Soaring in Wind Shear

5.1 Introduction

In this chapter, the wind shear model used for dynamic soaring, wind speed and gradient estimation method, point mass model equations, IDVD technique, optimization problem for dynamic soaring and predictions of the fuel saving by the optimization program using a point mass model are described.

In a dynamic soaring cycle a glider UAV climbs into an increasing wind, it can climb to a slightly higher altitude in comparison with a still air climb. The increase in head wind compensates for some of the air speed lost while climbing. In this process the UAV gains potential energy. This energy is then converted into kinetic energy by diving downward with the wind. As the wind speed declines with the altitude, the UAV gains additional kinetic energy. Two effects modify the energy of the UAV, interaction with the ambient wind and losses due to drag.

Sinusoidal cruise trajectories involve a series of boost-glide cycles powered by engines. It starts with an initial boost and followed by an un-powered glide phase. This is followed by a pull-up manoeuvre until the vehicle achieves the initial altitude, speed and flight path angle to repeat the cycle [Mos99].

There is a need for UAVs to increase endurance and/or reduce the amount of fuel carried. The problem is to determine the trajectory required to maximize (in some sense) the extracted energy and make the sailplane follow this trajectory. This can be formulated as an optimal control problem. However, in order to implement such a technique in practice, the solution must be obtained fairly rapidly. Hence we propose the use of a particular direct method, sometime known as the Inverse Dynamics in the Virtual Domain (IDVD) method, which has been shown [Yak00] to be suitable for practical real-time operation.

Non-linear optimal control problems don't have an analytical solution unlike the linear quadratic control problem. Over the past two decades, an approach called the direct method has become popular. The control/state variables are approximated using a polynomial or piecewise constant approximation. The cost functional is approximated as cost function in parallel.

Typical direct methods include a direct shooting quasilinearization and a direct collocation method etc. In this thesis the IDVD technique is used and the MATLAB function `fmincon` is used to solve the resulting non-linear programming problem.

The `fmincon` function finds the minimum of constrained non-linear multivariable function. It attempts to find a constrained minimum of a scalar function of several variable starting at an initial estimate. This method is also called non-linear programming. It starts by using the polynomial coefficients initial guess values and attempts to find a minimizer of the specified function subject to the linear inequalities specified. The minimizer could be a scalar, vector or matrix. The lower and upper bounds are specified for the variable(s) to be minimized, therefore the solution is always between the bounds. It also subjects the minimization to defined non-linear inequalities or equalities.

Zhao [Zha4a, Zha4b] has provided the most promising method for real-time implementation for dynamic soaring optimization. The optimal control problems were converted into parameter optimization with a collocation method and solved numerically using standard non-linear optimization software. Zhao in his paper [Zha04b] extends the work of previous paper [Zha04a] by using a non-linear wind-profile. However no indication of the efficiency of the methods is provided. The approach proposed in this paper draws on Zhao in the modelling and problem formulation.

The IDVD method is used here to solve the optimal control problem. This is a direct method that uses the inverse dynamics of a point-mass model of the aircraft to perform a search in the output space to obtain optimal trajectories that satisfy the constraints on the states and controls. The initial and final conditions enforce the dynamic soaring pattern, whilst the constraints on flight path angle, bank angle, thrust and airspeed are enforced. The initial and final jerks (derivatives of acceleration) are used as the search parameters. A virtual arc is used to decouple the speed profile from the spatial paths. Polynomials are used to define the spatial trajectories and the speed, and their coefficients are determined analytically from the known boundary conditions, initial and final jerks and the soaring cycle time. The resulting non-linear programming problem is solved using the MATLAB `fmincon` function. The method has a drawback as the parametrization uses a finite degree polynomial, the search is conducted over a subset of all possible trajectories resulting in sub-optimal solutions.

The point mass and the wind gradient models are based on those from Zhao [Zha04b]. The equations of motion are normalized, using a wind conditioning parameter that represents the combined effect of atmospheric density, wing loading and wind gradient slope. Two modes of operation are considered — a crosswind mode and loitering mode. In the first mode the aircraft is required to travel a distance in the horizontal direction during each cycle. In the second mode it returns to its initial state at the end of the cycle. A cost function that minimized the total power used per horizontal distance is used for the crosswind mode and the total power used per total time in the air is used for loitering mode.

The resulting optimal trajectories are verified using a six degrees of freedom (6DoF) model of a high-performance powered sailplane [Amr05]. A controller, based on a classical architecture, was designed to track the trajectories generated by the optimization routine. As like Zhao

[Zha04a, Zha04b], the proposed method requires *a priori* knowledge of these characteristics.

5.2 Dynamic Soaring Model

5.2.1 Wind Profile Model

Typically, reasonably stable atmospheric conditions exist close to the sea surface with the wind velocity nearly zero at the surface and increasing gradually with altitude. A wind profile is developed below and is based on the work of Zhao [Zha04b, Zha04a]. In this work only the horizontal wind component is considered and it is assumed static being some function of altitude only.

The average wind gradient slope is defined as

$$G = \frac{W_{x,max}}{h_{tr}}, \tag{5.1}$$

where $W_{x,max}$ is the maximum horizontal wind and h_{tr} is the transition altitude at which the wind becomes constant. The wind component and altitude are normalized as:

$$\bar{W_x} = \frac{W_x}{W_{x,max}}, \tag{5.2}$$

$$\bar{h} = \frac{h}{h_{tr}}, \tag{5.3}$$

A linear wind profile can be expressed as $W_x = Gh$ and in normalized form as $\bar{W_x} = \bar{h}$. Equally a quadratic variation of the linear profile is given as:

$$\bar{W_x} = A\bar{h} + (1 - A)\bar{h}^2, \tag{5.4}$$

where $\bar{W_x}$=0 at $\bar{h}$=0 and $\bar{W_x} = 1$ at $\bar{h} = 1$. Use of equation (5.1) and substitution of equation (5.2) into equation (5.4) results in:

$$W_x = G\left(Ah + \frac{1 - A}{h_{tr}}h^2\right). \tag{5.5}$$

To ensure that the wind component is within $[0, W_{x,max}]$, it is required that $0 < A < 2$. The exponential like wind profile corresponds to $0 < A < 1$ and $1 < A < 2$ gives a logarithmic wind profile. In this project, values of $A = 1.5$ and $G = 0.04107$ (an arbitrary value selected from the range quoted by Zhao [Zha04b, Zha04a]) is used.

5.2.2 Wind Shear Characteristics Estimation

The optimal trajectory generation method assumes that the wind shear characteristics are known. Hence a method that can estimate the wind shear model parameters is required. The wind velocity can be obtained by using the measured values of airspeed in the body axis

and measured ground speed values in earth axis. The wind speed equation from (5.5) can be expressed as:

$$W = GAh + \frac{G(1-A)}{h_{tr}}h^2. \tag{5.6}$$

Standard least squares estimation [KB95] can be used to estimate the values of G and A. For this method, the model is taken as

$$Y = \Theta^T X. \tag{5.7}$$

Where Y is the vector of the measurement sequences, X is a vector of known value sequences and Θ is the vector of unknowns. From equation (5.6), the unknown parameters are taken as $\theta_1 = GA$ and $\theta_2 = G(1-A)$, and the known values are $x_1 = h$ and $x_2 = h^2/h_{tr}$. The estimate of the unknowns, $\widehat{\Theta}$, is obtained by [KB95]

$$\widehat{\Theta} = (X^T X)^{-1} X^T Y. \tag{5.8}$$

To test the method, a time varying wind component was used in the 6DoF simulation, and equation (5.8) was used to estimate G and A.

The value of the average wind direction was calculated by averaging the two horizontal wind velocity components, W_x and W_y, giving the average wind direction as

$$\theta_{wind} = \text{atan2}(W_x, W_y). \tag{5.9}$$

For the 6DoF simulation, the estimated value of $A = 1.38$ was obtained compared to the actual value of $A = 1.5$. An estimated value of $G = 0.1$ and the actual value of $G = 0.096$. The estimated value of average wind direction was 2.2°, whereas the actual value was 1.8°. The value of the wind direction was initially set from the north direction but it was varied linearly with time.

5.2.3 Point Mass Model

UAV motion can be represented by a three-dimensional point fixed mass model in a stationary flat earth reference system [Zha04a]. The equations of motion are (where T is thrust in equation 5.10):

$$m\frac{dV}{dt} = T - D - mg\sin\gamma - m\frac{dW_x}{dt}\cos\gamma\sin\psi, \tag{5.10}$$

$$mV\cos\gamma\frac{d\psi}{dt} = L\sin\phi - m\frac{dW_x}{dt}\cos\psi, \tag{5.11}$$

$$mV\frac{d\gamma}{dt} = L\cos\phi - mg\cos\gamma + m\frac{dW_x}{dt}\sin\gamma\sin\psi, \tag{5.12}$$

$$\frac{dh}{dt} = V\sin\gamma, \tag{5.13}$$

$$\frac{dx}{dt} = V\cos\gamma\sin\psi + W_x(h), \tag{5.14}$$

$$\frac{dy}{dt} = V\cos\gamma\cos\psi. \tag{5.15}$$

Where T is defined as thrust in equation (5.10). The state variables are $[V, \psi, \gamma, x, y, h]$ and the control variables are $[C_L, \Phi, T]$. The lift and drag forces are represented as

$$L = \frac{1}{2}\rho V^2 S C_L, \tag{5.16}$$

$$D = \frac{1}{2}\rho V^2 S C_D, \tag{5.17}$$

and C_D is described by equation (5.18).

A high performance sailplane was used to parametrize the point mass model. The relationship between drag and lift of air foil was expressed using the following polynomials, derived from the drag polar based on reference [Tho99].

$$C_D = \frac{1}{10^4}\left(28C_L^3 - 40C_L^2 + 35C_L + 53\right), \tag{5.18}$$

The total drag coefficient expression that includes the contributions from stabilizer, fin and fuselage [Amr05] is expressed as:

$$C_D = \frac{1}{10^4}\left(28C_L^3 + 79C_L^2 + 35C_L + 132\right). \tag{5.19}$$

Note that the three-dimensional flow effects on C_D are ignored.

Following Zhao, [Zha04a] equations (5.10)–(5.15) are normalized as

$$\bar{V} = \frac{G}{g}V, \qquad \left(\bar{x}, \bar{y}, \bar{h}\right) = \frac{G^2}{g}(x, y, h), \tag{5.20}$$

$$\bar{T} = \frac{T}{mg}, \qquad \sigma = Gt, \tag{5.21}$$

and we have

$$\dot{(\cdot)} = \frac{d(\cdot)}{d\sigma} = \frac{1}{G}\frac{d(\cdot)}{dt}, \tag{5.22}$$

where B is defined as

$$B = \frac{1 - A}{\bar{h}_{tr}}, \tag{5.23}$$

and

$$\bar{h}_{tr} = \frac{h_{tr}}{g/G^2}. \tag{5.24}$$

The normalized equations of motion, after some derivation, become:

$$\dot{\bar{V}} = \bar{T} - \bar{\rho}\bar{V}^2 C_D - \sin\gamma - (A + 2B\bar{h})\bar{V}\sin\gamma\cos\gamma\sin\psi, \tag{5.25}$$

$$\dot{\psi} = \frac{\bar{\rho}\bar{V}C_L\sin\phi}{\cos\gamma} - (A + 2B\bar{h})\tan\gamma\sin\psi, \tag{5.26}$$

$$\dot{\gamma} = \bar{\rho}\bar{V}C_L\cos\phi - \frac{\cos\gamma}{\bar{V}} + (A + 2B\bar{h})\sin^2\gamma\sin\psi, \tag{5.27}$$

$$\dot{\bar{h}} = \bar{V}\sin\gamma, \tag{5.28}$$

$$\dot{\bar{x}} = \bar{V}\cos\gamma\sin\psi + (A\bar{(h)} + B\bar{h}^2), \tag{5.29}$$

$$\dot{\bar{y}} = \bar{V}\cos\gamma\cos\psi. \tag{5.30}$$

where $\bar{\rho}$ is the wind shear parameter defined as:

$$\bar{\rho} = \frac{\rho g^2}{2(mg/S)G^2}. \tag{5.31}$$

The total air-relative energy can be defined as:

$$E = mgh + \frac{mV^2}{2}, \tag{5.32}$$

$$e_T = \frac{E}{mg} = h + \frac{V^2}{2g}, \tag{5.33}$$

and is normalized after Zhao[Zha04b, Zha04a] as:

$$\bar{e}_T = e_T\frac{G^2}{g} = \frac{G^2}{g}(h + \frac{V^2}{2g}). \tag{5.34}$$

and using equation (B.1) results in:

$$\bar{e}_T = \bar{h} + \frac{\bar{V^2}}{2}. \tag{5.35}$$

The normalized energy rate is obtained by differentiating equation (5.35),

$$\dot{\bar{e}}_T = \dot{\bar{h}} + \bar{V}\dot{\bar{V}}. \tag{5.36}$$

Substituting values of $\dot{\bar{h}}$ from equation (5.28) and $\dot{\bar{V}}$ from equation (5.25) results in:

$$\dot{\bar{e}}_T = \bar{V}\sin\gamma + \bar{T}\bar{V} - \bar{\rho}\bar{V}^3 C_D - \bar{V}\sin\gamma - (A + 2B\bar{h})\bar{V}^2\sin\gamma\cos\gamma\sin\psi, \tag{5.37}$$

Which gives

$$\dot{\bar{e}}_T = \dot{\bar{E}}_{thrust} - \dot{\bar{E}}_{drag} + \dot{\bar{E}}_{wind}, \tag{5.38}$$

where $\dot{\bar{E}}_{thrust} = \bar{T}\bar{V}$, $\dot{\bar{E}}_{drag} = \bar{\rho}\bar{V}^3 C_D$, $\dot{\bar{E}}_{wind} = -(A + 2B\bar{h})\bar{V}^2\sin\gamma\cos\gamma\sin\psi$.

5.3 IDVD Method

This is a non-linear constrained optimization method where some reference polynomials are determined by the boundary conditions. The speed profile can be separated from trajectory by introduction of a virtual arc instead of time . Inversion of the model dynamics means that the inequality constraints (ϕ, Speed, γ and T)are algebraic functions of the output. For further details of the method, see references [Yak00, WCY08].

5.3.1 Inverse Dynamics

By manipulating the equations of motion, the state and control vectors can be expressed as a functions of the output vector. The outputs of the system are taken as x, y, and h and the inputs are $\bar{T}$, C_L and ϕ. Manipulating equations (5.25)-(5.30) gives the inverse dynamics as

$$\bar{V} = \sqrt{(\dot{\bar{x}} - \bar{W}_x)^2 + \dot{\bar{y}}^2 + \dot{\bar{h}}^2}, \tag{5.39}$$

$$\gamma = \arcsin \frac{\dot{\bar{h}}}{\bar{V}}, \tag{5.40}$$

$$\psi = \text{atan2}(\dot{\bar{y}}, (\dot{\bar{x}} - \bar{W}_x)), \tag{5.41}$$

$$\dot{\gamma} = \frac{\ddot{\bar{h}}}{\sqrt{\bar{V} - \dot{\bar{h}}^2}} - \frac{\dot{\bar{h}}((\dot{\bar{x}} - \bar{W}_x)(\ddot{\bar{x}} - \dot{\bar{W}}_x) + \dot{\bar{y}}\ddot{\bar{y}}) + \dot{\bar{h}}\ddot{\bar{h}}}{\bar{V}^2\sqrt{\bar{V} - \dot{\bar{h}}^2}}, \tag{5.42}$$

$$\dot{\psi} = \frac{(\dot{\bar{x}} - \bar{W}_x)\ddot{\bar{y}} - \dot{\bar{y}}(\ddot{\bar{x}} - \dot{\bar{W}}_x)}{((\dot{\bar{x}} - \bar{W}_x) + \dot{\bar{y}})^2}, \tag{5.43}$$

$$\bar{T} = \dot{\bar{V}} + \rho\bar{V}^2 C_D + \sin\gamma + (A + 2B\bar{h})\bar{V}\sin\gamma\cos\gamma\sin\psi, \tag{5.44}$$

$$\phi = \text{atan2}(\cos\gamma\dot{\psi} - (A + 2B\bar{h})\tan\gamma\sin\psi, \dot{\gamma} + (\cos\gamma)/\bar{V} - (A + 2B\bar{h})\sin^2\gamma\sin\psi), \tag{5.45}$$

$$C_L = \frac{\bar{V}\dot{\gamma} + \cos\gamma + (A + 2B\bar{h})\bar{V}\sin^2\gamma\sin\psi}{\bar{\rho}\bar{V}^2\cos\phi}. \tag{5.46}$$

5.3.2 Parametrization

The trajectories are defined by coefficients of the polynomials. The coefficients are determined analytically from the known boundary conditions, that is the initial and final positions, velocities, accelerations and the free variables, which are taken as the initial and final jerks and the final time. The degree of the reference polynomials is given by the number of boundary conditions that have to be met. The minimum degree must be equal to $n = d_0 + d_f + 1$ with $d_{0,f}$ being the maximum order of the time derivative of the UAV coordinates. If the initial and final acceleration coordinates are pre-set ($d_0 = d_f = 2$), the reference polynomial will be fifth order. An addition of one fictive boundary condition gives a more flexible reference trajectory. These fictive boundary values are added as additional optimization variables. They are free to vary to find more optimal solutions [Yak00, WCY08]. In this case $n = 7$

and this gives us a total of 24 coefficients calculated from

$$a_{x0} = x_0, \tag{5.47}$$
$$a_{x1} = x_0', \tag{5.48}$$
$$a_{x2} = x_0'', \tag{5.49}$$
$$a_{x3} = x_0''', \tag{5.50}$$
$$a_{x4} = -\frac{2x_f''' + 8x_0'''}{\tau_f} + \frac{30x_f'' - 60x_0''}{\tau_{f^2}} - \frac{180x_f' + 240x_0'}{\tau_{f^3}} + 420\frac{x_f - x_0}{\tau_{f^4}}, \tag{5.51}$$
$$a_{x5} = \frac{10x_f''' + 20x_0'''}{\tau_{f^2}} - \frac{140x_f'' - 200x_0''}{\tau_{f^3}} + \frac{780x_f' + 900x_0'}{\tau_{f^4}} - 1680\frac{x_f - x_0}{\tau_{f^5}}, \tag{5.52}$$
$$a_{x6} = -\frac{15x_f''' + 20x_0'''}{\tau_{f^3}} + \frac{195x_f'' - 225x_0''}{\tau_{f^4}} - \frac{1020x_f' + 1080x_0'}{\tau_{f^5}} + 2100\frac{x_f - x_0}{\tau_{f^6}}, \tag{5.53}$$
$$a_{x7} = 7\frac{x_f''' + x_0'''}{\tau_{f^4}} - 84\frac{x_f'' - x_0''}{\tau_{f^5}} + 420\frac{x_f - x_0}{\tau_{f^6}} - 840\frac{x_f - x_0}{\tau_{f^7}}, \tag{5.54}$$

where τ_f is the final value of the individual arc, and is the free parameter of the optimization. The reference function is then

$$x(\tau) = \sum_{k=0}^{7} \frac{a_{xk}\tau^k}{\max(1, k(k-1))}. \tag{5.55}$$

The process is identical for the two other coordinates, y and h.

5.3.3 The Virtual Arc

The use of a virtual arc, τ, enables the speed profile to be separated from the trajectory. A UAV can therefore follow the same trajectory with different speed histories. If we set $\tau = t$ then the speed is tightly coupled to the path and is equal to:

$$V = \sqrt{\dot{x}^2 + \dot{y}^2 + \dot{h}^2}. \tag{5.56}$$

The virtual arc is linked to the time by the variable speed parameter, λ, which allows us to independently vary speed along the trajectory path. The speed is then

$$V = \lambda\sqrt{x'^2 + y'^2 + h'^2}. \tag{5.57}$$

A numerical solution is obtained by dividing the virtual arc $[0,\ \tau_f]$ into N equally placed points [CYW07]. The interval between two points is defined as:

$$\Delta\tau = \frac{\tau_f}{N-1}. \tag{5.58}$$

With $\tau_0 = 0$ the next value of the virtual arc is computed as:

$$\tau_j = \tau_{j-1} + \Delta\tau \text{ for } j = 1 \ldots N. \tag{5.59}$$

The reference polynomials are found as polynomials of τ and these only depend on the boundary conditions.

The initial conditions are converted from time derivatives to virtual arc derivatives using the following relationship:

$$\lambda(\tau) = \frac{d\tau}{dt} \tag{5.60}$$

This brings us to the relations:

$$\dot{x} = \frac{dx}{d\tau}\frac{d\tau}{dt} = \lambda x', \tag{5.61}$$

$$\ddot{x} = \frac{d((\lambda x')}{d\tau}\frac{d\tau}{dt} = \lambda^2 x'' + \lambda\lambda' x', \tag{5.62}$$

$$\dddot{x} = \frac{d(\lambda^2 x'' + \lambda\lambda' x')}{d\tau}\frac{d\tau}{dt} = \lambda^3 x''' + 3\lambda^2\lambda' x'' + x'(\lambda^2\lambda'' + \lambda\lambda'^2). \tag{5.63}$$

Rearrangement of equations (5.61) and (5.62) leads to the expression of the virtual arc's first and second derivatives of the coordinates:

$$x' = \dot{x}\lambda^{-1}, \tag{5.64}$$

$$x'' = \ddot{x}\lambda^{-2} - \dot{x}\lambda'\lambda^{-2}. \tag{5.65}$$

For the boundary, the values of $\lambda_{0,f} = V_{0,f}$ and $\lambda'_{0,f} = \dot{V}_{0,f}V_{0,f}^{-1}$ may be chosen but the scaling of λ does not really matter (allowing the virtual speed and the actual speed to be equal at the boundaries just implies that the virtual arc τ_f will be of the order of the path length). The current time is computed as follows:

$$t_j = t_{j-1} + \Delta t_{j-1}, \tag{5.66}$$

where

$$\Delta t_{j-1} = 2\frac{\sqrt{(x_j - x_{j-1})^2 + (y_j - y_{j-1})^2 + (h_j - h_{j-1})^2}}{V_j - V_{j-1}}. \tag{5.67}$$

Therefore the current value of the speed factor is:

$$\lambda_j = \frac{\Delta\tau}{\Delta t_{j-1}}. \tag{5.68}$$

5.3.4 The Optimization Problem

The differential flatness properties allow us to set the optimization problem as a non-linear programming problem in the output space [CYW07]:

$$\min\left\{\Phi : \mathbf{y}(t) \in R^4, t \in [0, t_f]\right\}, \tag{5.69}$$

such that:

$$d_1(\mathbf{y}) \leq 0, \tag{5.70}$$

$$\mathbf{x}_0 - d_2(\mathbf{y}(0)) = 0, \tag{5.71}$$

$$\mathbf{x}_f - d_2(\mathbf{y}_{t_f}) = 0, \tag{5.72}$$

where Φ is the cost function, $\mathbf{y}$ is the output vector (x, y, h, V), d_1 represents the inequality constraints and is an algebraic function of the output (and its derivatives). d_2 is the algebraic function relating y to the vehicle state and control vector $\mathbf{x}$ and where x_0 represent the initial x at $t = t_0$ and terminal x_f at $t = t_f$ respectively. Where $\mathbf{y}_f$ represents the terminal output at $t = t_f$. The problem has been programmed in MATLAB using the parametrization described and solved using the MATLAB `fmincon` function. The cost function $\Phi_{travelling}$ minimizes the power used per horizontal distance travelled in cross wind. The fuel flow in a propeller engine is approximately proportional to the power i.e. to TV. Therefore the total fuel usage per distance travelled in (for example the x direction) is proportional to

$$\frac{\int T\sqrt{\dot{x}^2 + \dot{y}^2 + \dot{z}^2}dt}{\int \dot{x}dt}. \tag{5.73}$$

Hence the cost function for cross wind travelling mode is:

$$\Phi_{travelling} = \frac{\int_0^{t_f} T\sqrt{\dot{x}^2 + \dot{y}^2 + \dot{z}^2}dt}{\int \dot{x}dt}. \tag{5.74}$$

In case of loitering mode, the total power used over the total time in air is minimized. The loitering cost function $\Phi_{loitering}$is described as:

$$\Phi_{loitering} = \frac{\int_0^{t_f} TVdt}{t_f}. \tag{5.75}$$

5.3.5 Constraints

Some constraints are specified to avoid singularities in the dynamic inversion equations. Other constraints are imposed to represent limits on the control power and the maximum airspeed.

The possible singularities are:

$$\cos(\gamma) = 0, \tag{5.76}$$

$$\cos(\phi) = 0, \tag{5.77}$$

$$g\cos(\gamma) + V\dot{\gamma} = 0. \tag{5.78}$$

Thus remaining constraints are:

$$-60^\circ < \phi < 60^\circ, \tag{5.79}$$

$$20 \text{ m/s } < V < 30 \text{ m/s }, \tag{5.80}$$

$$-15^\circ < \gamma < 15^\circ, \tag{5.81}$$

$$0 \text{ N } < T < 1264 \text{ N }. \tag{5.82}$$

5.4 Predictions

In this section, the optimization results are presented for two problems: travelling normal to the wind direction (cross wind) and loitering, (where the vehicle returns to its starting point) problems. The wind is assumed to be blowing toward *east* and only has a horizontal component. In case of cross wind the sailplane travels in *north* direction at the end of the cycle and thrust used is minimized. In loitering mode, the sailplane is required to return to its initial state at the end of the cycle and average thrust used is minimized. For these problems, the wind is assumed to be from an easterly direction, with non-linear wind shear parameters of $A = 1.5$ and $G = 0.04107$/s. The results of the 6DoF simulation are also presented in Chapter 6. In addition, a method to estimate the wind shear parameters is proposed and tested with the 6DoF simulation.

5.4.1 The Crosswind Problem

Figure 5.1 shows a three dimensional view of the optimal trajectory for the crosswind mode problem and the UAV is required to travel north. The powered sailplane initially turns into the wind and climbs to gain potential energy from kinetic energy. The trade-off between speed and altitude is shown in Figure 5.2. As the speed drops to near the minimum of 20 m/s, it begins to turn away from the wind and increases speed with some additional thrust. It reaches a maximum altitude of just over 20 m after about 27 s when it is travelling in an northerly direction. It continues to turn away from the wind and dives, gaining kinetic energy from the loss in potential energy and wind. The airspeed reaches a minimum at the peak altitude and a maximum at the lowest altitude, see Figure 5.2 and the lowest airspeed corresponds to the peak lift coefficient Figure 5.4). The peak normalized thrust occurs near the end of the dynamic soaring cycle when the vehicle turns back into the wind (see Figure 5.4).

The normalized energies are shown in Figures 5.5. The kinetic energy is traded for the potential energy as the powered sailplane gains altitude. After reaching maximum altitude, the potential energy is traded for the kinetic energy. The total energy and contributions from thrust, wind and drag are also shown. The contribution from thrust is highest towards the end of the cycle. The drag value is proportional to the lift-coefficient value. Normalized energy rates are shown in Figure 5.6. Where the sum of the total energy over the cycle is zero. The contribution of the wind energy rate, thrust and drag rates are also presented. The wind energy is positive as initially a positive glide angle is used to gain altitude in the wind

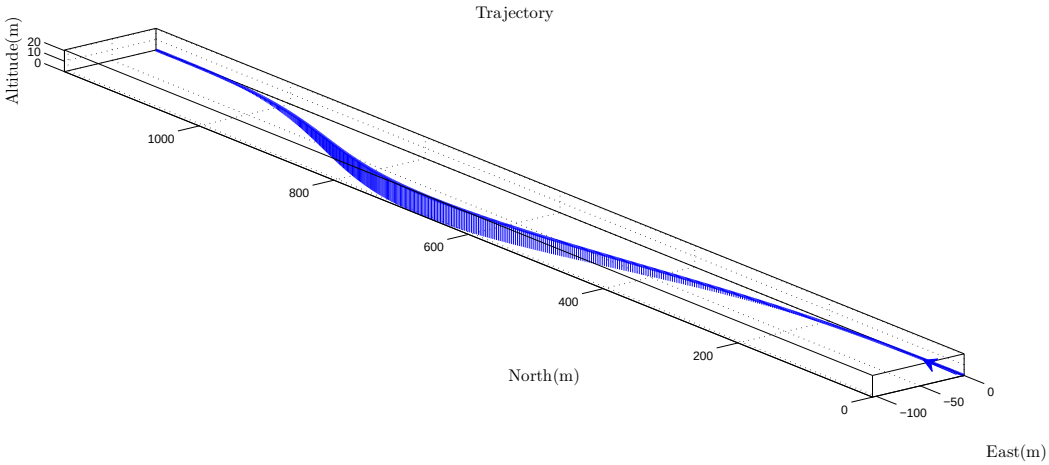

Figure 5.1: Optimal trajectory for crosswind travelling

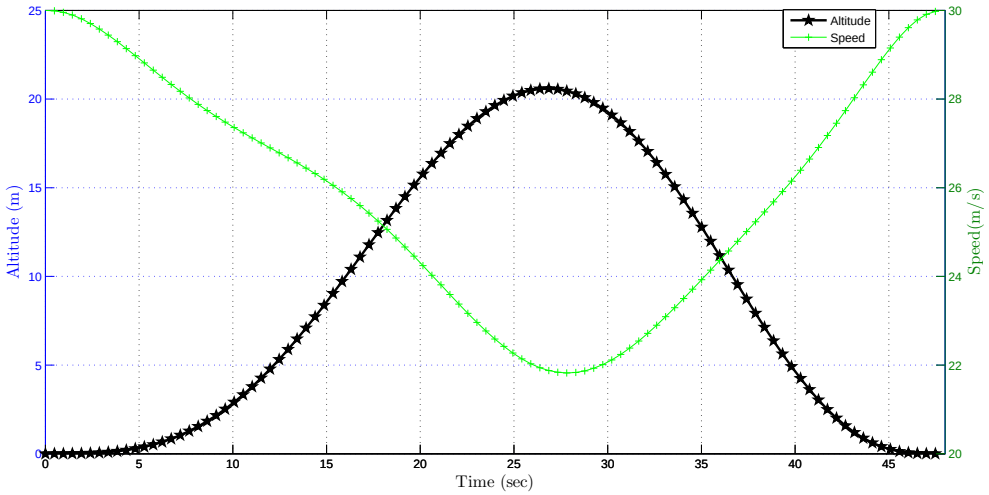

Figure 5.2: Altitude and speed for crosswind travelling

with a negative heading angle. This makes the contribution of the wind energy positive as the resulting negative sign cancels the negative sign in the wind energy rate equation (5.36). The sailplane loses height with a positive heading angle and a negative flight path angle and this leads to again cancellation of the sign, and results in positive wind shear energy.

For this example, the total power used per horizontal distance travelled was 3.5% less than the total power used per horizontal distance travelled used when the powered sailplane covered the same distance by flying, in wind shear, in a straight line at 25 m/s (minimum drag speed) using a thrust of 116 N at the minimum altitude covering a horizontal distance of 1200m.

Table 5.4.1 compares the results of the two modes. In case of the loitering mode the total power used per total time in the air is compared when the same loop is executed with using wind shear and travelling at the minimum drag speed of $25m/s$. The results of dynamic soaring using a small UAV are described in Appendix D. The saving achieved for various

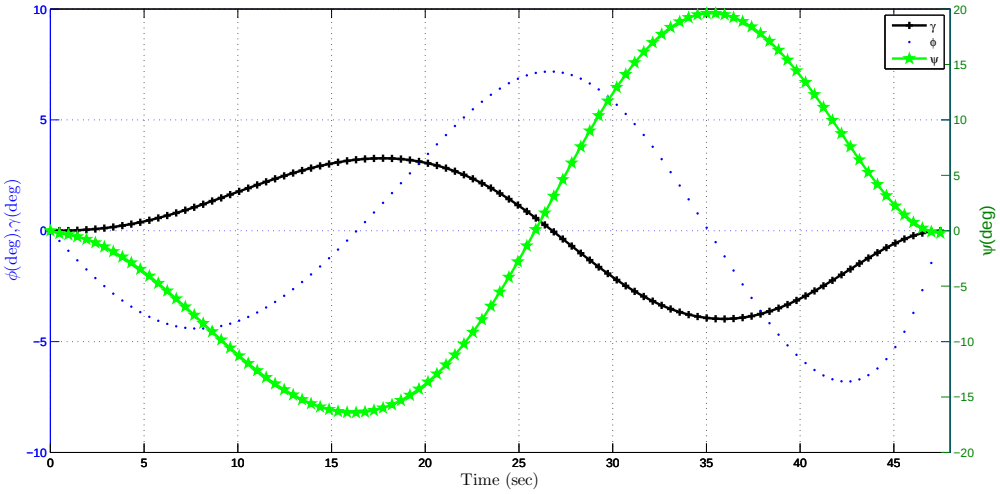

Figure 5.3: Flight path, bank and heading angles for crosswind travelling

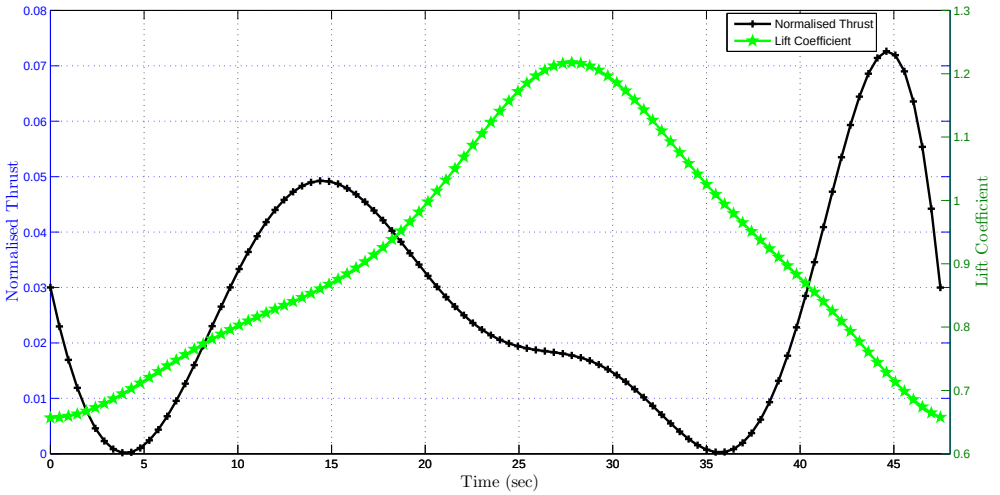

Figure 5.4: Thrust and lift-coefficient for crosswind travelling

crosswind solutions ranged from 3.5% to 8.5% and for the loitering mode from 4% to 6%. An interesting outcome of the project is the energy savings from sinusoidal cruise motion. When we compare fuel savings with a straight line flight from point A to B by flying a sailplane at the minimum drag speed then the feasible modes for crosswind are trajectories close to the straight line. If the sailplane spends too much time in the wind by executing a full turn in the wind, the total thrust usage becomes higher. These trajectories save fuel by executing sinusoidal cruise in wind shear. The total cycle time is also not very different from the straight line motion. The savings from the sinusoidal cruise motion was demonstrated in the 6DoF model by following the crosswind trajectories in absence of any wind shear and the results are presented in Chapter 6.

The plots for the crosswind case when 8.5% savings were achieved are presented in Figures 5.7 to 5.12. The plots for point mass analysis of loitering mode are presented in Appendix D

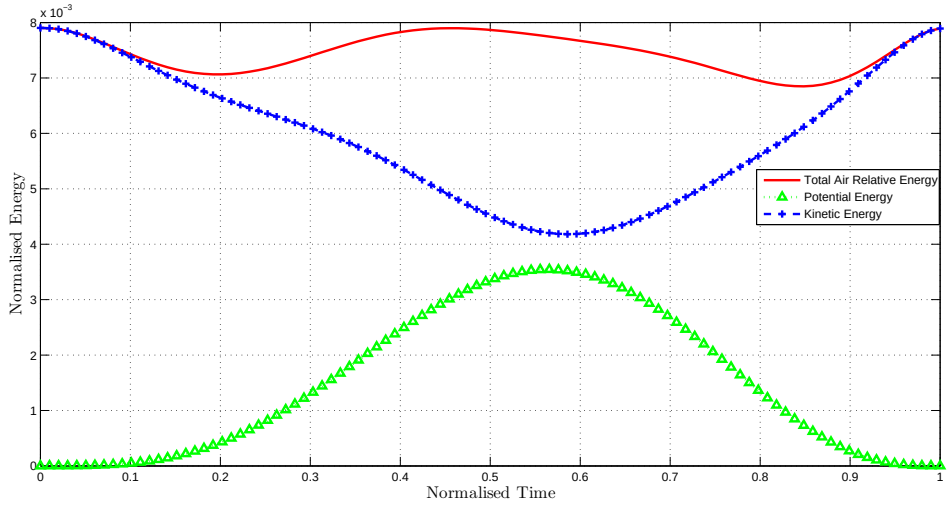

Figure 5.5: Energy for crosswind travelling

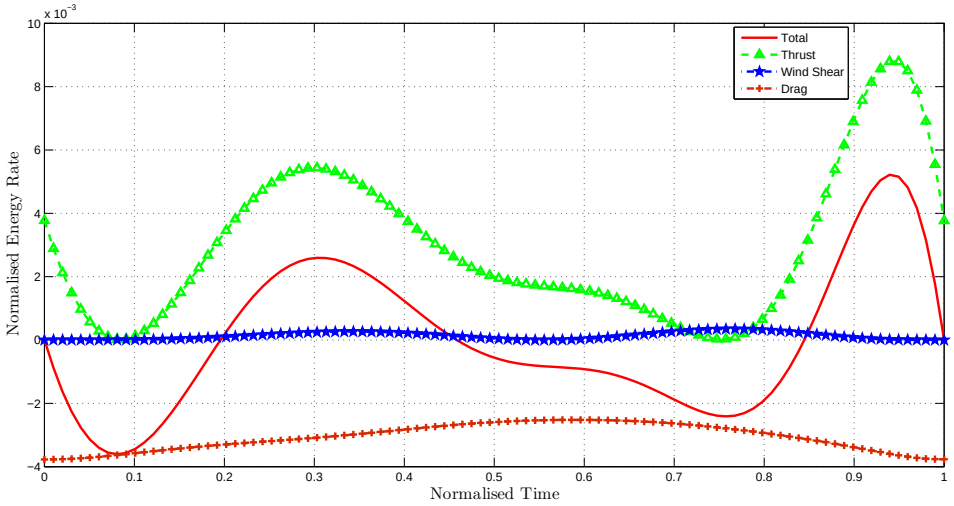

Figure 5.6: Energy rate for crosswind travelling

m(kg)	$W/S(kg/m^2)$	Crosswind savings(%)	Loitering savings(%)
430	36.8	3.5 to 8.5	4 to 6

Table 5.1: Fuel Savings

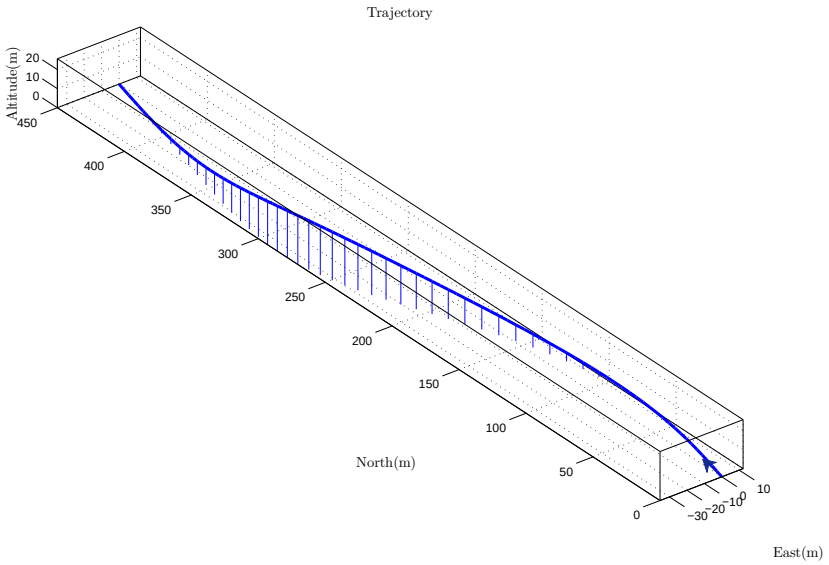

Figure 5.7: Optimal trajectory for crosswind travelling

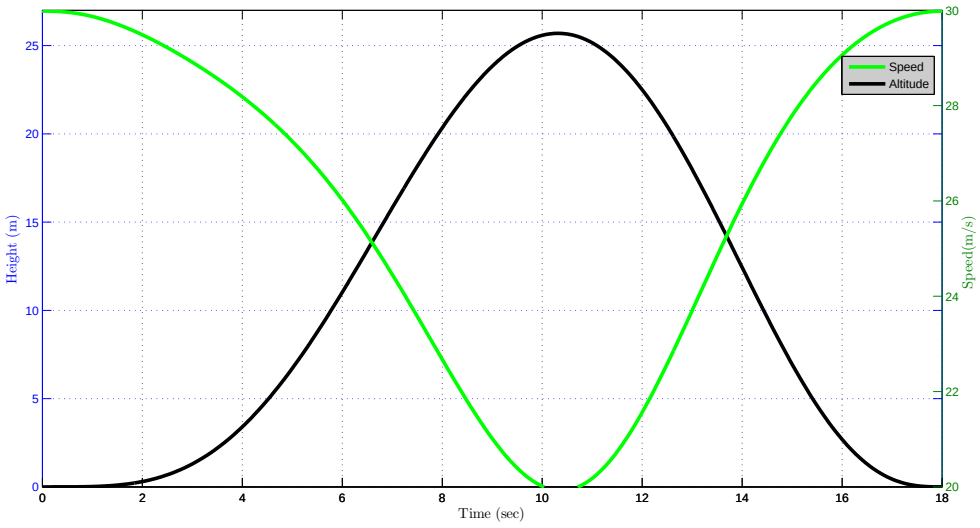

Figure 5.8: Altitude and speed for crosswind travelling

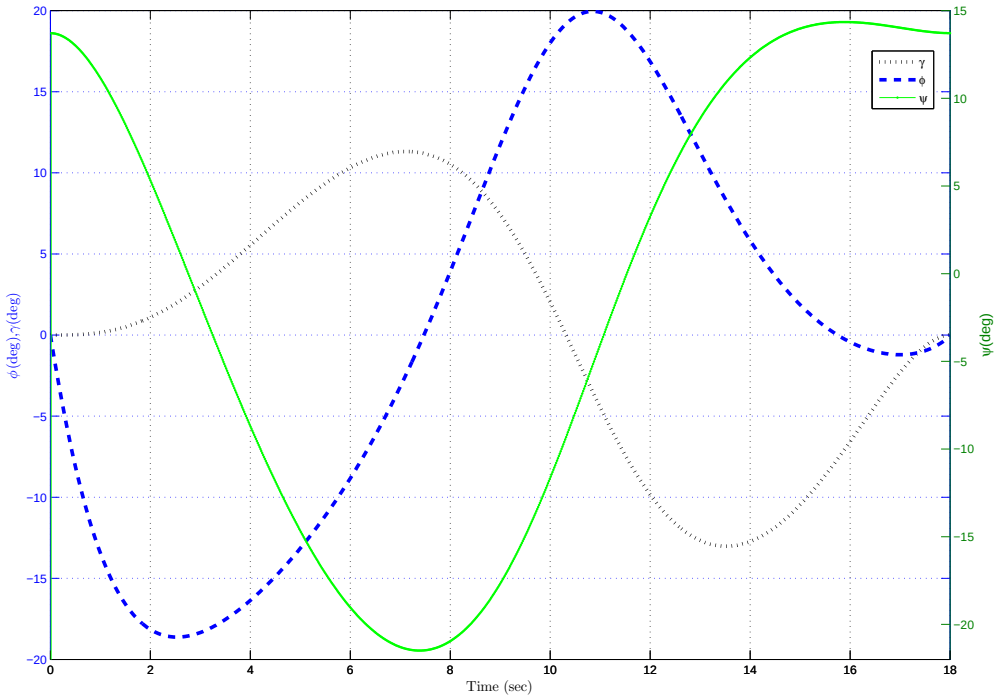

Figure 5.9: Flight path, bank and heading angles for crosswind travelling

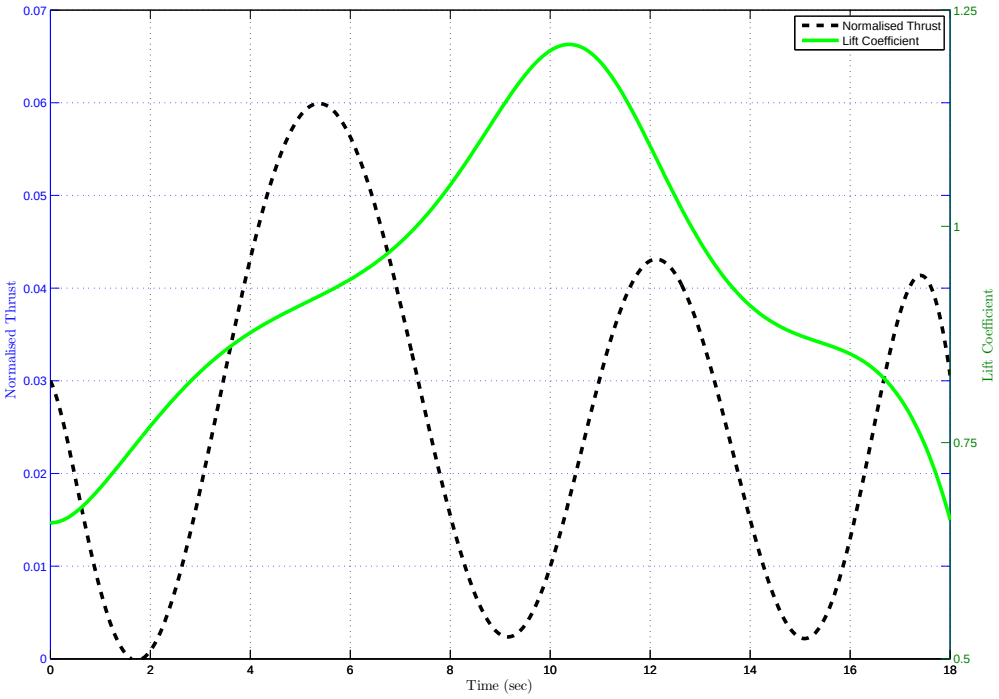

Figure 5.10: Thrust and lift-coefficient for crosswind travelling

Figure 5.11: Energy for crosswind travelling

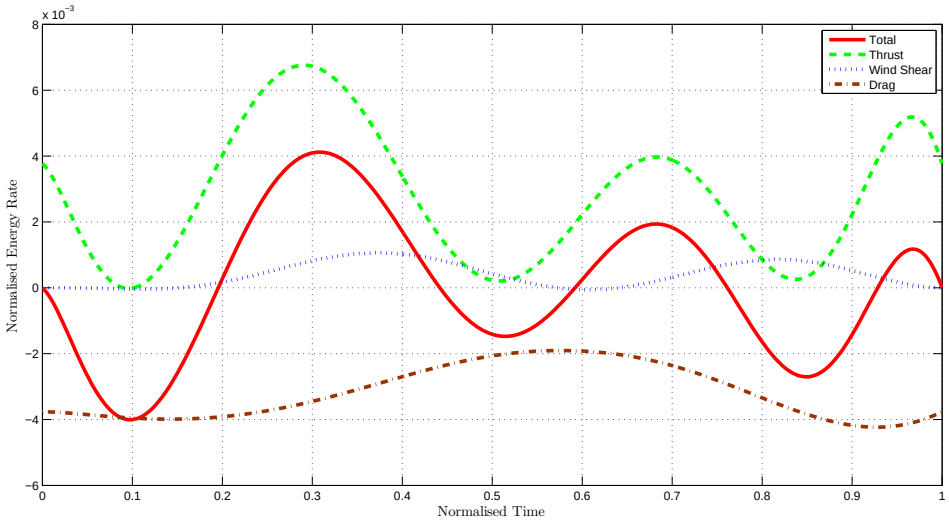

Figure 5.12: Energy rate for crosswind travelling

5.5 Conclusions

1. The IDVD method has a clear benefit because it can be implemented in real-time as the optimization time is just eight seconds compared to a trajectory loop time between 20 and 1000 seconds depending on the cost function. This short optimization time would allow computation of the next loop during the current trajectory loop. The estimation of the shear characteristics for the previous loop are used.

2. Wind shear estimation was carried out using least squares method for each dynamic soaring cycle so that these results could be used for the next dynamic soaring trajectory calculation.

3. The results of the crosswind travelling mode demonstrated a total power saving per horizontal distance travelled of 3.5% for the chosen example. The trajectories generated for the travelling problem are successfully followed in the 6DoF powered sailplane model simulation and they validate the point mass model results, by demonstrating 3% to 12% savings in the energy used per length of the horizontal distance travelled. The more aggressive trajectories for the crosswind mode resulted in the savings of up to 8.5%.

4. In the case of the loitering mode, a 6% total power saving per total time in air is achieved compared with the powered sailplane executing the loop without utilizing the wind shear. The saving is achieved as a result of lower thrust usage and lower airspeed.

5. The solutions for crosswind travelling are close to a straight line and the time to complete a cycle is not very different from that for straight line motion. Therefore fuel saving is achieved without compromising the time to complete a cycle.

6. The main disadvantages of the IDVD method are that sub-optimal solutions are generally obtained, and that there is no guarantee that feasible solutions are obtained. In such cases, the last obtained feasible trajectory can be used for the next loop and repeated until a feasible solutions is obtained.

Chapter 6

6DoF Model and Simulation

6.1 Introduction

A high fidelity sailplane model was used to demonstrate the ability of a controller to extract energy from atmospheric thermals and wind shear. A brief description of the air vehicle and the data flow diagram of the 6DoF model, developed by Amrane [Amr05] is provided. Extensive testing of the positioning algorithm for thermal soaring applications and validation of the point mass model based fuel saving trajectories were carried out in the 6DoF model and results are presented in this chapter. The changes made in the 6DoF model to carry out these tasks are also described in this Chapter.

The equations of Forces and Moments used in the non-linear 6DoF model are presented in Appendix A.

6.1.1 Air Vehicle

A non-linear 6DoF flight dynamics model based on the ASH 26E, a high performance sailplane, was developed in Simulink. See Table 6.1 for a list of the key dimensions and Figure 6.1 for the dimensions of the wing. (Forces and moments generated by various components of the sailplane were estimated using classical methods provided by ESDU data sheets, see appendix A). As the thermal strength varies with radius its effects will not be constant along the wing span. Consequently, two dimensional strip theory was used to determine the total aerodynamic forces produced by the wings and tailplane[Amr05]. This was achieved by taking into account the induced angle of attack across the span or at the aerodynamic center in the case of the tail surfaces. The wing was divided into discrete sections, and it was assumed that no interaction occurred across section boundaries. Local air velocities u_P^b, v_P^b and w_P^b were obtained in body axis for each wing station by combining the vehicle motion with the thermal gust field. Air angles α_P and β_P were found from these velocities and used to determine the elemental forces and moments acting on the two dimensional aerofoil section.

Parameter	Value
Mass	430.00 kg
Wing span	18.00 m
Wing area	11.69 m^2
Wing aspect ratio	26.67
Tailplane span	2.85 m
Tailplane area	0.99 m^2
Fin area	0.98 m^2
Fin height	1.23 m
Fuselage length	7.05 m

Table 6.1: Sailplane Data

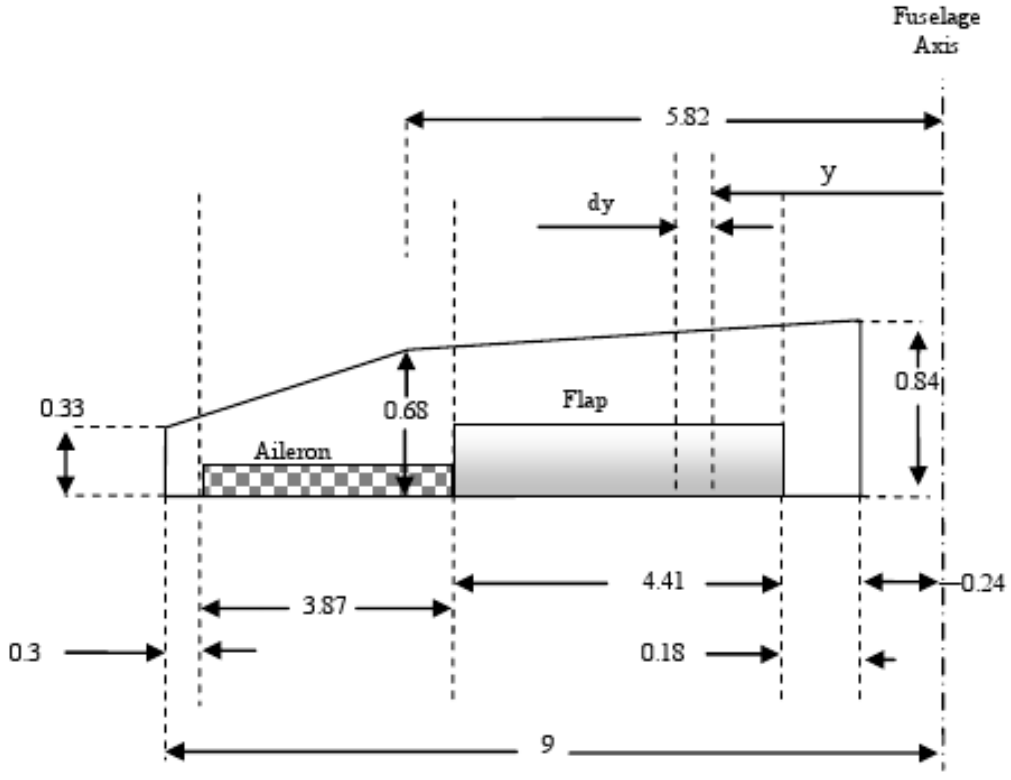

Figure 6.1: Dimension of wing[Amr05]

The accuracy of the sailplane model was enhanced by expressing the wing section drag coefficient, see Figure 6.2 as a cubic function of the lift coefficient[Tho99][1].

$$C_{D_{wg}} = \frac{1}{10^4}\left(28C_L^3 - 40C_L^2 + 35C_L + 53\right). \tag{6.1}$$

When required the drag polar for the whole aircraft was obtained by adding zero-lift contributions from the stabilizer, fin and fuselage. A global value for the induced drag was estimated assuming an elliptical lift distribution, thus:

$$\begin{aligned} C_D &= \frac{1}{10^4}\left(28C_L^3 - 40C_L^2 + 35C_L + 132\right) + \frac{C_L^2}{\pi A}, \\ C_D &= \frac{1}{10^4}\left(28C_L^3 + 79C_L^2 + 35C_L + 132\right). \end{aligned} \tag{6.2}$$

A data-flow diagram for the 6DoF model is shown in Figure 6.3, note that standard rigid-body equations of motion are used.

The ASH 26 simulation model has a 74 KW engine, composed of two blades of 1.5 m diameter [Amr05]. The advance ratio of the engine is defined as:

$$J = \frac{V}{ND} \tag{6.3}$$

where V is the airspeed of the sailplane, D is the propeller diameter and N is RPM of engine.

An expression for analytical curve filled to the experimental data in the range $J = 0.4$ to $J = 1.6$ is provided in Amrane's report [Amr05]. The propeller efficiency for two blades is:

$$\eta = 0.2109J^3 - 0.8718J^2 + 1.2100J + 0.3120 \tag{6.4}$$

The thrust is calculated using the estimated efficiency η using the following relationship:

$$T = \eta\frac{P}{V} \tag{6.5}$$

Due to the compact nature of the engine the drag generated was ignored. P is the power of the engine in the above equation.

A model validation was carried out by first considering the wings level flight and spiral glides, see Figures 6.4 and 6.5. The results of sink speed, at airspeeds of interest from the full 6DoF model were compared with the values obtained using only the drag polar described in equation (6.2). Airspeed in turn, sink speed in turn and radius of turn is described by equations (4.16) to (4.18). The results are presented in Figure 6.4, and they show a close match. Then similarly a spiral flight was considered and the sink speed airspeeds of interest during the trim state were compared. The result match closely and they are presented in Figure 6.5.

[1]Data for a FX-67-K-150 airfoil was used as this mostly closely matched the actual airfoil fitted to the ASH 26

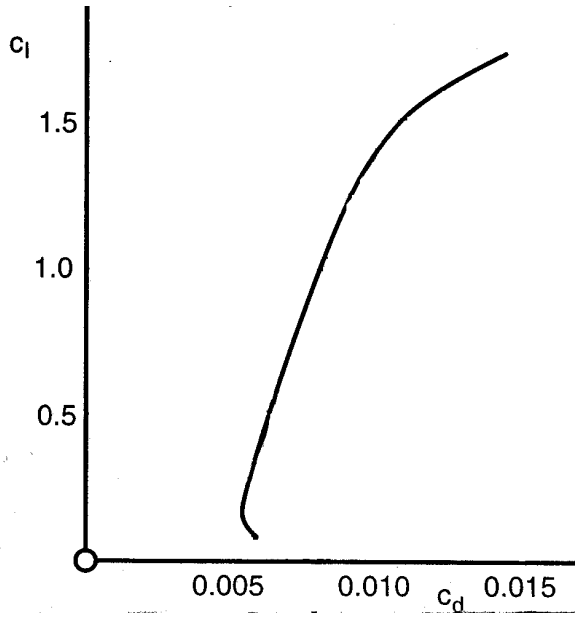

Figure 6.2: Airfoil polar [Tho99]

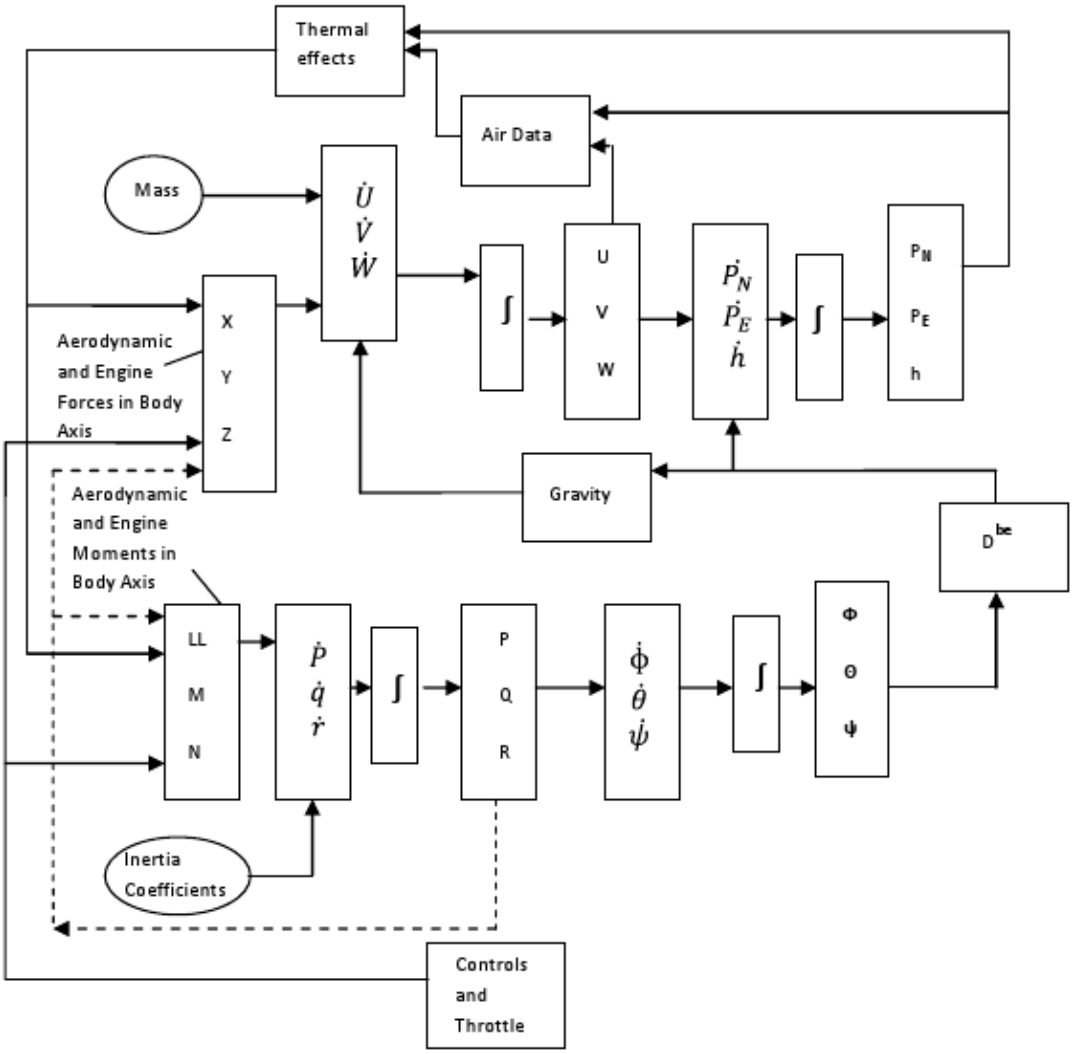

Figure 6.3: Data flow diagram [Amr05]

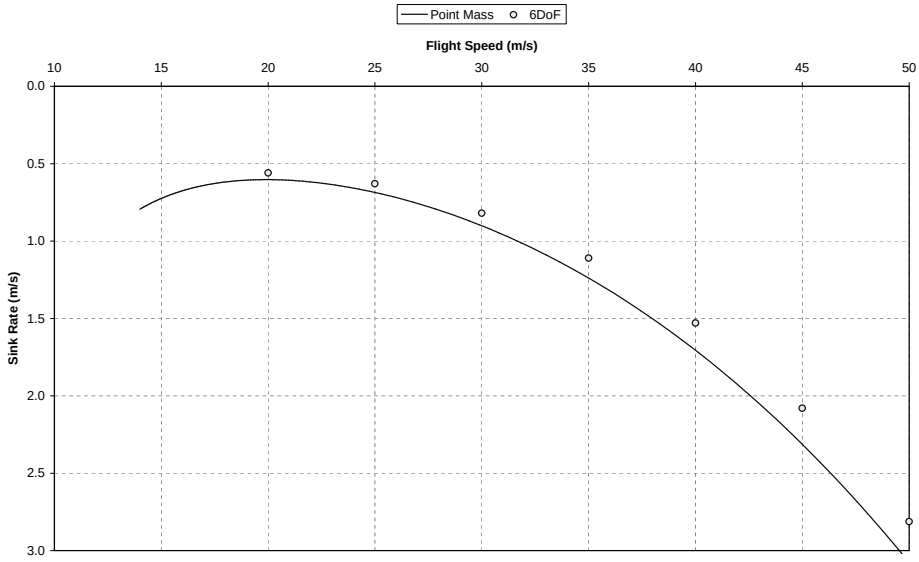

Figure 6.4: Data Validation wings level glide

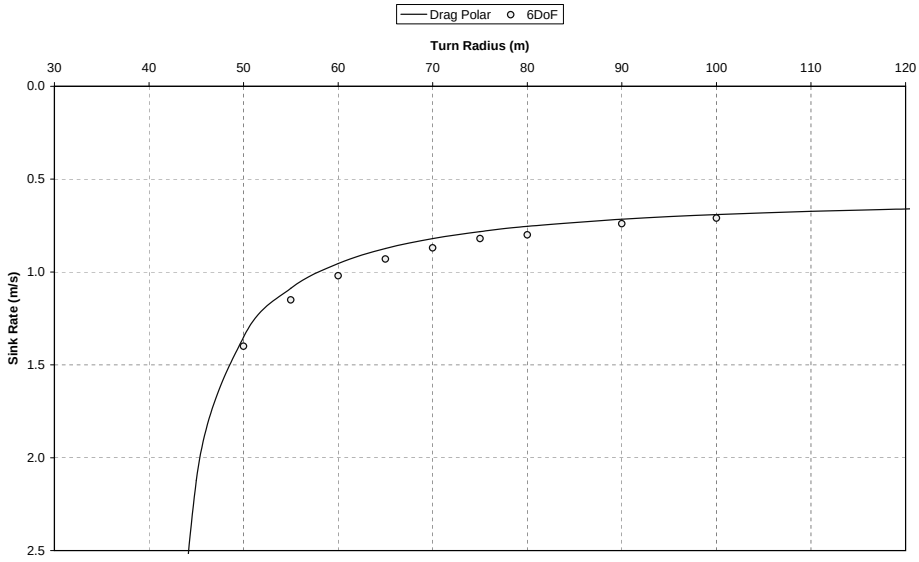

Figure 6.5: Data Validation spiral glide

6.2 Changes made for thermal soaring demonstration

A thermal soaring controller architecture can be seen in Figure 6.6. The speed command in the architecture is generated by an autopilot and is based on the analysis in Chapter 4 that determines the optimal speed required while in a bank. The altitude and speed measurements are used to calculate the rate of change of total energy and this information is passed to the positioning algorithm module. Once the presence of a thermal is confirmed by the variometer signal, then the positioning algorithm generates the bank angle commands. The positioning algorithm is explained in detail in Chapter 4.

An improvement was made in the positioning algorithm by addition of turning logic that determined the orientation of the sailplane with respect to the thermal center, see Figure6.7. The logic decides whether the sailplane is on the left or right side of the thermal center by examining the variometer and aileron input. When a sailplane enters a thermal it experiences more lift on the inner wing and would be banked out of the thermal. However when the autopilot is engaged it cancels the rolling effects of the thermal by deflecting the ailerons. The command of the autopilot to ailerons identifies the roll direction and hence the orientation of the thermal. A reading of a variometer is also used to confirm that the rolling disturbance is caused by a thermal up draft and not from turbulence.

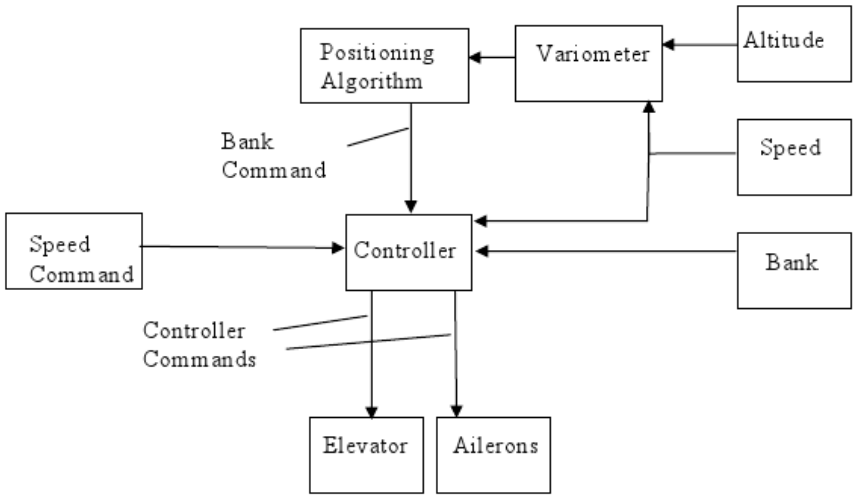

Figure 6.6: Thermal soaring controller architecture

The inner control architecture for the flight control system is used for stability augmentation and is explained in Chapter 4 and is based on the work of reference [CCW06].

A PI controller for the tracking of bank commands is shown in Figure 6.8. The error between the reference bank and actual value is passed to the PI controller to calculate a roll command. The following equation describes the controller:

$$\epsilon_{phi} = \phi - \phi_{ref}. \tag{6.6}$$

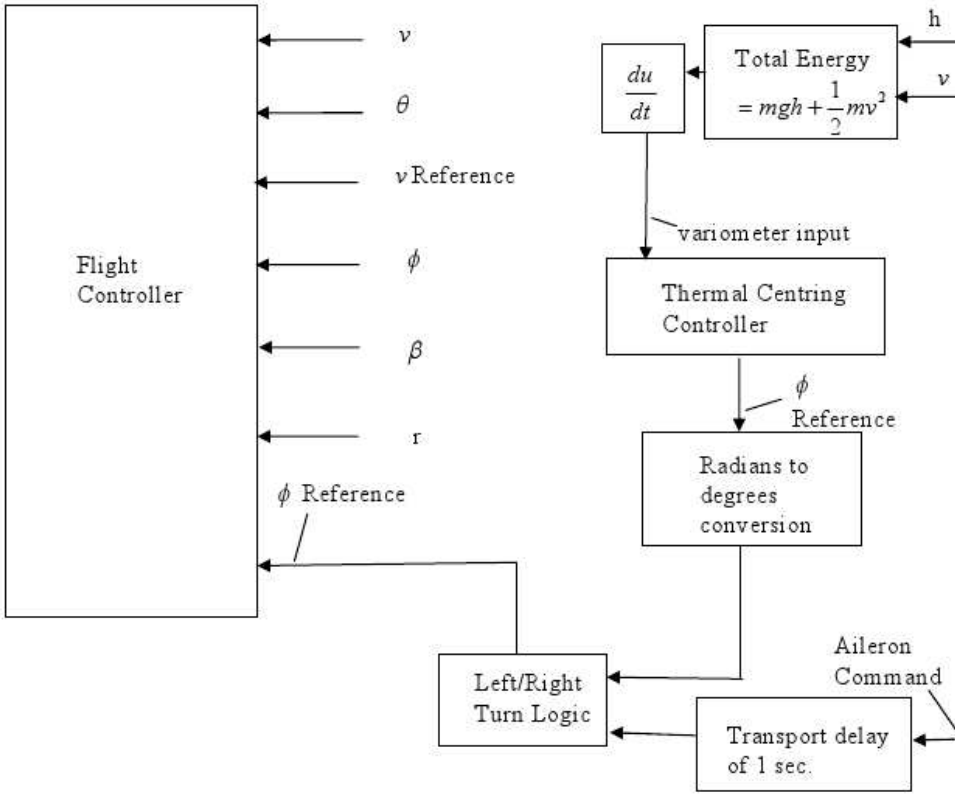

Figure 6.7: Thermal positioning controller

$$\xi = \int (K_{I_\phi} \epsilon_\phi + K_{p_\phi} \epsilon_\phi) dt. \tag{6.7}$$

A thermal soaring speed controller is shown in Figure 6.9, the speed is controlled using elevators and a PI scheme is used in the controller. The reference speed is adjusted by a factor while in a turn as shown by the following equation:

$$\epsilon_V = \frac{V_{Reference}}{\sqrt{\cos \phi}} - V. \tag{6.8}$$

$$V_{Command} = \int (K_{I_V} \epsilon_V + K_{p_V} \epsilon_V) dt. \tag{6.9}$$

The proportional and integral gains for both controllers were tuned manually to ensure an adequate step response. The remaining gains and time constants were based directly on Cook [CCW06] because of the similar sizes of the vehicles, see Table 6.2. A bank angle input is also

Gain	Value
K_{ari}	0.75
K_r	-0.90
K_{i_β}	0.01
K_{p_β}	0.80
K_{i_V}	0.01
K_{p_V}	0.20
K_ϕ	-0.48
K_θ	-0.20
T_a	0.05 s
T_r	5.00 s
T_θ	20.00 s
K_{p_ϕ}	-0.88
K_{i_ϕ}	-0.09

Table 6.2: Controller Gains

used by the controller to adjust the demand according to changes in the bank angle. All the controller gains are obtained using a tuning method, except for the inner control architecture which can be obtained from reference [CCW06]

6.3 Results of Thermal Soaring

The three positioning algorithms type A, type B and type C used in the simulations are:

- Type A, commands a bank angle of 35° and lowers the bank for three seconds after a heading of 154° and the turning logic is not included.
- In type B, command a bank angle of 35° lowers the bank for three seconds after a heading of 154° and the turning logic was included.
- In type C, algorithm commands a bank of 42° on detection of a thermal, lowers the bank for three seconds after a heading of 154°, when the thermal was lost and a turning

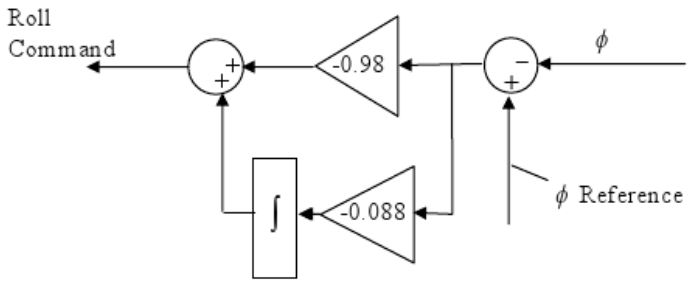

Figure 6.8: Bank controller

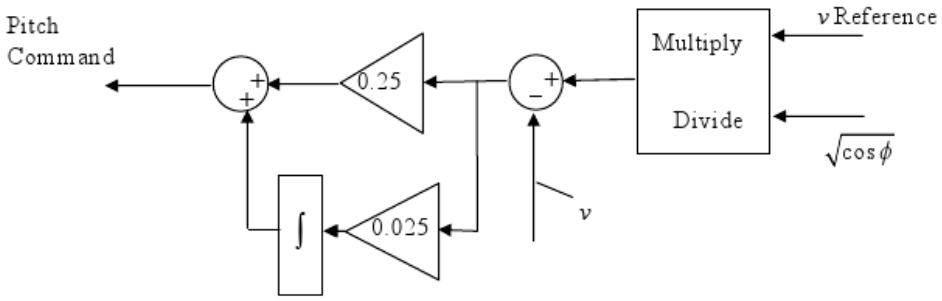

Figure 6.9: Thermal soaring speed controller

logic that determined the sailplane orientation with respect to the thermal center was included.

The simulations carried out to test the ability of three positioning algorithms using Woodward's and Carmichael's models are described in this section. First three different positions are used to enter a thermal using Woodward's model, where the sailplane entered from the left, right and the center line of the thermal, and turning in a thermal with a bank angle of 42°. In the case of the Carmichael model, eight different positions to enter the thermals were used to test the performance of the positioning algorithm and turning with a bank angle of 35°. This bank angle was chosen because it gave the minimum sink rate as described in Chapter 4. The maximum updraft velocity in Woodward's model was 2.4m/s for both wide and narrow models. In Carmichael's wide model the maximum updraft velocity was 4.6m/s and in narrow model the maximum updraft velocity value was 6.20m/s.

$R_W(m)$	w (m/s)	$R_N(m)$	w (m/s)
0.00	4.63	0.00	6.20
25.00	4.42	15.00	6.10
50.00	3.39	30.00	5.50
75.00	3.33	45.00	4.25
100.00	2.26	60.00	2.80
125.00	0.95	75.00	1.00
145.00	0.00	90.00	0.00

Table 6.3: Carmichael Thermal Models

$\text{dist}_x A(m)$	δh	$\text{dist}_x B(m)$	δh
-120.00	148.00	-70.00	100.00
-100.00	158.00	-60.00	103.70
-70.00	166.80	-50.00	110.70
-40.00	157.90	-40.00	135.90
40.00	107.30	40.00	124.00
80.00	71.52	50.00	113.40
100.00	53.12	60.00	97.40
120.00	24.40	70.00	82.70

Table 6.4: Altitude Gained

6.3.1 Tests using Carmichael's Models

A 50 seconds simulation was initially run and the two dimensional trajectory is shown in Figure 6.10. The sailplane's initial position was east=0 m and south= 500 m. On entering the thermal at point A, it is detected by a total energy variometer, and a right bank of 35° was commanded by the positioning algorithm. The sailplanes crosses the edge of the thermal and at point C, after executing a turn of 154° the bank is lowered for three seconds and after which the sailplane resumes the turn. The bank angle tracking and the variometer output are shown in Figure 6.11. The green line shows the upper boundary value at which the presence of thermal is confirmed and the red line represents the lower boundary value at which the

thermal is considered to be lost. The third sub-plot in Figure 6.11 shows the output of the thermal display logic used in the simulations, where 1 means that a thermal is present and a value 0 means a sailplane is not in a thermal.

To demonstrate the ability of the positioning algorithm A, Carmichael's wide and narrow thermal models were used. Eight points were selected on the centreline, as thermal entry points. Plots for four tests are presented in this section and the results of altitude gained for all eight tests carried out using both thermal models are presented in Table 6.4. In the first case, see Figure 6.12, the sailplane entered the thermal from the right side at a distance of 120m from the thermal center. Initially the sailplane lost altitude, see sub-plot of Figure 6.12 as it was gliding toward the thermal. As before, the positioning algorithm after a heading of 154°, lowered the bank, see sub-plot in Figure 6.12 and moved the sailplane toward the thermal. The sailplane kept on edge cutting while trying to position itself in the thermal.

The starting position of the sailplane in the second test was 120 m from left of the center of the thermal. The red circle in the sub-plot of Figure 6.13, shows the boundary of a thermal with a radius of 145 m. When the thermal was detected by a total energy variometer a bank command of 35° was generated by the positioning algorithm, see Figure 6.13. The sailplane crossed the boundary of thermal while trying turning right and the positioning algorithm after a turn of 154°, commanded lowering of the bank angle for a few seconds, this brought the sailplane into the thermal again. This process was repeated and the sailplane kept on trying to position itself in the thermal. In this process, it resulted in edge cutting and oscillations were introduced, see sub-plot of Figure 6.13.

The sailplane was made to enter the thermal at a distance of 70m from the right hand side of the thermal center. In this case the Carmichael narrow thermal and positioning algorithm A was used. The positioning algorithm A always commands a right turn on detection of a thermal. The sailplane crossed the boundary and this resulted in edge cutting that introduced oscillations in altitude and bank angle, see sub-plot in Figure 6.14. To further test the robustness of positioning algorithm A the sailplane entered was made to enter the thermal from 70m left of the thermal center. The Carmichael's narrow thermal model was used. The sailpane's turn was not tight enough as bank angle of 35° was used and it kept on edge cutting as the positioning algorithm was trying to place it in the thermal. The edge cutting and crossing the regions of varying up draft strength introduced oscillations in the bank angle and altitude. In the bank angle the large oscillations are due to the lowering of the bank angle and the small amplitude more frequent oscillations are due to the edge cutting and crossing the regions of variable up draft strength. The altitude gained, trajectory and bank angle can be seen in Figure 6.15.

The sailplane entered from the right hand side of the thermal from a distance of 70m from the thermal center. The Carmichael narrow thermal model and positioning algorithm B was used that also included a turning logic. The sailplane, on detection of the logic, made a left turn, as the turning logic worked out the orientation of the thermal center with respect to the sailplane. The sailplane on crossing the boundary, continued to circle and after a turn of 189°, lowered the bank angle for a few seconds, see sub-plot in Figure 6.16. The selection of

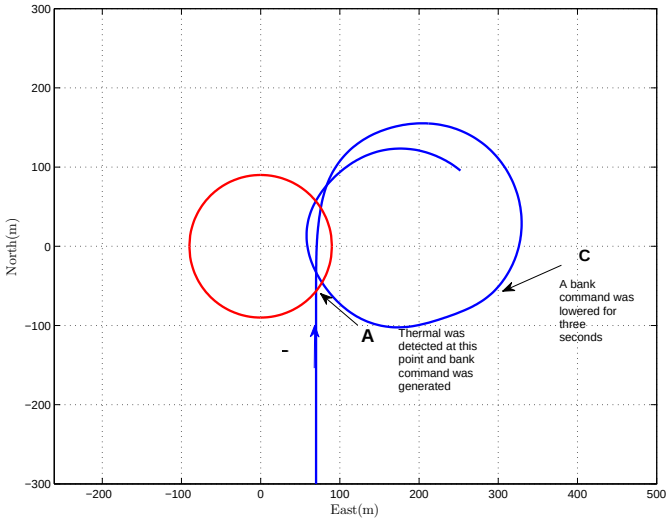

Figure 6.10: (Scenario test, trajectory)

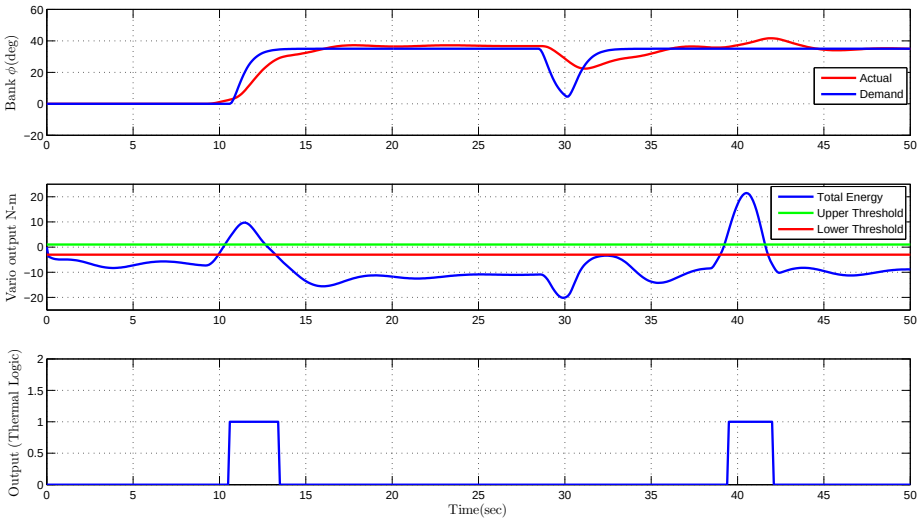

Figure 6.11: (Test, bank command)

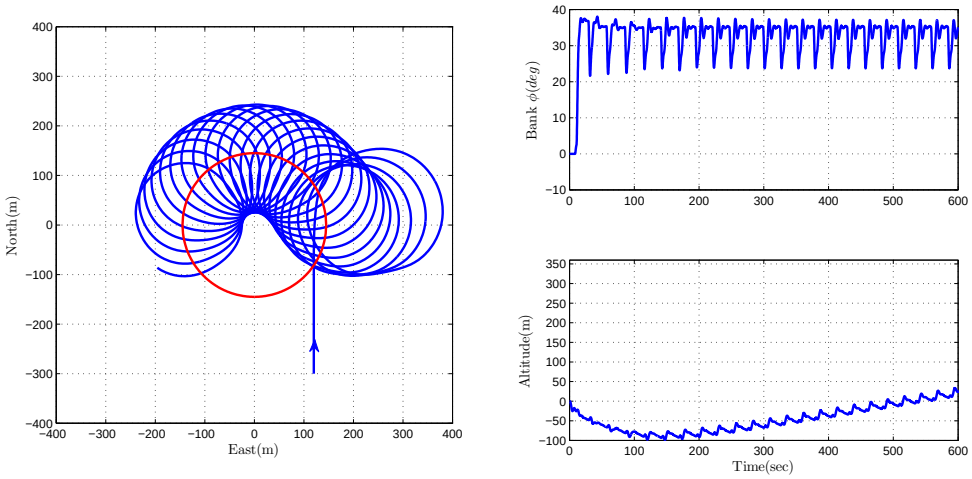

Figure 6.12: (Test 1, wide thermal)

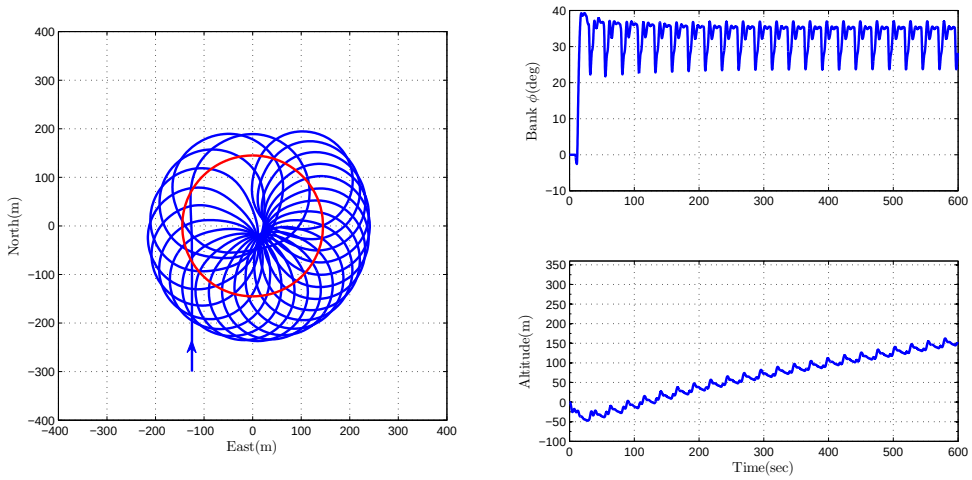

Figure 6.13: (Test 2, wide thermal)

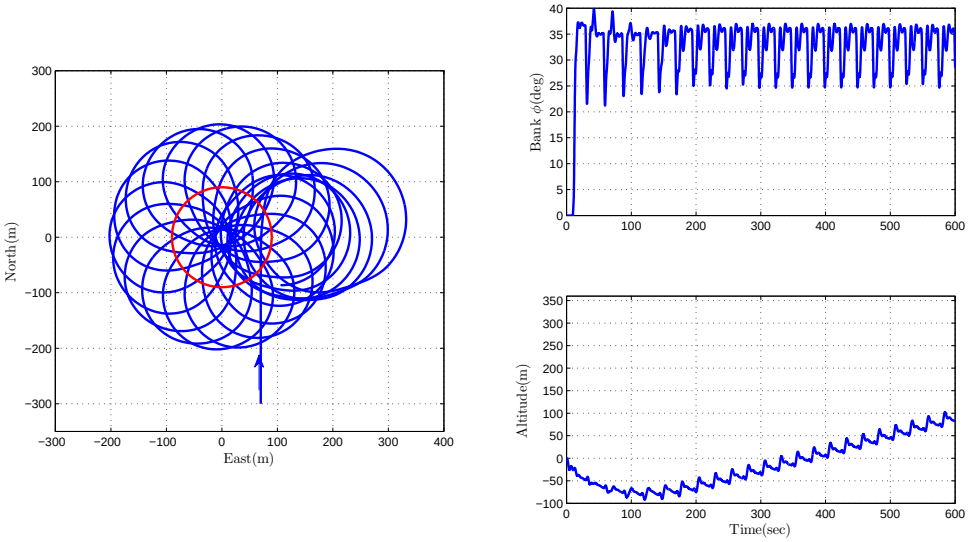

Figure 6.14: (Test 1, narrow thermal)

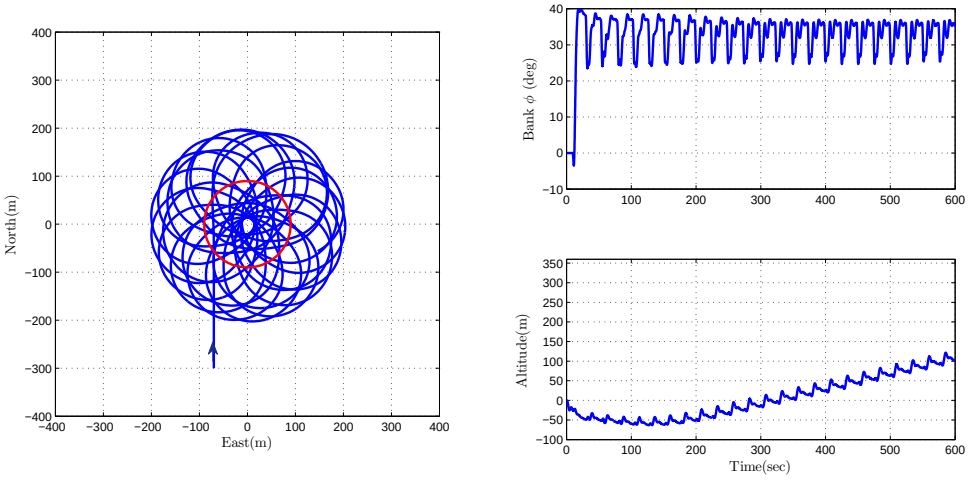

Figure 6.15: (Test 2, narrow thermal)

189° instead of 154° resulted in better performance in the case when a left turn is executed on entering a thermal. The sailplane approximately gained same height, in comparison when this test was carried out without using a turning logic. However heading of 154° was finalized as it resulted in positioning of sailplane in thermals once they were lost, for all the eight cases. The oscillations also resulted in the bank angle and altitude for the reasons described earlier. A test was then repeated again, using Carmichael's wide thermal and a turning logic (positioning algorithm B) but this time using the Carmichael's wide thermal. The sailplane entered from the right side of the thermal, and the positioning algorithm commanded 35° and this resulted in a left turn. The sailplane crossed the boundary and the process of thermal positioning, by lowering the bank was repeated, see sub-plot of Figure 6.17. The altitude gained is presented in sub-plot of Figure 6.17, the sailplane gained 54m, where as in the same scenario 24m were gained when positioning algorithm A was used. The sailplane circled the edge of the thermal and this performance could be further improved by tuning the heading angle for this particular thermal size however edge cutting would still result and a tighter turning would only position the sailplane in the thermal.

6.3.2 Simulations using Woodward's Model

Two different sizes of thermals, narrow and wide were used. The ability of positioning algorithm C, was tested by considering three entry points into a thermal. In first case, the sailplane entered from the center line, then it entered from the east of the center line and in the third case it entered from the west of the center line. The plots of these tests and results are summarized in this section.

These different entry points and wide and narrow thermals were used to test the performance of positioning algorithm C. This positioning algorithm had a turning logic that determined the orientation of the sailplane with respect to the center of the thermal. In the first case the sailplane entered the wide thermal from the center line. On entering the thermal, the sailplane turned right and crossed the boundary of the thermal, see Figure 6.18. The positioning algorithm managed to place the sailplane in the thermal after edge cutting for a few times. The bank angle and altitude gained are shown in Figure 6.18. The oscillations in the bank angle and altitude are due to edge cutting and crossing the regions of variable up draft strength.

In the second test, using the wide thermal, the sailplane's initial position was 120m right of the thermal center. On entering the thermal, the sailplane turned left, because of the turning logic's ability to determine the orientation of the sailplane with the thermal center. It managed to position itself in the thermal in first attempt, Figure 6.19 but the oscillations occurred due to the reasons described earlier. It gained 340m in 600 seconds.

In the third test, the sailplane's initial position was 120m from the left of the thermal center.It turned in the right direction towards the thermal center, when the thermal was detected. It crossed the boundary once but then managed to position itself in the thermal. An altitude of 252m was reached in 600 seconds, see Figure 6.20.

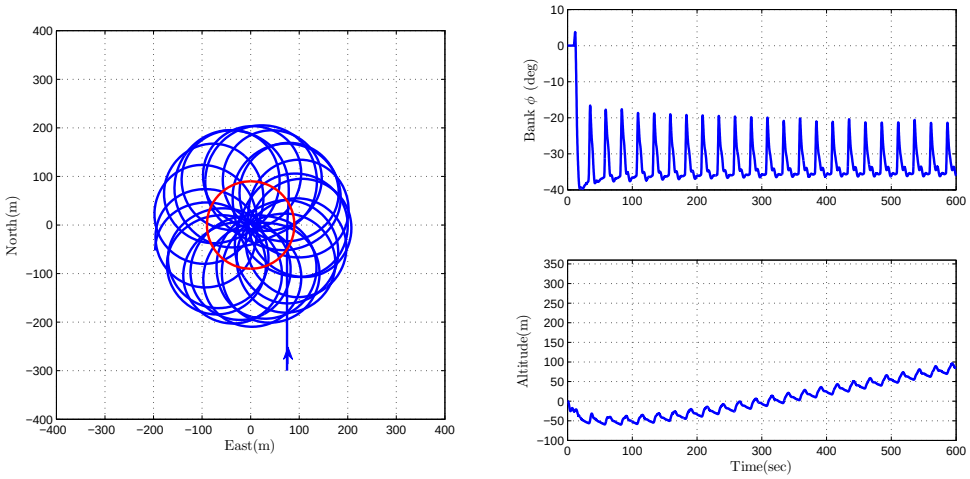

Figure 6.16: (Test, narrow thermal (turning logic used))

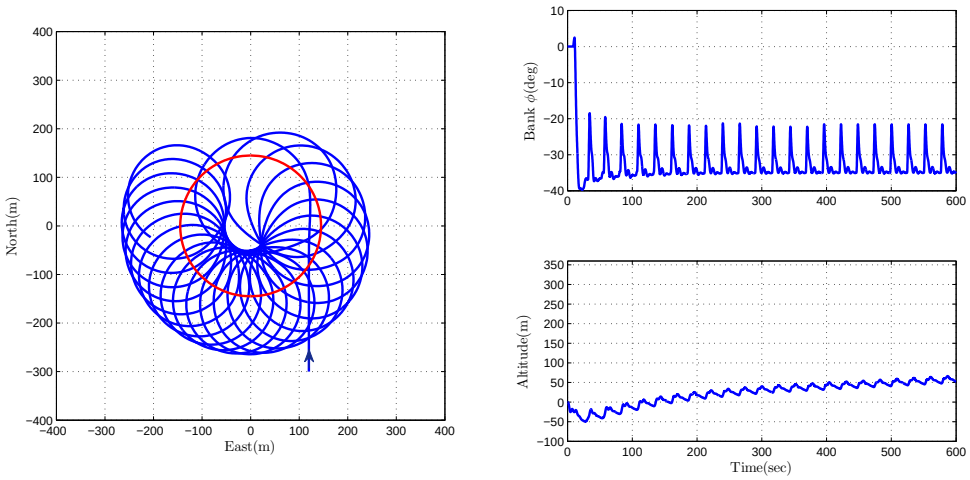

Figure 6.17: (Test wide thermal (turning logic used))

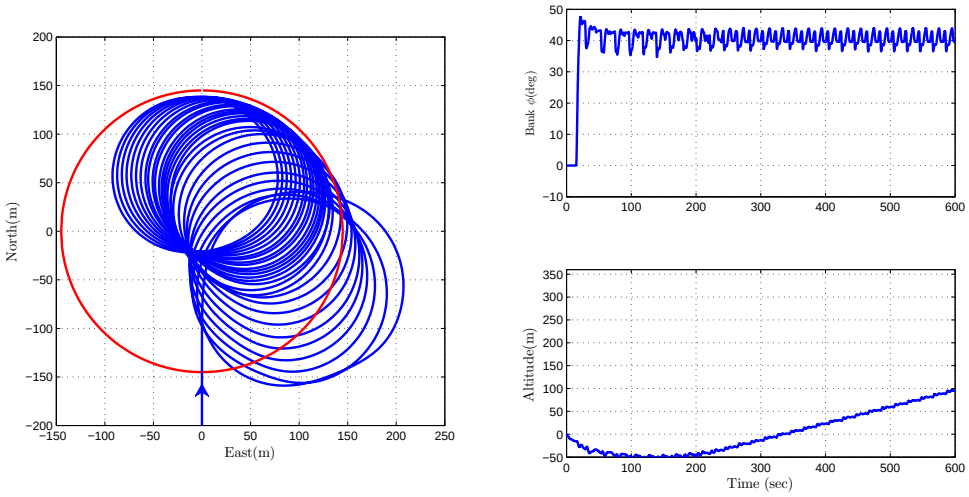

Figure 6.18: (Test 1, wide thermal)

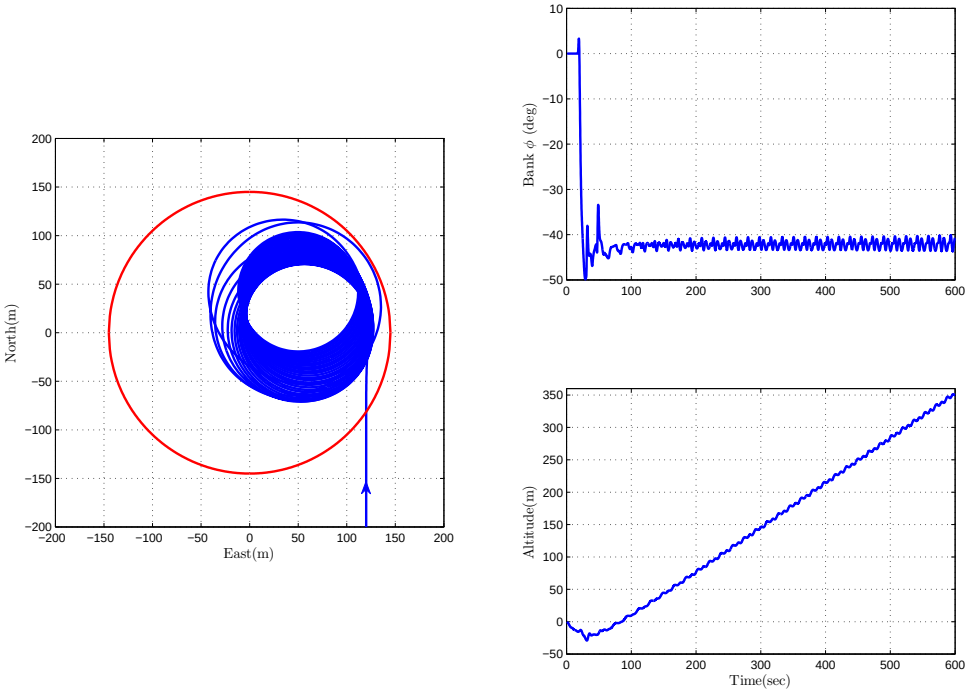

Figure 6.19: (Test 2, wide thermal)

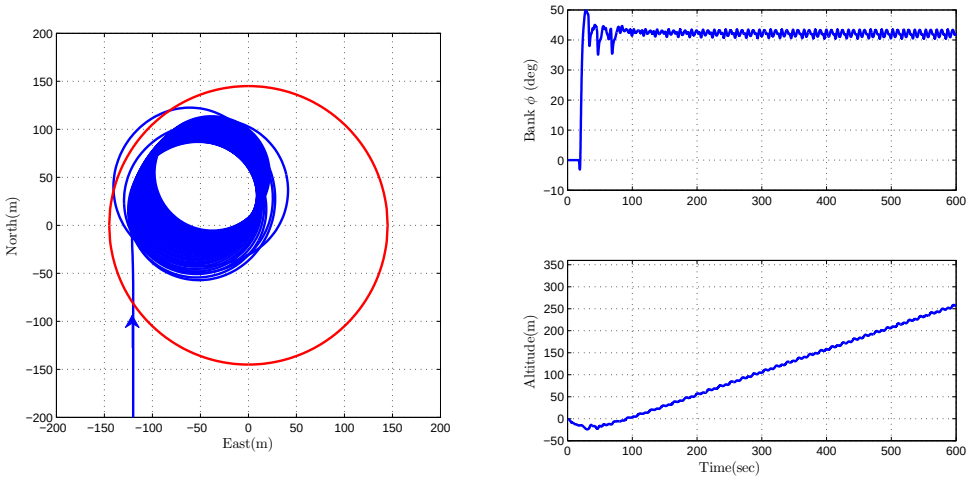

Figure 6.20: (Test 3, wide thermal)

The above mentioned three tests were also repeated but this time using narrow Woodward's model. Figure 6.21 shows the trajectory of the sailplane when it entered the thermal from the center line. It turned left but its not able to position itself in the first attempt as the thermal radius was small in this case. After a few attempts it managed to position itself in the thermal and gained 60m in 600 seconds.

The sailplane's initial position was set at 60m on the right of the thermal center. On entering the thermal it executed a left turn managed to position itself in the thermal in only two attempts, see Figure 6.22 and gained 150m in 600 seconds.

In the final test, the initial position of the sailplane was set 60m on the left of the thermal center. The sailplane turned right on entering the thermal and on exiting the thermal and managed to position itself in the thermal on the third attempt, see Figure 6.23, and gained 60m in 600 seconds. The oscillations ware also observed in the bank angle and altitude mainly due to the sailplane's crossing of the varying strength up-draft regions.

6.3.3 Summary

When the sailplane was made to enter 120m from the right side of the thermal center and the Carmichael model and positioning algorithm A were used, an average climb rate of 0.03m/s was achieved. The reason for poor performance was because no turning logic was included and the sailplane turned towards the right on detection of the thermal, regardless whether the thermal center was on right or left side. When the improved positioning algorithm B was used that included a turning logic, the sailplane made a turn in the correct direction and the average climb rate was 0.13m/s. When positioning algorithm C was used for these scenarios it resulted in an even better performance than positioning algorithm B and the sailplane achieved an average climb rate of 0.58m/s.

When the sailplane entered the thermal 120m from the left side of the thermal center, algo-

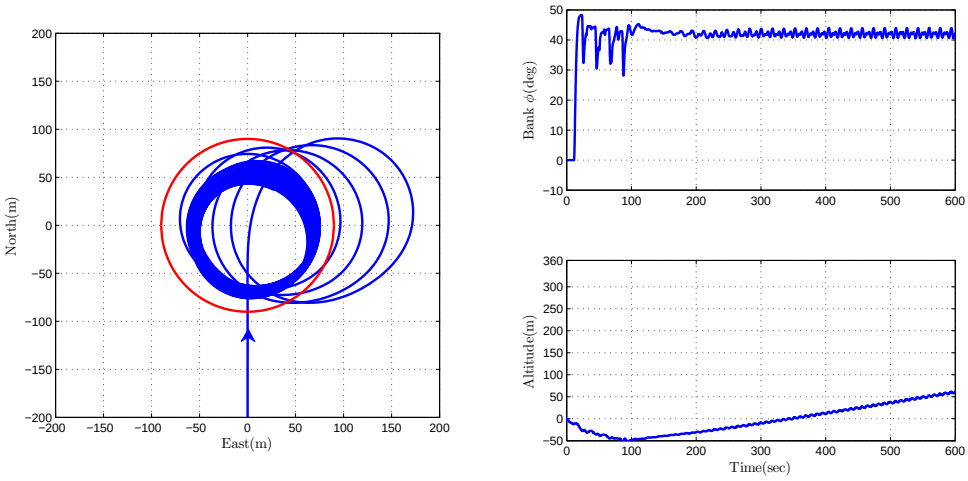

Figure 6.21: (Test1, narrow thermal)

Positioning algorithm	Thermal	dist$_x(m)$	Average climb rate(m/s)
C	wide,(Woodward)	120	0.58
C	wide,(Woodward)	-120	0.43
C	narrow,(Woodward)	60	0.26
C	narrow,(Woodward)	-60	0.10
A	wide,(Carmichael)	120	0.03
A	wide,(Carmichael)	-120	0.24
A	narrow,(Carmichael)	70	0.13
A	narrow,(Carmichael)	-70	0.17
B	wide,(Carmichael)	120	0.13
B	narrow,(Carmichael)	70	0.13

Table 6.5: Average Climb Rate

rithm A resulted in 0.24m/s because in this case the sailplane entered the thermal from the left side of the thermal center and a climb rate of 0.24m/s was achieved. However positioning algorithm C resulted in 0.43m/s as it resulted in tighter turns within the stronger part of the thermal. When the sailplane entered 70m from the thermal center from the right side, when the narrow thermal was used, positioning algorithm A resulted in 0.13m/s rate of climb and whereas the use of turning logic in positioning algorithm B did not improve the performance and also resulted in 0.13m/s climb rate. The turning logic made the sailplane turn in the right direction but because the thermal was small it resulted in edge cutting and because of large turns that resulted from using a bank angle of 35° the sailplane found it hard to circle within the thermal. Use of algorithm C in this case resulted in a climb rate of 0.26m/s. The sailplane managed to position itself in the thermal when positioning algorithm A was used with a bank command of 42°. When sailplane entered 70m from the left side of the center and narrow thermal was used, the positioning algorithm A resulted in a climb rate of 0.17m/s because it turned in the right direction in this case as the thermal center was on the right side. Use of positioning algorithm C in this case only resulted in a climb rate of 0.10m/s because the sailplane drifted towards the north and went outside the thermal initially.

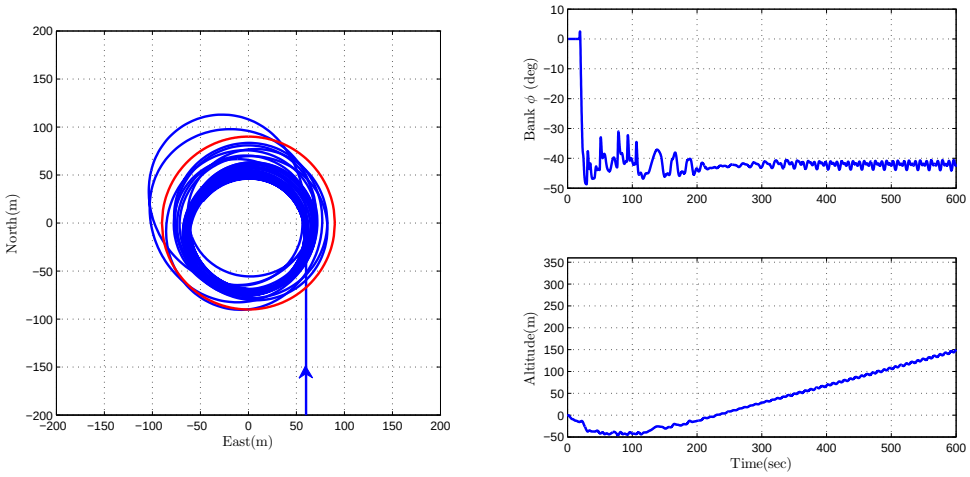

Figure 6.22: (Test 2, narrow thermal)

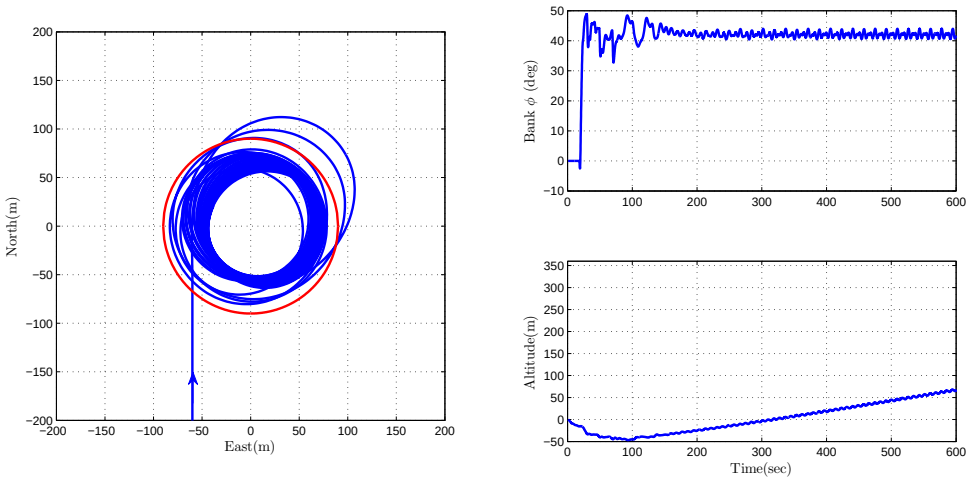

Figure 6.23: (Test 3, narrow thermal)

6.4 Changes made for dynamic soaring demonstration

A dynamic soaring architecture is described in Figure 6.24. A point mass model of a sailplane is used in the trajectory generation module. It uses estimated values of wind shear and a wind direction and then generates fuel saving trajectories. The trajectories generated are passed to the controller. The trajectory generation system passes, ground speed, bank angle demand, altitude command, *east* distance and *north* distance.

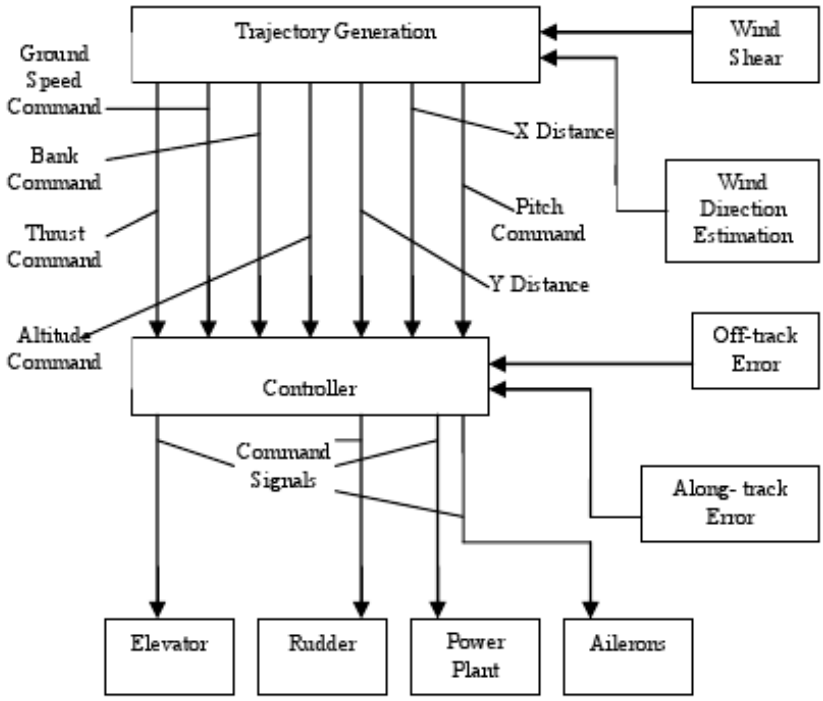

Figure 6.24: Dynamic soaring architecture

These commands are tracked by the controller, and we have used a 6DoF model to validate the trajectories generated. The off-track error is controlled by bank angle and the along track error is controlled by the ground speed.

Figure 6.25, shows the altitude controller for trajectory following. The altitude commands generated by the trajectory generation system are followed by the controller. The reference altitude is compared with the measured values; errors are fed to a PI controller, which generates pitch (radians) commands and these commands are passed to the second PI controller and pitch rate feed back value is subtracted from the output of the second controller. The resulting value is the demand for elevator defection in radians. This value is converted into degrees and then is passed to the elevators. Feed forward pitch values obtained from the reference trajectory are also used. The following equations describe the altitude controller

command calculation:

$$\epsilon_{alt} = h - h_{ref}, \tag{6.10}$$

$$\theta_c = \int (K_{I_{alt}} \epsilon_{alt} + K_{p_{alt}} \epsilon_{alt} + \theta_{input}) dt, \tag{6.11}$$

$$\epsilon_{theta} = \theta_c - \theta, \tag{6.12}$$

$$eta = \int (K_{_{theta}} \epsilon_{theta} + K_{p_\theta} \epsilon_{theta} + K_{q_\theta} q) dt. \tag{6.13}$$

The along-track error ate is calculated using the following formula:

$$ate = (P_u - P_t)' \frac{V_t}{\sqrt{V'tV_t}}, \tag{6.14}$$

$$\theta_1 = \text{atan2}(P_{ux} - P_{tx}, P_{uy} - P_{tY}) - \text{atan2}(V_{tx}, V_{ty}), \tag{6.15}$$

where the off-track error is defined as:

$$ote = \sqrt{(P_u - P_t)'(P_u - P_t)} \sin(\theta_1). \tag{6.16}$$

Where Pt is the vector describing the position of the trajectory and Pt_x and Pt_y are the x and y components. Vt is the velocity vector of the trajectory with Vt_x and Vt_y as it components. Where as Pu is the position vector of the UAV with Pu_x and Pu_y as its components in x and y direction respectively. These body velocities relative to air are then passed to the air data module.

The along-track controller is shown in Figure 6.26. The demand for the error is set equal to zero and is compared with the measured value of the error. The error values are passed to a PI controller and its output is added to the reference ground speed values. The demand for the ground speed is adjusted according to the along track error and a limiter is included to limit the adjusted reference ground speed values to between 20 m/s to 30 m/s. An anti-wind up logic is also used and if any the upper or lower limits are reached, the logic switches off the integral gain. The ground speed demand is then compared with the measured ground speed values and error is input to a speed proportional controller. The output generates the throttle demand and the throttle demand is also constraint between the values 0 and 1 using a limiter.

The off-track controller can be seen in Figure 6.27. The demand of the error is set equal to zero and is then compared with the off-track error. A PI controller is used and the desired bank angle obtained from the optimization program is added to the output of the controller and then passed as a bank angle command to ailerons.

The wind effects are added in Figure 6.28. In our case we have assumed that the up-gust component is zero and the wind has only a horizontal component. The wind is blowing from the North direction and the wind component angle is transformed into body axis by using a transformation matrix. The resulting wind speeds in body axis are described as u_w,v_w and w_w. These values are then subtracted from the velocity components of the sailplane in body

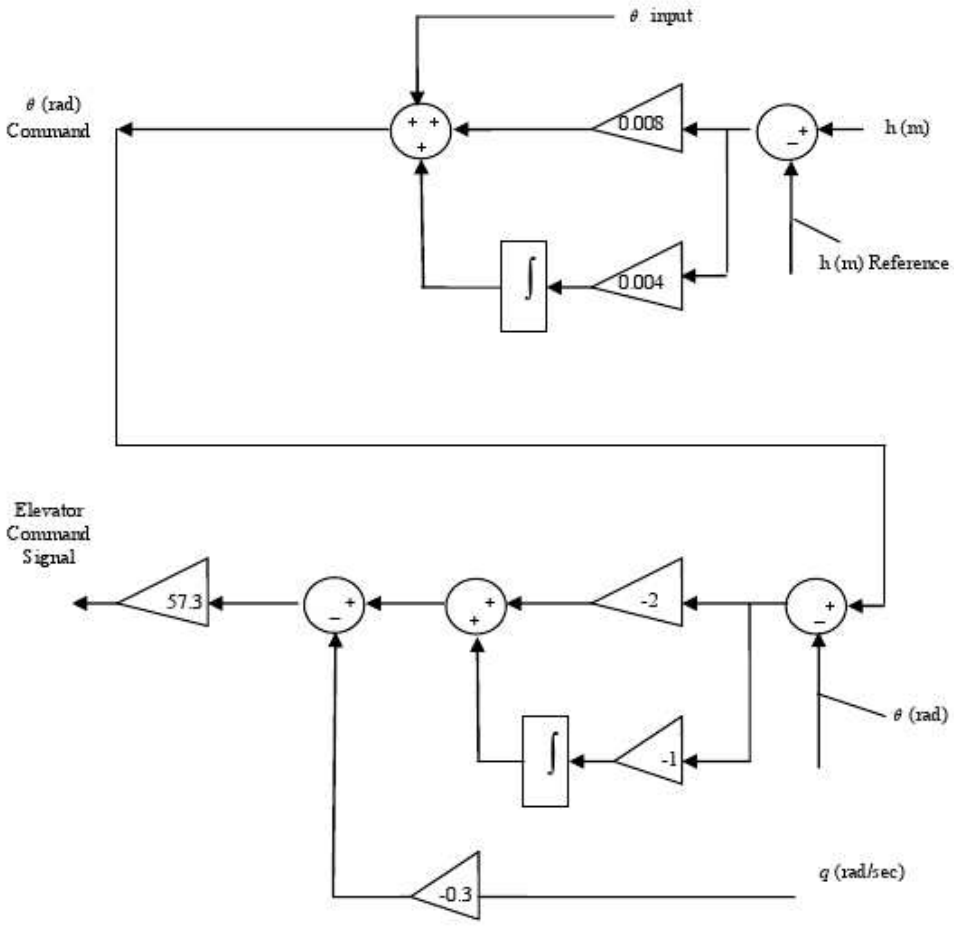

Figure 6.25: Altitude controller

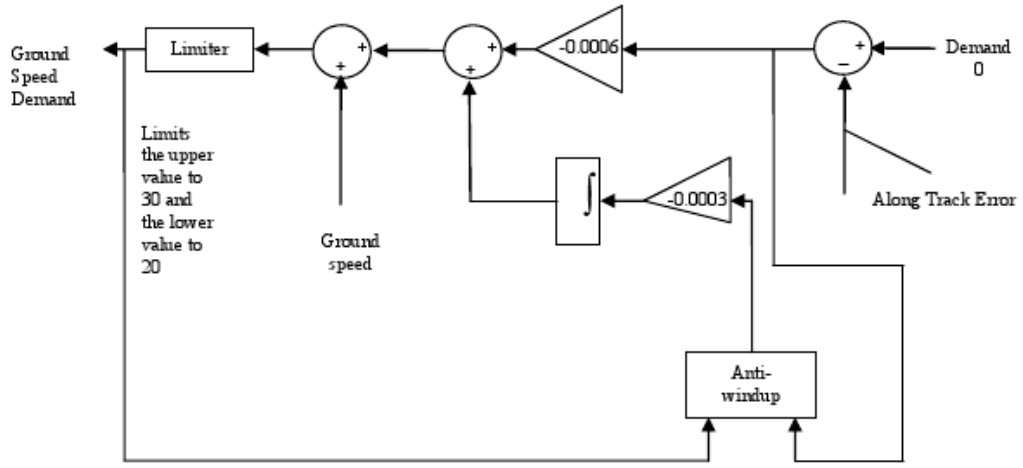

Figure 6.26: Along track controller

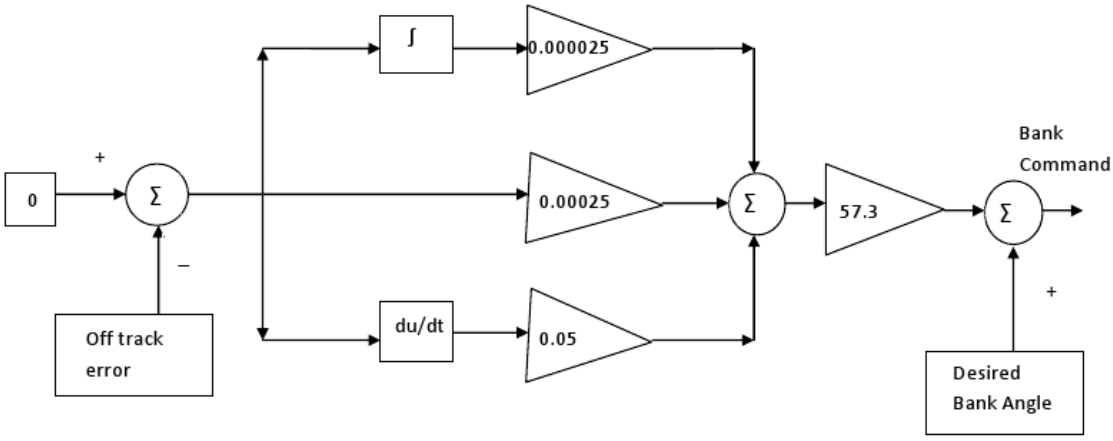

Figure 6.27: Offtrack controller

axis:

$$u_R = u - u_w, \tag{6.17}$$

$$v_R = v - v_w, \tag{6.18}$$

$$w_R = w - w_w, \tag{6.19}$$

where u,v and w are wind velocity components in the body axis and where u_R,v_R and w_R are the resultant velocity components in the body axis. Figure 6.29 describes the wind effect addition in the 6DoF model. W_N, W_E and W_D are transformed into body axis and then subtracted from the body velocities components U,V,W. These values are then passed to the air data module, where α, β, V_T are calculated. These values are used to calculate the aerodynamic forces and then passed to the equations of motion module.

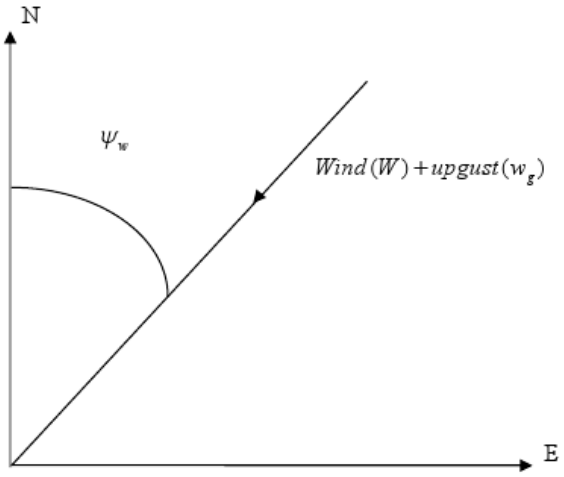

Figure 6.28: Wind heading

6.5 Validation of fuel saving trajectories

A trajectory following control system based on a classical control scheme was designed to test the ability of the control system to follow trajectories in SIMULINK. The trajectory following control system uses the trajectories of bank, thrust, airspeed, altitude, distance covered in east direction and distance covered in north direction and tracks them. The trajectories generated by the IDVD method for crosswind and loitering modes are validated in 6DoF simulation. This is achieved by following these trajectories in 6DoF simulations and comparing the results of the total power used per horizontal distance for the crosswind mode and the total power used per total time spent in air for loitering mode.

Figure 6.30 shows a three dimensional view of the desired and actual 6Dof simulation trajectories of the crosswind mode. Figure 6.31 shows the speed tracking output, where the desired and actual output values are plotted. A non-linear wind shear model (5.4) was used in the 6DoF simulations. This is used as an input to have comprehensive testing of the system when

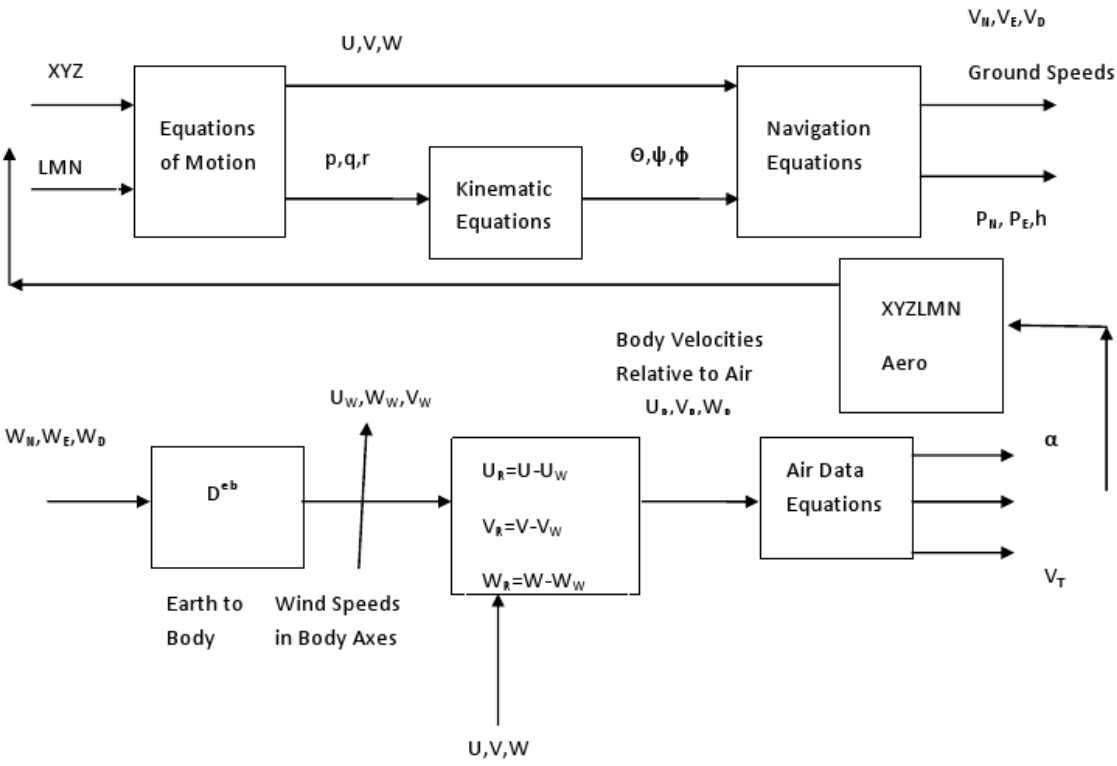

Figure 6.29: Wind effect addition

executing dynamic soaring cycles in the wind shear.

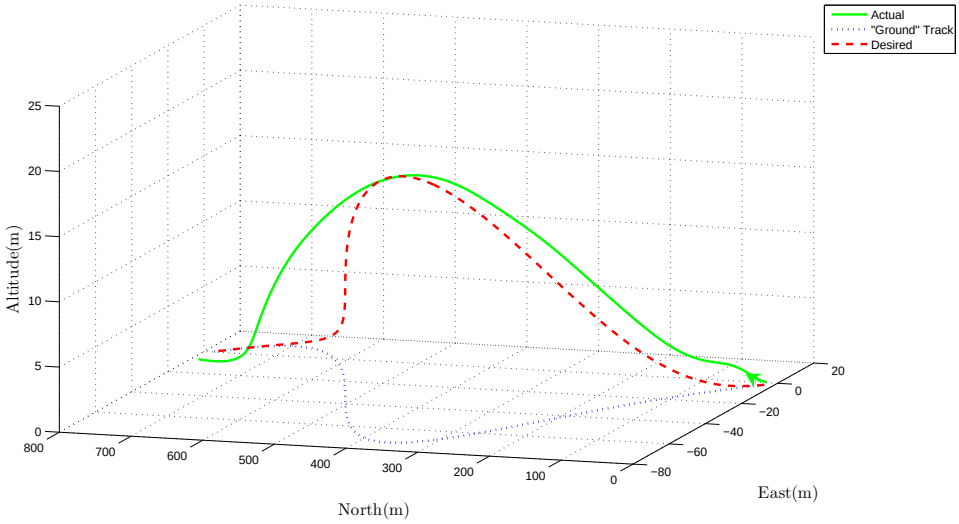

Figure 6.30: Travelling trajectory tracking in 6DoF model

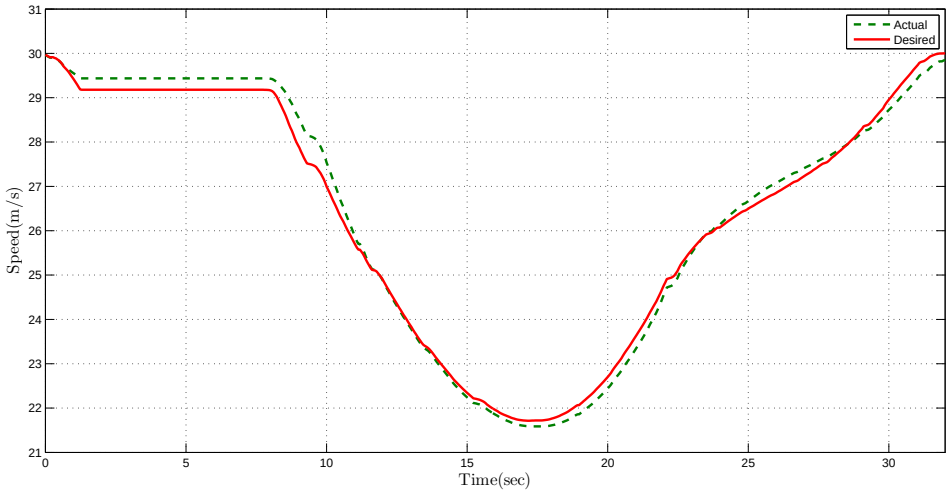

Figure 6.31: Travelling mode speed 6DoF model

Figure D.7 shows the trajectory for the loitering mode, where the desired trajectory obtained for the point mass model is plotted with the trajectory obtained from the 6DoF simulation. Figure D.8, shows the speed values predicted by the point mass model and the actual values obtained from the 6DoF simulation.

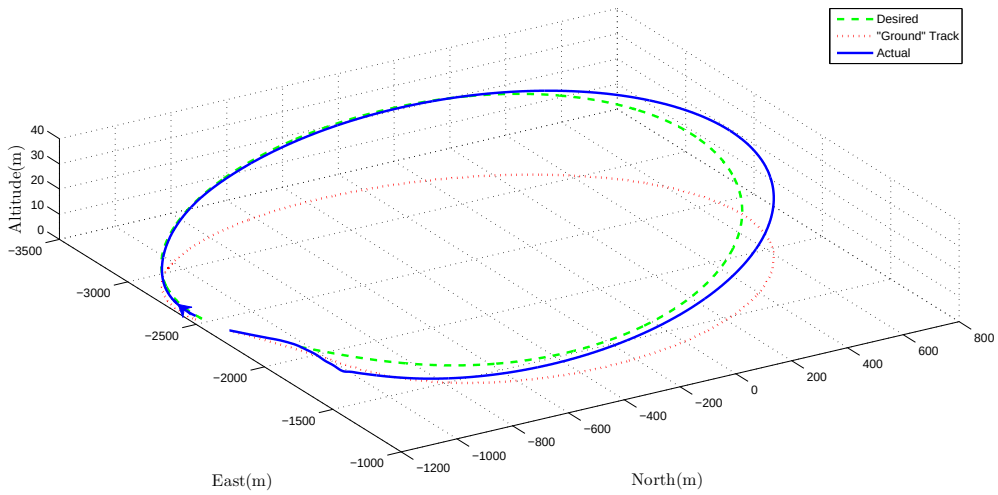

Figure 6.32: Loitering trajectory tracking in 6DoF model

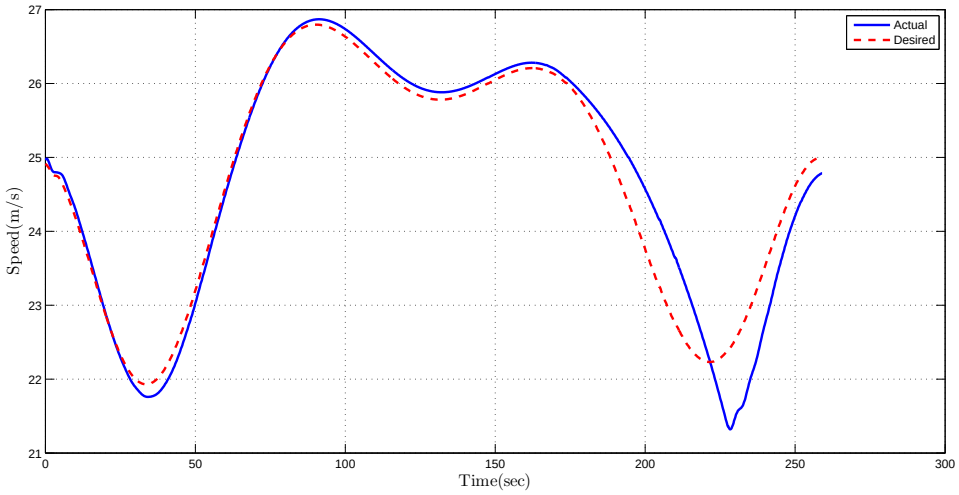

Figure 6.33: Loitering mode speed 6DoF model

The crosswind mode 6 DoF simulations demonstrated a thrust saving of 3.5% to 12% as compared with a predicted saving of 3.5% by the point mass model. The loitering mode demonstrated a saving of 3.3% and the point mass trajectory used predicted a saving of 6%.

The trajectory of crosswind that resulted in 3.5% savings was also followed various times in the 6DoF model and resulted in fuel savings of 5% to 11%. The fuel savings are very sensitive to the along-track and cross-track controllers gains and for example when a fuel saving of 12% was achieved in the 6DoF for the cross wind mode for particular controller gain values the corresponding saving was 11% when no wind shear was used see Figure 6.34 to 6.35. The modelling inaccuracy and tracking error both contribute to the discrepancies. The solution is sensitive because the fuel savings are small and are of similar order to the modelling and tracking errors. The plots for the case when 12% fuel savings were realized for crosswind trajectory are shown in Figures 6.36 to 6.37. In Appendix D the 6DoF trajectory and speed tracking are presented for a more gentle loitering manouver with a cycle time of 460 seconds and the resulting tracking error are very small.

Model	Crosswind(%)	No Wind shear savings(%)	Loitering savings(%)
Point Mass	3.5	–	6
6DoF	3.5 to 12	5 to 11	3.3

Table 6.6: Fuel saving comparison

6.6 Conclusions

6.6.1 Thermal Soaring

1. The thermal positioning capability was demonstrated using eight different sizes of thermals using Carmichael models. The positioning algorithm did not require individual tuning for these different thermal sizes. It was also tested using three different sizes of Woodward's model.

2. The edge cutting and passing through variable updraft strength resulted in small oscillations in the altitude gained and this resulted in suboptimal performance.

3. The use of the positioning algorithm that included a turning logic resulted in improved performance.

6.6.2 Dynamic Soaring in Wind Shear

1. The results of the crosswind travelling mode predicted a total power saving per horizontal distance travelled of 3.5%. The trajectories generated for the travelling problem are successfully followed in the 6DoF powered sailplane model simulation and they validate the point mass model results, by demonstrating 3% to 12% savings in the energy used

per length of the horizontal distance travelled. The more aggressive trajectories for the crosswind mode resulted in the savings of up to 8.5%.

2. In the case of the loitering mode, a 6% total power saving per total time in air is predicted compared with the powered sailplane executing the loop without utilizing the wind shear. The saving is achieved as a result of lower thrust usage and lower airspeed. These results are also validated in 6DoF simulations and resulted in 3.3% saving.

3. The modelling and tracking errors both contribute to the discrepancies in the point mass and 6DoF model results and the small fuel savings make the solution sensitive.

4. An additional outcome of the research was fuel saving due to the contribution of sinusoidal cruise in crosswind travelling mode.

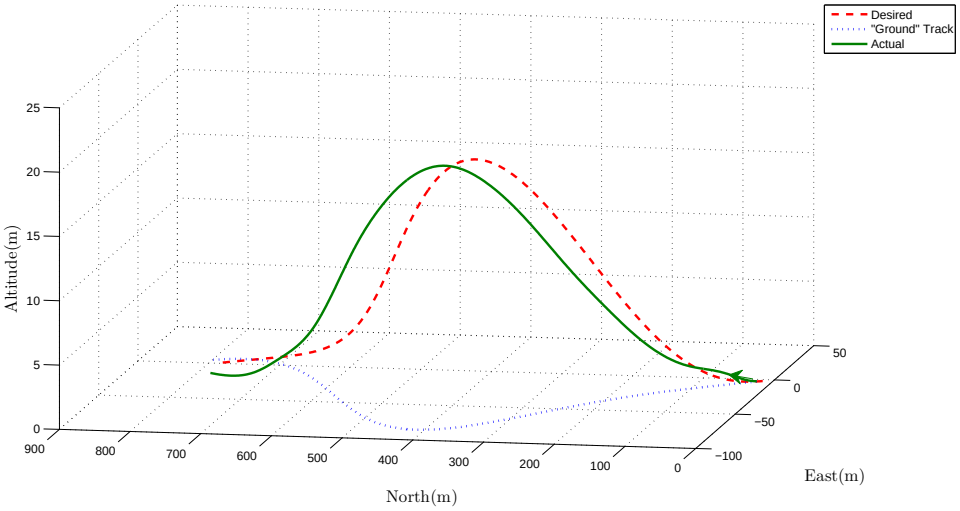

Figure 6.34: No Wind Shear mode trajectory tracking in 6DoF model

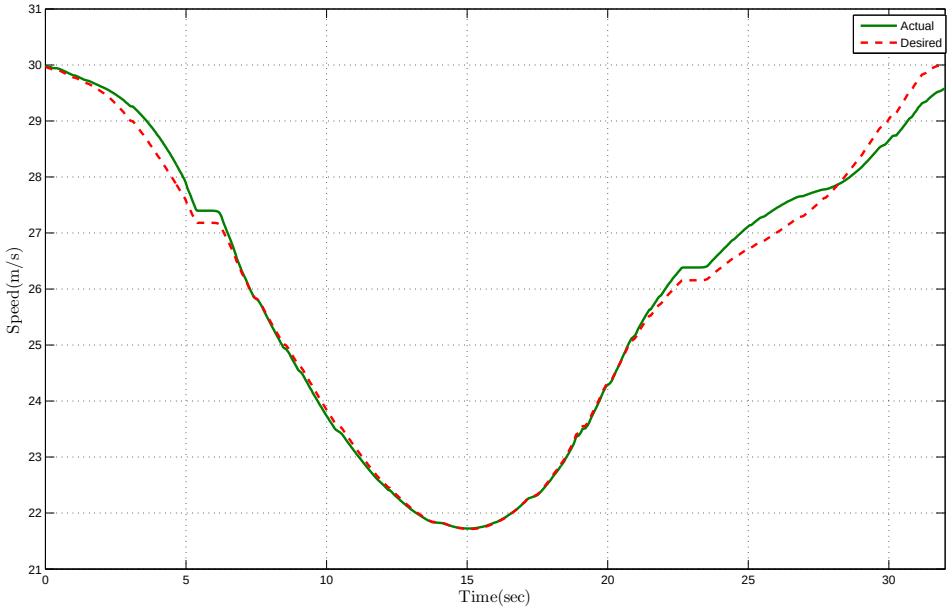

Figure 6.35: No Wind Shear mode speed 6DoF model

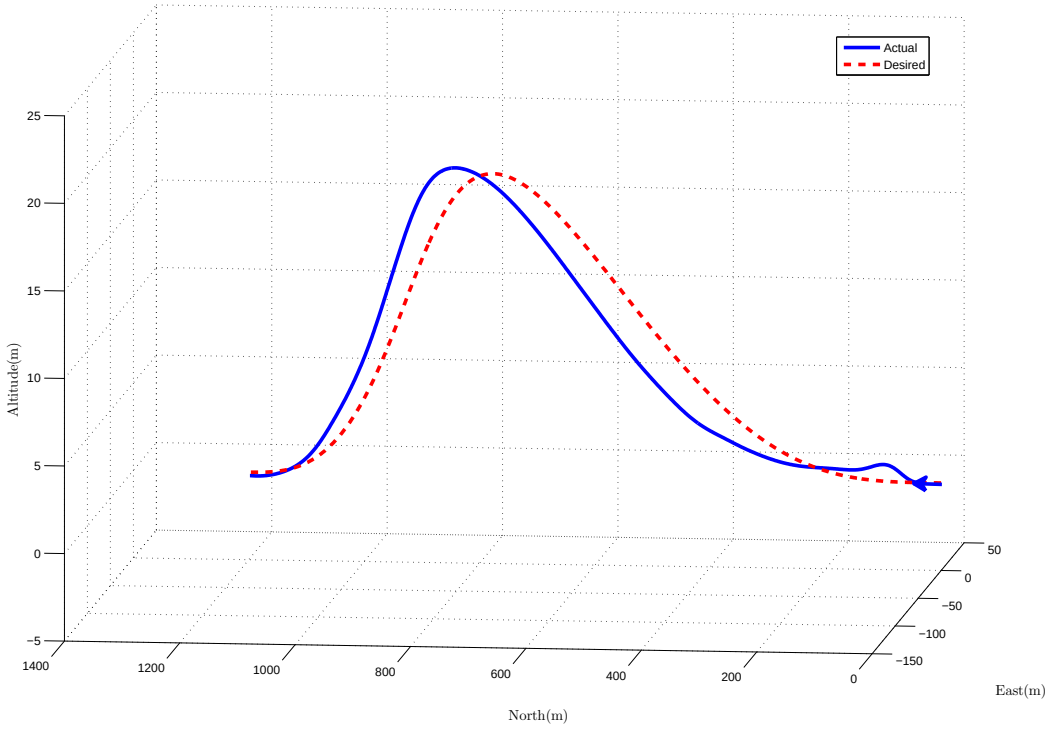

Figure 6.36: Travelling trajectory tracking in 6DoF model

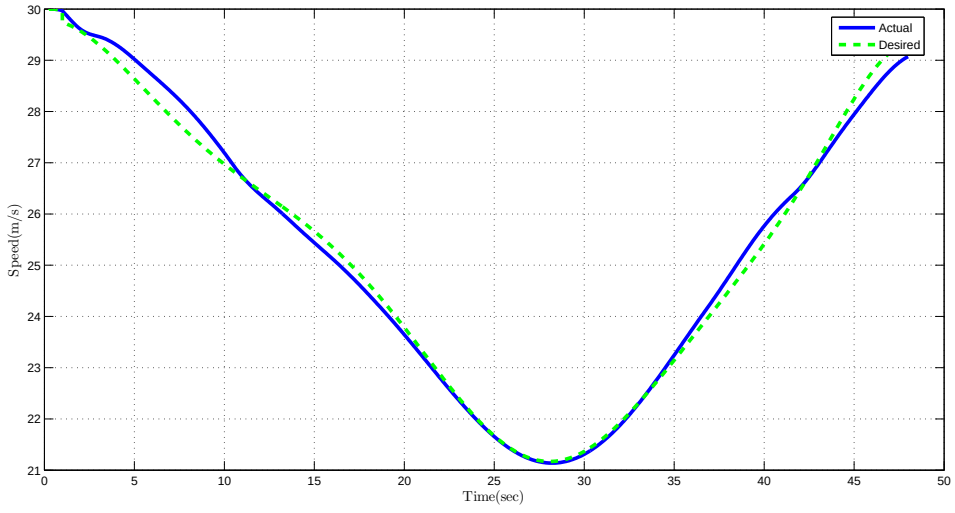

Figure 6.37: Travelling mode speed 6DoF model

Chapter 7

Conclusions and Future Work

This chapter concludes the research work and presents a summary of the main results. A number of recommendations have been made for the future work that would help to investigate the problem of soaring flight further.

7.1 Conclusions

Autonomous soaring is dependent on various key technologies and they all have to operate in an integrated system to make it work. The key is remote sensing of the thermal activity and then ability of a sailplane to position itself in a thermal autonomously to extract energy by gaining height. Dynamic soaring is dependent on the systems ability to estimate wind shear strength and wind direction and use this information to generate fuel saving trajectories. The trajectory following controller should be able to follow these trajectories. The results of the activities that involved testing these capabilities are described below.

7.1.1 Sensors and Image Recognition

The infra red camera trials successfully demonstrated the ability to see hot spots associated with the various landmarks and objects of interests.

7.1.2 Thermal Positioning Algorithm

1. The thermal positioning capability was demonstrated using eight different sizes of thermals using Carmichael models. The positioning algorithm did not require individual tuning for these different thermal sizes. It was also tested using three different sizes of Woodward's model.

2. The edge cutting and passing through variable updraft strength resulted in small oscillations in the altitude gained and this resulted in suboptimal performance.

3. The use of the positioning algorithm that included a turning logic resulted in improved performance.

7.1.3 Dynamic Soaring in Wind Shear

1. The IDVD method has a clear benefit because it can be implemented in real-time as the optimization time is just eight seconds compared to a trajectory loop time between 20 and 1000 seconds depending on the cost function. This short optimization time would allow computation of the next loop during the current trajectory loop. The estimation of the shear characteristics for the previous loop are used.

2. Wind shear estimation was carried out using least squares method for each dynamic soaring cycle so that these results could be used for the next dynamic soaring trajectory calculation.

3. The results of the crosswind travelling mode demonstrated a total power saving per horizontal distance travelled of 3.5% for the chosen example. The trajectories generated for the travelling problem are successfully followed in the 6DoF powered sailplane model simulation and they validate the point mass model results, by demonstrating 3% to 12% savings in the energy used per length of the horizontal distance travelled. The more aggressive trajectories for the crosswind mode resulted in the savings of up to 8.5%.

4. In the case of the loitering mode, a 6% total power saving per total time in air is achieved compared with the powered sailplane executing the loop without utilizing the wind shear. The saving is achieved as a result of lower thrust usage and lower airspeed. These results are also validated in 6DoF simulations and resulted in 3.3% saving.

5. The modelling and tracking errors both contribute to the discrepancies in the point mass and 6DoF model results and the small fuel savings make the solution sensitive.

6. The solutions for crosswind travelling are close to a straight line and the time to complete a cycle is not very different from that for straight line motion. Therefore fuel saving is achieved without compromising the time to complete a cycle.

7. An additional outcome of the research was fuel saving due to the contribution of sinusoidal cruise in crosswind travelling mode.

8. The main disadvantages of the IDVD method are that sub-optimal solutions are generally obtained, and that there is no guarantee that feasible solutions are obtained. In such cases, the last obtained feasible trajectory can be used for the next loop and repeated until a feasible solutions is obtained.

7.2 Future work

The following recommendations are made for future work:

1. It is recommended that an on-board image processing system should be used to look ahead and identify clouds and even soaring birds. This will help identify landmarks

and objects many miles ahead of the sailplane. A database linked to the meteorological information source should be used to provide a grid with estimates of updrafts at various locations.

2. In the current research, Woodwards absolute updraft velocity distribution with thermal sizes described by Carmichael are used and they are based on the assumptions that a thermal is circular and updraft distribution is Gaussian. The positioning algorithm should also be tested on more sophisticated thermals.

3. Testing should be carried out of using an algorithm that can estimate a thermal center, as this will allow a UAV to circle around the center, as this will not involve crossing the regions of varying updraft strength. This will avoid small oscillations experienced in the bank tracking and altitude tracking and would lead to optimum performance.

4. Lags were observed while following the more aggressive manoeuvre in 6DoF simulations. A further improvement in trajectory following controller is required specially for aggressive manoeuvre.

5. A practical test for the dynamic soaring in wind shear for large UAVs would quantify the fuel savings in the real life.

6. A practical demonstration could involve using a model aeroplane and installing image recognition and soaring controller on-board. This would allow the testing of how much endurance is increased.

7. The sinusoidal cruise control should be tested using 6DoF models of a fighter aircraft and also of an airliner to quantify the fuel savings.

Bibliography

[AK09] K. Andersson and I. Kaminer. On stability of hermal centering controller. In *AIAA Guidance, Navigation and Control Conference*, Chicago,Illinois, August 2009.

[All06] M.J. Allen. Updraft model for development of autonomous soaring uninhabited air vehicles. In *44 th AIAA Aerospace Sciences Meeting and Exhibit*, number AIAA 2006-1510, Reno, Nevada, 9-12 January 2006.

[Amr05] A.R. Amrane. Flight dynamics model of a high performance sailplane. Master's thesis, School of Engineering, Cranfield University, September 2005.

[Bos02] M.B.E. Boslough. Autonomous dynamic soaring platform for distributed mobile sensor arrays. Technical report, Sandia National Laboratories, June 2002.

[Car54] B.H. Carmichael. What price performance. *Soaring*, 18, May/June 1954.

[CCW06] M.V. Cook, A.K. Cooke, and J.F. Whidborne. Flight dynamics modelling refinement for an autonomous UAV glider. College of Aeronautics Report NFP0505, School of Engineering, Cranfield University, Feburary 2006.

[Con61] C.D. Cone. The theory of soaring flight in vortex shells-1. *Soaring Magazine*, April 1961.

[Con64] C.D. Cone. The design of sailplanes for optimum thermal soaring performance. Technical Report TND 2052, NASA, 1964.

[CRW+08] I.D. Cowling, M. Roberts, S. Willcox, Y. Patel, and P. Smith. Increasing persistence of UAVs and MAVs through thermal soaring. In *23st Bristol Conference on UAVs*, Bristol, U.K., April 2008.

[CYW07] I.D. Cowling, O.A. Yakimenko, and J.F. Whidborne. A prototype of an autonomous controller for a quadrotor UAV. In *Proceedings European Control Conference*, Kos, Greece, July 2007.

[DABL08] A . Dennis, J. Archibald, Edwards B., and D.J. Lee. On-board vision based sense-avoid for small uavs. In *AIAA Guidance, Control Conference and Exhibit*, Honolulu, Hawaii, August 2008.

[DRTP09a] M. Deittert, A. Richards, C.A. Toomer, and A. Pipe. Dynamic soaring flight in turbulence. In *AIAA Guidance, Navigation and Control Conference*, Chicago, Illinois, August 2009.

[DRTP09b] M. Deittert, A. Richards, C.A. Toomer, and A. Pipe. Engineless unmanned aerial vehicle propulsion by dynamic soaring. *Journal of Guidance, Control and Dynamics*, 32(6), November 2009.

[DTP06] M. Deittert, C. Toomer, and A.G. Pipe. Biologically inspired uav propulsion. In *21 st UAV Bristol Conference on UAVs*, Bristol, U.K., April 2006.

[Edw08] D.J. Edwards. Implementation details and flight test results of an autonomous soaring controller. In *AIAA Guidance, Navigation and Control Conference and Exhibit*, Honolulu, Hawaii, August 2008.

[GEC06] A.K. Goodwin, G.K . Egan, and F. Crusca. UAV ridge saoring in an unknown environment. Technical report, Manash University, 2006.

[HFPW07] M.K. Hook, D.A. Findlay, A.G. Purcell, and R.T. Watkin. Autonomous soaring. Technical report, Roke Manor Research Limited, 2007.

[Hor76] K.H. Horstmannm. Neue modellaufwindverteilungen and ihr einflub auf die aiuslegung von segelflugzeugen. In *OSTIV Publication XIV. Presented at the XV OSTIV Congress*, Rayskala, Finland, 1976.

[IIB+07] R. Irvine, F. Innes, A. Brown, S. Vosper, G. Rooney, B. Devenish, M. Hook, and E. Sparks. Autonomous soaring project phase 2. In *2 nd SEAS DTC Technical Conference*, Edinburgh, U.K., 2007.

[Jac05] M. Jacobson. *Fundamentals of Atmospheric Modelling*. Cambridge University Press, 2 nd edition, 2005.

[KB95] K. J. Astrom K.J. and Wittenmark B. *Adaptive Control*. Addison-Wesley, Reading, MA, 1995.

[Kic01] T. Kiceniuk. Dynamic soaring and sailplane energetics. *Technical Soaring*, XXV(4), August 2001.

[Koc05] G.J. Koch. Doppler lidar obervations of an atmospheric thermal providing lift to soaring ospreys. Technical report, NASA Langley Research Center, 2005.

[Lan09] J.W. Langelaan. Gust energy extraction for mini and micro uninhabited aerial vehicles. *Journal of Guidance, Control and Dynamics*, 32, No2, March -April 2009.

[Mos99] G.E. Moster. Oscillatory trajectories applied to NASA's DF-7 configuration. In *AIAA 9th International Space Planes and Hypersonic Systems and Technologies Conference*, Norfolk, Virginia, November 1999.

[PDH04] S. Park, J. Deyst, and J.P. How. A non-linear guidance logic for trajectory tracking. In *AIAA Guidance, Navigation and Control Conference and Exhibit*, Rhode Island, August 2004.

[Pig90] D. Piggott. *Gliding: A handbook on Soaring Flight.* A&C Black, London, 6th edition, 1990.

[Pig95] D. Piggott. *Beginning Gliding.* A&C Black, London, 1995.

[PK97] H. Pruppacher and J. Klett. *Microphysics of Clouds and Precipitation.* Kluwer Academic Publishers, 1997.

[QZ05] Y.C. Qi and Y.J. Zhao. Energy efficient trajectories of unmanned aerial vehicles flying through thermals. *Journal of Aerospace Engineering*, April 2005.

[Ray83] Lord Rayleigh. Letter to nature. XX111:Page 10, 1883.

[SC03] G. Sachs and O. da Costa. Optimization of dynamic soaring at ridges. In *Atmospheric Flight Mechanics Conference and Exhibit*, Austin, Texas, August 2003.

[SLKK08] S. Sohn, B. Lee, J. Kim, and C. Kee. Vision-based real-time target localization for single-antenna gps-guided UAV. *IEEE Transactions on Aerospace and Electronics Systems*, 44(4), October 2008.

[Tho99] F. Thomas. *Fundamentals of Sailplane Design.* College Park Press, 3 rd (english) edition, 1999.

[Wal77] C.E. Wallington. *Meteorology for glider pilots.* John Murray Publisher, 1977.

[WCY08] J.F. Whidborne, I.D. Cowling, and O.A. Yakimenko. Direct method for UAV guidance and control. In *23 rd Bristol Conference on UAVs*, Bristol, U.K., April 2008.

[Wha98] J. Wharington. *Autonomous Control of Saoring Aircraft by Reinforcement Learning.* PhD thesis, Royal Melbourne Institute of Technology, November 1998.

[Wha04] J.M. Wharington. Heuristic control of dynamic soaring. In *5 th Asian Control Conference*, Melbourne, Australia, July 2004.

[Woo58] B. Woodward. The motion in and around isolated thermals. In *7 th, OSTIV Congress*, Lezno, Poland, June 1958.

[Yak00] O.A. Yakimenko. Direct method for rapid prototyping of near-optimal aircraft trajectories. *AIAA Journal of Guidance Control and Dynamics*, (23(5):865-875), 2000.

[Zha04a] Y.J. Zhao. Minimum fuel powered dynamic soaring of unmanned aerial vehicles utilizing wind gradients. *Optimal Control Applications and Methods*, (25:211-233), 2004.

[Zha04b] Y.J. Zhao. Optimal dynamic soaring. *Optimal Control Applications and Methods*, (25:67-89), 2004.

Appendix A

Equations for the Non-linear Model

A.1 Longitudinal Aerodynamic Forces and Moments

This section is based on the work of Amrane [Amr05] and the coefficients of the equations are described in Table A.1. The total lift of the sailplane is defined as a sum of the wing lift and tailplane lift as follows:

$$L = L_W + L_T \tag{A.1}$$

The wing lift is calculated using a two dimensional strip theory and the tailplane lift is calculated using the classical method applied on the horizontal tail by considering it as a straight-tapered platform [Amr05].

A.1.1 Wing Lift

The general expression for the lift coefficient of any airfoil along the span, is given by:

$$[C_L(y)]_W = [a_1(y)]_W(\alpha_e(y) - \alpha_{0i}) + \Delta C_{L0t}(y) + \Delta C_{L0a}(y) \tag{A.2}$$

$a_1(y)$ is the two dimensional lift curve slope in viscous and incompressible flow. α_{0i} is the incompressible zero lift incidence for the airfoil, where ΔC_{Lot} is the increment in lift at zero angle of attack due to plain trailing edge flap and ΔC_{L0a} is an increment due to an aileron. The wing geometry is defined in Figure 6.1, the chord along the span is defined as:

- For $y \in [-5.82; -0.24] \cup [0.24; 5.82]$ we have $c(y) = -0.0287y + 0.847$
- For $y \in [-9; -5.82] \cup [5.829; 9]$ we have $c(y) = -0.11y + 1.32$
- For $y \in [-0.24; 0.24]$, we have $c(y) = 0$

The maximum lift coefficient for any two dimensional wing section along the span is:

$$[C_{L_m}(y)]_W = C_{L0}(y) + \Delta C_{Lm}(y) + \Delta C_{Lma}(y) \tag{A.3}$$

ΔC_{Lm} is an increment in maximum lift coefficient and ΔC_{Lmt} is increment in a plain trailing edge deployed, where as ΔC_{Loa} is due to an aileron deflection.

The local wing lift is calculated by calling y_l, the middle position of the segment with length d_y such that:

$$y_l = y + \frac{dy}{2} \tag{A.4}$$

The local lift, $L_W(y_l)$ can be calculated as:

$$L_W^w(y_l) = \frac{1}{2}\rho(V)_e(y_l)^2 \left[C_L(y_l)\right]_W c(y_l)dy \tag{A.5}$$

The total lift of the wing L_W is given by integration of the values along the span of the wing as follows:

$$L_W^w = \sum_{yl=-9...9} [L_W^w(y_l)] \tag{A.6}$$

The total tailplane lift L_T is the sum of two components which are the lift, L_{T1} due to the angle of attack and L_{T2} which is due to pitch rate q.

$$L_T = L_{T1} + L_{T2} \tag{A.7}$$

The tailplane aerofoil section is a symmetric Wortmann Fx-71-L-150 aerofoil, the resultant lift coefficient due to the horizontal-tail area reduces to $(a_1)_T$ is the tailplane lift curve slope. The lift curve slope with aileron deflection is a_2.

$$(C_L)_T = (a_1)_T\alpha_{eT} + (a_2)_T\delta_E \tag{A.8}$$

The lift force of the tailplane due to the angle of attack is given by:

$$L_{T1} = \frac{1}{2}\rho V_o^2 S_T (C_L)_T \tag{A.9}$$

The maximum tailplane lift coefficient's expression is

$$(C_{Lm})_T = (\Delta C_{Lm})_T + \Delta C_{LmE} \tag{A.10}$$

ΔC_{Lm} is an increment in the maximum lift coefficient and ΔC_{LmE} is due to the elevator deflection. The tailplane lift L_{T2} due to rate of pitch is defined as:

$$L_{T2} = \frac{1}{2}\rho V_o^2 S_W (Z_q)_T \frac{q\bar{\bar{c}}_W}{V_o} \tag{A.11}$$

where $(Z_q)_T$ is the tailplane lift force derivative. The total drag of the sailplane consists of the contributions from the wing D_W, the tailplane D_T and fin D_F and the fuselage D_B, such that:

$$D = D_W + D_T + D_F + D_B \tag{A.12}$$

The general drag expression of any section along any aerofoil section is given by:

$$[C_D(y)]_W = C_{Do}(y) + \Delta C_{Dot}(y) + \Delta_{Doa}(y) + C_{Di}\,[C_L(y)]_w \tag{A.13}$$

ΔC_{Dot} is an increment in the profile drag due to trailing edge deflection and ΔC_{Doa} is due to aileron deflection, where $C_{Di}(y)$ is induced drag coefficient. The middle position of the segment with the length d_y is called y_l such that: $y_l{=}y + \frac{d_y}{2}$.

The local drag in local wind axis D_W^w, can be calculated at each local aerodynamic center as follows:

$$D_W^w(y_l) = \frac{1}{2}\rho V_e(y_l)^2\,[C_D(y_l)]_W\,c(y_l)dy \tag{A.14}$$

The total drag of the wing, D_W is calculated by integrating along the span of the wing

$$D_W^w = \sum_{yl=-9\ldots9} [D_W^w(y_l)] \tag{A.15}$$

Both horizontal and vertical stabilizers are composed of the same symmetrical Wortmann FX-71-L-150 aerofoil, and the linear relationship between C_D and C_L^2, and is defined as:

$$C_D = C_{Do} + KC_L^2 \tag{A.16}$$

For the tailplane this expression becomes:

$$(C_D)_T = (C_{Do})_S + \Delta C_{D0_E} + K_T(C_L)_T^2 \tag{A.17}$$

$(C_{Do})_s$ is the stabilizer drag profile, C_{DoE} is an increment in the profile drag due to an elevator and ΔC_{DoR} is increment due to the rudder deflection. The drag coefficient for the fin is described as:

$$(C_D)_F = (C_{Do})_S + \Delta C_{D0_E} + K_F(C_L)_{F^2} \tag{A.18}$$

The drag generated by the tailplane is given by:

$$D_T = \frac{1}{2}\rho V_o^2 S_T(C_D)_T \tag{A.19}$$

The drag generated by the fin is given by:

$$D_F = \frac{1}{2}\rho V_o^2 S_F(C_D)_F \tag{A.20}$$

The equivalent body surface S_B is defined as:

$$S_B = C_s \pi D l_B \tag{A.21}$$

C_s is body surface coefficient and $(C_D)_B$ is body profile drag coefficient. The drag generated by the tailplane is given by:

$$D_B = \frac{1}{2}\rho V_0^2 S_B(C_D)_B \tag{A.22}$$

The total pitching moment of the sailplane consists of the moment generated by tailplane, M_T and the wings, M_W such that

$$M = M_W + M_T \tag{A.23}$$

At the center of gravity of the aircraft, the pitching moment is composed of the surface pitching moment and the the component of due to lift or drag produced by the surface multiplied by its moment arm.

The general expression for two-dimensional wing pitching moment coefficient defined at the aerodynamic center of the aerofoil is given by:

$$[C_m(y)]_W = [C_{mo}(y)]_W + \Delta C_{mot}(y) - [h_o(y) + \Delta h_1(y)]_W [a_1(y)]_W \, \alpha_e(y) \tag{A.24}$$

C_{mo} is the incompressible pitching moment coefficient at zero angle of attack due to the basic wing section and ΔC_{mot} is the pitching moment coefficient moment due to a plain trailing edge flap. Δh_1 is an increment in the center of the lift due to the flap deflection and $[a_1(y)]_w$ is a two dimensional lift curve slope in viscous and incompressible flow. The middle position of the segment with a length d_y can be called y_l such that $y_l = y + \frac{d_y}{2}$

$$M_W(y_l) = \frac{1}{2}\rho V_e(y_l)^2 \, [C_m(y_l)]_W \, c^2(y_l) dy + L_W(y_l) \left[X_{CG} - \frac{x_{ai}}{c(y_l)} \right] cos(\alpha_e(y)) \tag{A.25}$$

$\frac{x_{ai}}{c}$ is the aerodynamic center for airfoil. The total pitching moment of the wing, M_W is obtained by integrating the values along the span of the wing and is given by:

$$M_W = \sum_{yl=-9\ldots9} [M_W(y_l)] \tag{A.26}$$

The tailplane is a significant contributor to the total pitching moment of the sailplane and consists of two components, first one due to angle of attack, M_{T1} and the second due to the rate of pitch, M_{T2}. The total tailplane of the pitching moments then is given by:

$$M_T = M_{T1} + M_{T2} \tag{A.27}$$

The pitching moment coefficient of the tailplane defined at the aerodynamic center of the sailplane, $(C_m)_T$ is given by:

$$(C_m)_T = (C_{mo})_T + (\mu_O)_T \delta_E - [h_o + \Delta h_1]_T a_{1T} \alpha_T \tag{A.28}$$

C_{m0} is the incompressible pitching moment at zero angle of attack for the basic wing section. $(\mu_0)_T$ is the rate of change pitching moment with a rudder deflection at constant lift. a_{1T} is a lift curve slope. The total pitching moment due to angle of attack, M_{T1} can be described by the following expression:

$$M_{T1} = \frac{1}{2}\rho V_o^2 S_T \overline{\overline{c_T}} (C_m)_T + L_{T1}[X_{CG} - \frac{x_{acT}}{\overline{\overline{c_T}}} \overline{\overline{c_T}}] + D_T z_{acT} \tag{A.29}$$

where Z_{acT} is the location of the tailplane on the Z body and $\frac{x_{acT}}{\overline{\overline{c_T}}}$ is the aerodynamic center position. The tailplane pitching moment due to rate of pitch M_{T2} is defined as:

$$M_{T2} = \left[\frac{1}{2}\rho V_o^2 S_W \overline{\overline{c_W}}\right][(M_q)_T \frac{q\overline{\overline{c_W}}}{V_o}\Bigg] \tag{A.30}$$

$(M_q)_T$ is the tailplane pitching moment derivative and $(M_q)_B$ is the body pitching moment. The contribution of the body to the pitching moment derivative due to the rate of pitch for the complete aircraft, M_B is taken into account and is defined as:

$$M_B = \left[\frac{1}{2}\rho V_o^2 S_W \overline{\overline{c_W}}\right]\left[(M_q)_B \frac{q\overline{\overline{c_W}}}{V_o}\right] \tag{A.31}$$

As the local wind axis are not the same along the span of the wing, therefore to determine the total lift and drag, they have been transformed to the body axis using the cosine matrix, $D^{bw}(y)$ and the local body axis forces defined at each local aerodynamic center are defined as:

$$\left[X_W^b(y), Y_W^b(y), Z_W^2(y)\right] = \left[D^{bw}(y)\right][-D_W^w(y), 0, -L_W^w(y)] \tag{A.32}$$

The total axial force component is defined as:

$$X_W^b = \sum_{y=-9\ldots9}\left[X_W^b(y)\right] \tag{A.33}$$

The total lateral force is defined as:

$$Y_W^b = \sum_{y=-9\ldots9}\left[Y_W^b(y)\right] \tag{A.34}$$

The total normal component is similarly defined as:

$$Z_W^b = \sum_{y=-9\ldots9}\left[Z_W^b(y)\right] \tag{A.35}$$

A.2 Lateral-Directional Aerodynamic Forces and Moments

The side force of the sailplane consists of the contribution from the fin, the wing and the influence of the body due to rate of yaw. The total side force is given by:

$$Y = Y_F + Y_W + Y_B \tag{A.36}$$

The total side force for the fin takes into account the effect of side slip velocity v, rate of roll p, rate of yaw r and rudder deflection ζ, such that:

$$Y_F = \left[\frac{1}{2}\rho V_o^2 S_W\right]\left[(Y_v)_F \frac{v}{V_o} + (Y_p)_F \frac{pb_W}{V_o} + (Y_r)_F \frac{pb_W}{V_0} + (Y_\zeta)\right] \tag{A.37}$$

The total contribution of the wing side force has already been determined and defined as:

$$Y_W = Y_W^b \tag{A.38}$$

The contribution of the body to the total side force composed of the lateral force due to rate of yaw and is defined as:

$$Y_B = \left[\frac{1}{2}\rho V_o^2 S_W\right]\left[(Y_r)_B \frac{pb_W}{V_0}\right] \tag{A.39}$$

The total rolling moment of the sailplane LL_W is consists of the wing, fin and the contribution from the tailplane and is summed as:

$$LL = LL_W + LL_F + LL_T \tag{A.40}$$

Due to the presence of the thermals or deflection of ailerons, the normal force distribution is no longer symmetric, and the total contribution of the wing to the rolling moment is defined as:

$$LL_W = \sum_{y=0\ldots9}\left[yZ_W^b(y)\right] - \sum_{y=-9\ldots0}\left[yZ_W^b(y)\right] \tag{A.41}$$

The contribution of the tailplane to the total rolling moment only consists of contribution due to the rate of roll such that

$$LL_T = \left[\frac{1}{2}\rho V_0^2 S_W b_W\right]\left[(L_p)_T \frac{pb_W}{V_o}\right] \tag{A.42}$$

The total yawing moment of the sailplane, N is composed of contributions from the fin, wing and body and is given by

$$N = N_F + N_W + N_B \tag{A.43}$$

The total yawing moment is composed of the effects of side slip velocity, v, rate of roll, p, rate of yaw, r and rudder deflection ζ such that

$$N_F = \left[\frac{1}{2}\rho V_o^2 S_W b_W\right]\left[(N_v)_F \frac{v}{V_o} + (N_p)_F \frac{pb_W}{V_o} + (N_r)_F \frac{pb_W}{V_o} + (N_\zeta)_F \zeta\right] \tag{A.44}$$

The wing's contribution to the total yawing moment is defined as

$$N_W = \sum_{y=-9\ldots0}\left[yX_W^b(y)\right] - \sum_{y=0\ldots9}\left[yX_W^b(y)\right] \tag{A.45}$$

The contribution of the body to the total yawing moment is based on the lateral force due to rate of yaw such that

$$N_B = \left[\frac{1}{2}\rho V_o^2 s_W b_W\right]\left[(N_r)_B \frac{pb_W}{V_o}\right] \tag{A.46}$$

Coefficient	Value	Reference
$(a_1)_W$	$0.1052/deg$	ESDU 97020
α_i	$-4.649deg$	ESDU 72024
ΔC_{Lot}	0.658	ESDU 94028
$\frac{x_{ai}}{c}$	0.274	ESDU 72024
ΔC_{Lmt}	0.343	ESDU 94028
ΔC_{Lm}	0.74	ESDU84026
$(a_1)_T$	$4.756/rad$	ESDU70011
$(a_2)_T$	$3.07/rad$	ESDU AERO c.01.01.03
$(Z_q)_T$	$-2.68/rad$	ESDU90010
CDo	40.00717	ESDU 00027
ΔC_{Dot}	0.024	ESDU 87005
C_{Lo}	0.489	ESDU 84026
C_{Lm}	1.22	ESDU 84026
$(C_{Lm})_T$	1.12	ESDU 84026
a_{1F}	$3.41/rad$	ESDU 70011
$(C_{Lmax})_T$	1.02	ESDU 89034
$(a_2)_F$	$3.36/rad$	ESDU AERO c.01.01.03
μ_T	0.58	ESDU AERO C.08.01.01
$(M_q)_T$	$-0.204/rad$	ESDU 90010
$(Z_q)_T$	$-2.68/rad$	ESDU 90010
$(Z_q)_W$	$1.594/rad$	ESDU 90010
$(Y_v)_F$	$-0.229/rad$	ESDU 90010
$(N_v)_F(\alpha = 8deg)$	$0.0565/rad$	ESDU 90010
$(L_v)_F(\alpha = 8deg)$	$-0.00268/rad$	ESDU90010
$(Y_r)_F$	$0.0688/rad$	ESDU 82017
$(N_r)_F$	$-0.0688/rad$	ESDU 82017
$(L_r)_F$	$0.000804/rad$	ESDU 82017
$(L_p)_{Tail}$	$0.208/rad$	ESDU Aero A.06.01.01
$z * F$	$0.738m$	ESDU 83006
$l * F$	$4.42m$	ESDU 83006
$(Y_p)_F$	0.0574	ESDU 83006
$(N_p)_F$	$-0.0135/rad$	ESDU 83006
$(L_p)_F$	0.00407	ESDU 83006
$(L_p)_T$	$0.000221/rad$	ESDU 83006
J_R	0.709	ESDU 87008
$(Y_\zeta)_F$	$0.148/rad$	ESDU 87008
$(N_\zeta)_F$	$-0.0103/rad$	ESDU 87008
$(L_\zeta)_F$	$0.000235/rad$	ESDU 87008
C_{Sf}	0.79	ESDU 77028
C_{vf}	0.675	ESDU 77028
C_{Sa}	0.68	ESDU 77028
C_{Va}	0.48	ESDU 77028
C_S	0.910	ESDU 77028
S	$15m^2$	ESDU 77028
C_v	0.762	ESDU 77028
C_F	0.00435	ESDU ESDU 78019
$(C_D)_B$	0.00463	ESDU 78019

Table A.1: Coefficients used in Equations

Appendix B

Differentially Flat Equations

In this appendix proof of the differential flat equations is described.

$$\bar{V} = \frac{G}{g}V, \qquad \left(\bar{x}, \bar{y}, \bar{h}\right) = \frac{G^2}{g}(x, y, h), \tag{B.1}$$

$$\bar{T} = \frac{T}{mg}, \qquad \sigma = Gt, \tag{B.2}$$

and we have

$$\dot{(\cdot)} = \frac{d(\cdot)}{d\sigma} = \frac{1}{G}\frac{d(\cdot)}{dt}. \tag{B.3}$$

The normalized equations of motion, after some derivation, become:

$$\dot{\bar{V}} = \bar{T} - \bar{\rho}\bar{V}^2 C_D - \sin\gamma - (A + 2B\bar{h})\bar{V}\sin\gamma\cos\gamma\sin\psi, \tag{B.4}$$

$$\dot{\psi} = \frac{\bar{\rho}\bar{V}C_L\sin\phi}{\cos\gamma} - (A + 2B\bar{h})\tan\gamma\cos\psi, \tag{B.5}$$

$$\dot{\gamma} = \bar{\rho}\bar{V}C_L\cos\phi - \frac{\cos\gamma}{\bar{V}} + (A + 2B\bar{h})\sin^2\gamma\sin\psi, \tag{B.6}$$

$$\dot{\bar{h}} = \bar{V}\sin\gamma, \tag{B.7}$$

$$\dot{\bar{x}} = \bar{V}\cos\gamma\sin\psi + (A\bar{h} + B\bar{h}^2), \tag{B.8}$$

$$\dot{\bar{y}} = \bar{V}\cos\gamma\cos\psi. \tag{B.9}$$

where $\bar{\rho}$ is the wind shear parameter defined as:

$$\bar{\rho} = \frac{\rho g^2}{2(mg/S)G^2}. \tag{B.10}$$

$$\bar{W}_x = A + B\bar{h}^2. \tag{B.11}$$

The differentially flat form involves describing the states as a function of the output and its derivatives. We hence derive the above equations in this form as the following.

From equations (B.7), (B.8) and (B.9)

$$\bar{V} = \sqrt{(\dot{\bar{x}} - \bar{W}_x)^2 + \dot{\bar{y}}^2 + \dot{\bar{h}}^2}. \tag{B.12}$$

From equations B.8 and (B.9

$$\psi = \text{atan2}(\dot{\bar{y}}, (\dot{\bar{x}} - \dot{\bar{W}}_x)) \tag{B.13}$$

From equation (B.6)

$$\gamma = \arcsin \frac{\dot{\bar{h}}}{\bar{V}}, \tag{B.14}$$

Differentiating equation (B.14) gives

$$\begin{aligned}
\dot{\gamma} &= \frac{d}{dt} \arcsin \frac{\dot{h}}{V}, \\
&= \frac{1}{\sqrt{1 - \dot{\bar{h}}^2/\bar{V}^2}} \frac{\ddot{\bar{h}}\bar{V} - \dot{\bar{h}}\dot{\bar{V}}}{\bar{V}^2}, \\
&= \frac{\bar{V}}{\sqrt{\bar{V}^2 - \dot{\bar{h}}^2}} \frac{\ddot{\bar{h}}\bar{V} - \dot{\bar{h}}\dot{\bar{V}}}{\bar{V}^2}, \\
&= \frac{\ddot{\bar{h}}\bar{V} - \dot{\bar{h}}\dot{\bar{V}}}{\bar{V}\sqrt{\bar{V}^2 - \dot{\bar{h}}^2}}.
\end{aligned} \tag{B.15}$$

Substituting for $\bar{V}$ using equation (B.12) gives

$$\begin{aligned}
\dot{\gamma} &= \frac{\ddot{\bar{h}}\sqrt{\dot{\bar{x}}^2 + \dot{\bar{y}}^2 + \dot{\bar{h}}^2} - \dot{\bar{h}}2(\dot{\bar{x}} - \dot{\bar{W}}_x) \quad (\ddot{\bar{x}} - \dot{\bar{W}}_x) + 2\dot{\bar{y}}\ddot{\bar{y}} + 2\dot{\bar{h}}\ddot{\bar{h}}}{2\bar{V}\sqrt{\dot{\bar{x}} - \dot{\bar{W}}_x} + \dot{\bar{y}}} \\
&= \frac{\ddot{\bar{h}}}{\sqrt{(\dot{\bar{x}} - \dot{\bar{W}}_x)^2 + \dot{\bar{y}}^2}} - \frac{\dot{\bar{h}}(\dot{\bar{x}} - \dot{\bar{W}}_x)(\ddot{\bar{x}} - \dot{\bar{W}}_x) + \dot{\bar{y}}\ddot{\bar{y}} + \dot{\bar{h}}\ddot{\bar{h}}}{\sqrt{(\dot{\bar{x}} - \dot{\bar{W}}_x)^2 + \dot{\bar{y}}^2}\sqrt{(\dot{\bar{x}} - \dot{\bar{W}}_x)^2 + \dot{\bar{y}}^2 + \dot{\bar{h}}^2}}.
\end{aligned} \tag{B.16}$$

and similarly differentiation of equation B.13 results in:

$$\dot{\psi} = \frac{\dot{\bar{y}}(\ddot{\bar{x}} - \dot{\bar{W}}_x) - \dot{\bar{y}}(\ddot{\bar{x}} - \dot{\bar{W}}_x)}{(\dot{\bar{x}} - \dot{\bar{W}}_x)^2 + \dot{\bar{y}}^2} \tag{B.17}$$

Appendix C

Mathematical Model of Updraft Acceleration

The vertical acceleration, dw/dt, of a dry thermal was determined using standard air parcel theory as presented by Pruppacher [PK97] and Klett and by Jacobson [Jac05], and is described as following.

$$\frac{\mathrm{dw}}{\mathrm{dt}} = \frac{2}{3}\left[g\left[\frac{\Theta_v - \Theta_{v_\infty}}{\Theta_{v_\infty}}\right] - \mu_t\omega^2\right], \tag{C.1}$$

where Θ_V is the local or ambient (infinity) potential temperature.

$$\Theta_v = T_v\left[\frac{100000}{p}\right]^{0.286}, \tag{C.2}$$

$$T_v = T(1 + 0.608q_v), \tag{C.3}$$

and q_v equals zero for dry air. Entrainment of ambient air into a thermal parcel or bubble causes two effects. First it reduces the rate of ascent and second it modifies the rate of cooling of air within the bubble.

$$\frac{\mathrm{dw}}{\mathrm{dt}} = \frac{2}{3}\left[g\left[\frac{\Theta_v - \Theta_{v_\infty}}{\Theta_{v_\infty}}\right] - \mu_t\omega^2\right], \tag{C.4}$$

and lapse for the thermal becomes

$$\frac{\mathrm{dT_t}}{\mathrm{dz}} = \Gamma_t = -\frac{g}{C_{pdry}} - \mu_t(T - T_\infty), \tag{C.5}$$

$$\mu_t = \frac{3}{z}\left[1 - \frac{zg(C_p - R)}{3RC_pT}\right]. \tag{C.6}$$

Size of thermal is assumed to be directly proportional to its altitude. Radius $r_t = r_0 + 0.2 * Z$, r_0 is between 100m and 150 and z is altitude.

Typically inertia causes the thermal to ascend beyond the cross over altitude at which the temperature difference $T - T_\infty$ is zero. When air parcel will eventually start to descend the

entertainment effects on vertical acceleration continue in the same sense and thus when $w<0$;

$$\frac{\mathrm{dw}}{\mathrm{dt}} = \frac{2}{3}\left[g\frac{\Theta_v - \Theta_{v_\infty}}{\Theta_{v_\infty}} + \mu_t\omega^2\right]. \tag{C.7}$$

Appendix D

Fuel Saving Plots

In this appendix plots for loitering mode using a point mass model are presented.

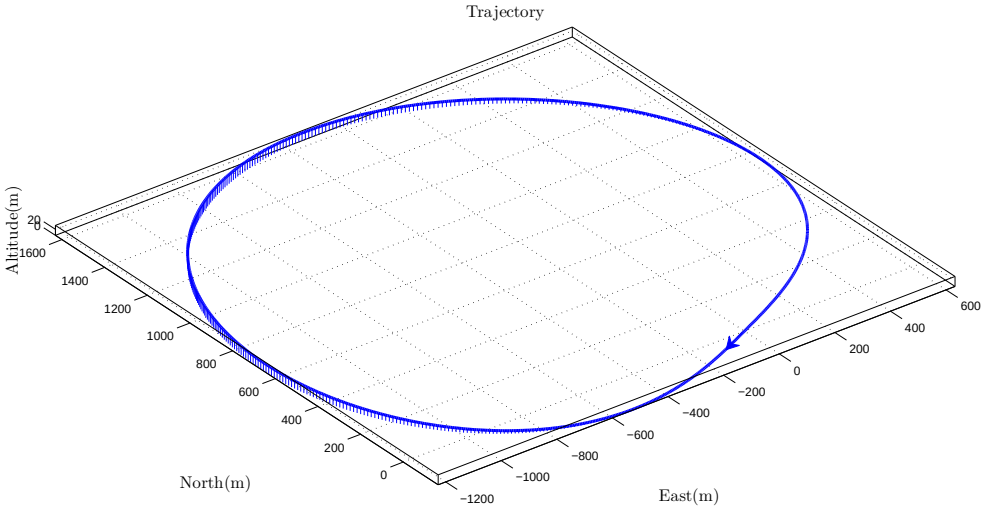

Figure D.1: Optimal trajectory for loitering mode

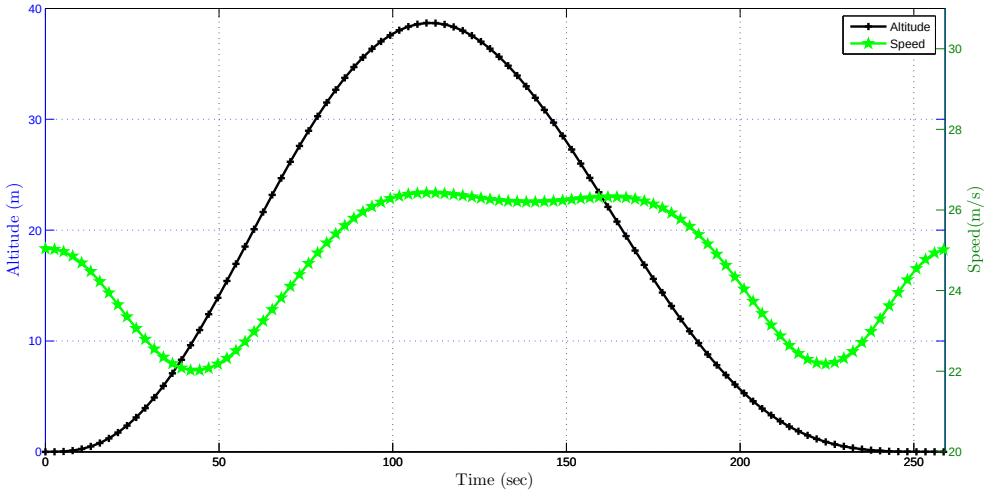

Figure D.2: Altitude and speed for loitering mode

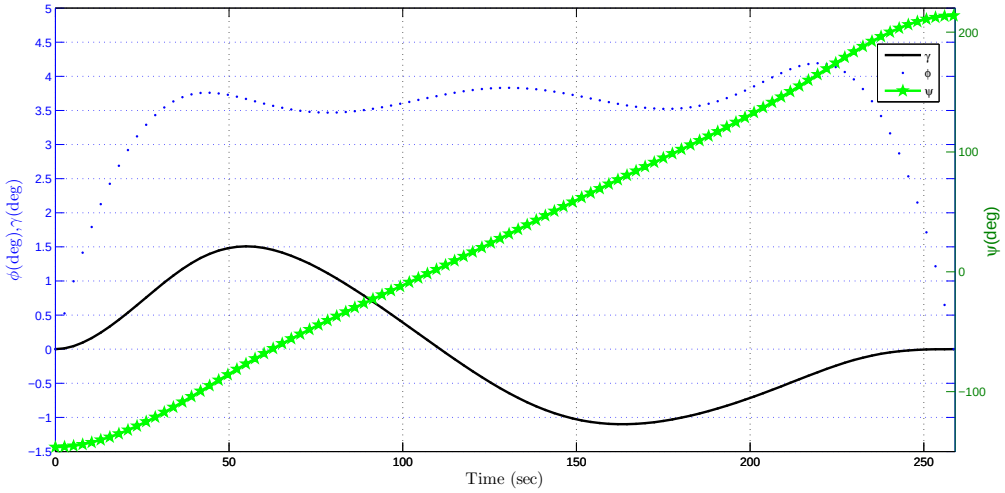

Figure D.3: Flight path, bank and heading angles for loitering mode

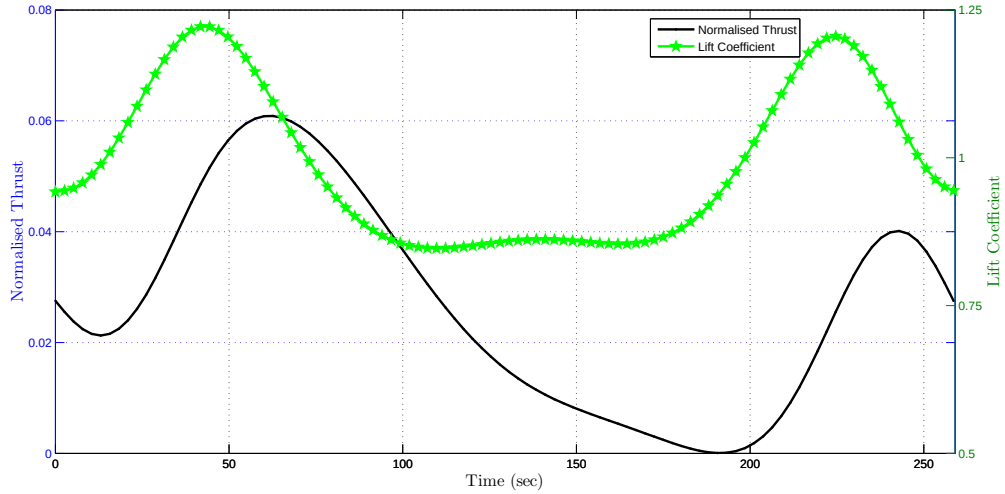

Figure D.4: Thrust and lift-coefficient for loitering mode

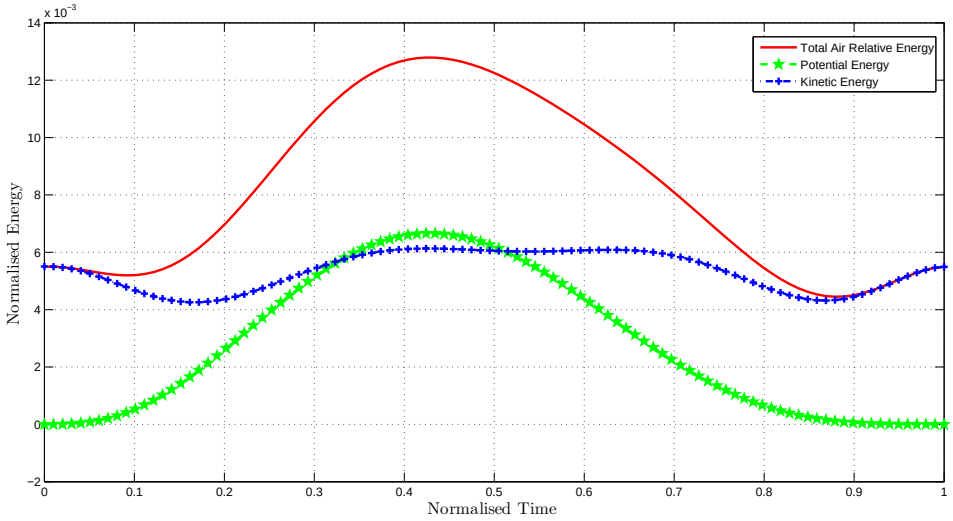

Figure D.5: Energy for loitering mode

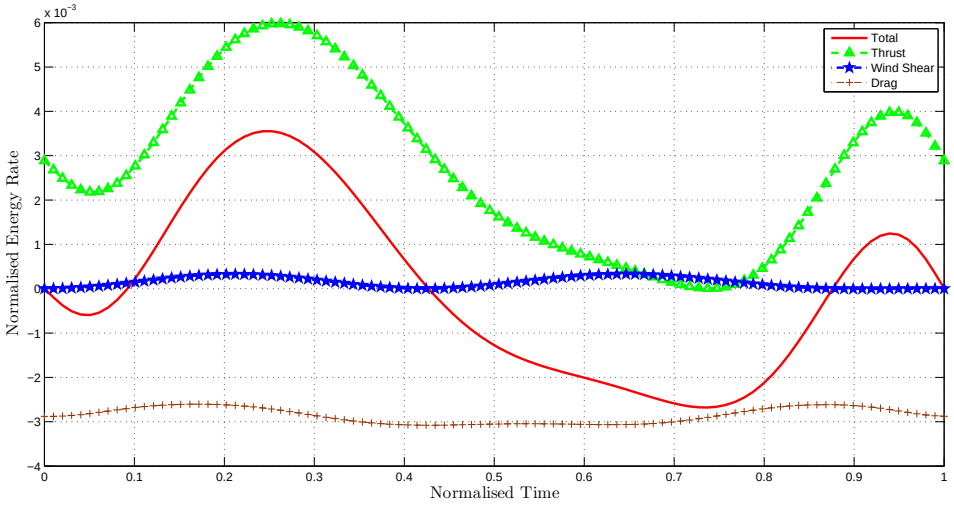

Figure D.6: Energy rate for loitering mode

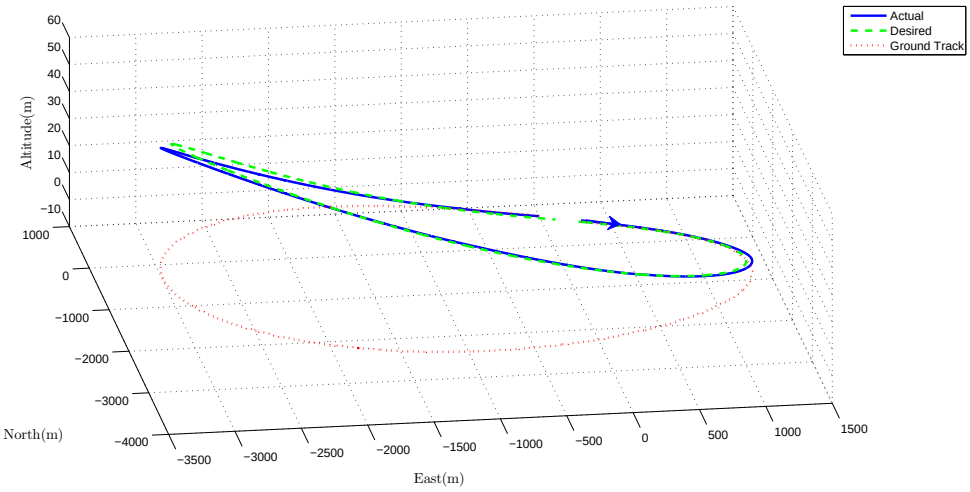

Figure D.7: Loitering trajectory tracking in 6DoF model

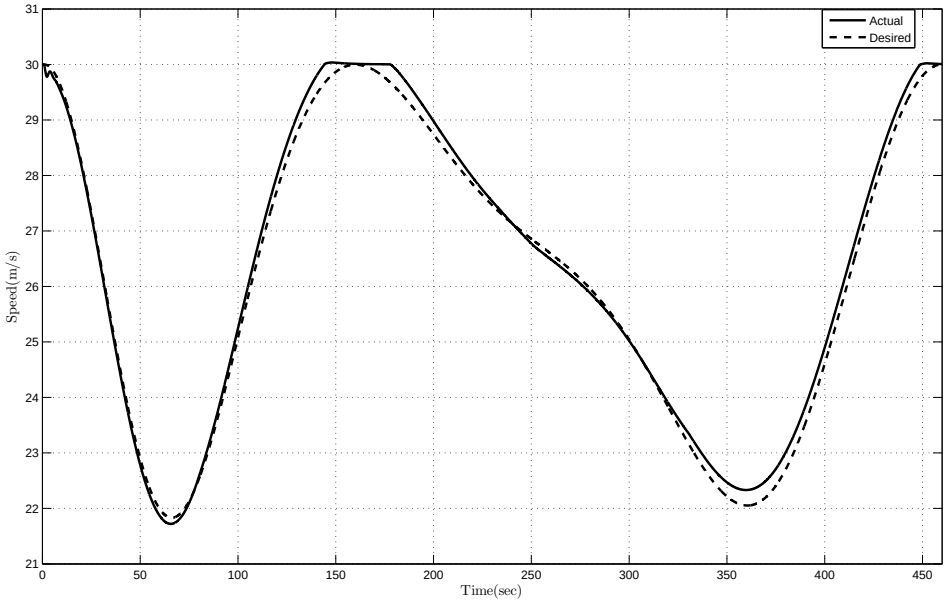

Figure D.8: Loitering mode speed 6DoF model

Appendix E

Conference Paper

In this appendix the Manchester control conference (UKACC 2008) paper on real-time trajectory generation techniques is presented that investigated dynamic soaring technique using a small UAV.

Real-time trajectory generation technique for dynamic soaring UAVs

Naseem Akhtar * **James F Whidborne** * **Alastair K Cooke** *

* *Department of Aerospace Sciences, Cranfield University, Bedfordshire MK45 0AL, UK. email:*n.akhtar@cranfield.ac.uk

Abstract: This paper addresses the problem of generating real time trajectories for the dynamic soaring of UAVs (unmanned aerial vehicles). The aircraft soar using the wind shear available over the oceans. The UAVs utilize the energy from low-altitude wind gradients to reduce fuel consumption. For a propeller driven UAV, a performance index is selected to minimize the average power required per cycle. The control problem is formulated by considering the equations of motion, operational constraints, initial conditions and terminal conditions that enforce a periodic flight. The differential flatness property of the equations of motion are used to transform the problem to the output space, which permits rapid solution using standard nonlinear programming. The results obtained are compared with those achieved for a collocation technique and a constrained optimization technique.

Keywords: Parametrization, real time trajectory generation, direct method, dynamic soaring, wind conditioning parameter, wind gradient, differential flatness, virtual arc, inverse dynamics.

NOTATION

β	Wind gradient.
K	Induced drag factor.
E_{max}	Aerodynamic efficiency.
C_L	Lift Coefficient.
C_D	Drag Coefficient.
C_{D_0}	Zero lift drag coefficient.
T	Thrust.
x, y, h	Position relative to Earth axis.
V	Velocity.
m	Mass.
g	Acceleration due to gravity.
γ	Flight path angle.
ϕ	Bank Angle.
ψ	Heading Angle.
$\bar{(\cdot)}$	Normalized states.
t_f	Final time.
n	Load factor.
$a_{x_{0\ldots7}}$	Coefficients of the polynomial.
τ	Virtual arc.
λ	Speed factor.
ρ	Air density.
$\bar{\rho}$	Normalized wind conditioning parameter.

1. INTRODUCTION

The extraction of energy from low-level wind gradients is called dynamic soaring [Zhao, 2004a]. This could be used to increase the endurance of UAVs by extracting energy from the velocity field in a similar manner to some sea birds. In a typical pattern of dynamic soaring a bird would descend with the prevailing wind to gain airspeed. On getting close to the sea surface, it turns into wind and begins to climb. Although the forward advance decreases due to the climb the bird maintains sufficient lift due to increased speed provided by the wind gradient. When the peak wind velocity is reached the bird changes direction to descend and starts the process again. It is possible, if the wind gradient is steep, for the bird to extract sufficient energy to maintain flight without flapping [Zhao, 2004a].

Optimal control methods have been used by Zhao [2004a] to minimize either the average power per cycle or the level of constant power required by a propeller driven UAV. By formulating a non-linear optimal control problem [Zhao, 2004a,b] has generated solutions for both linear and nonlinear wind gradient profiles with a three-dimensional point mass model. In the case of a linear wind profile [Zhao, 2004a], through normalization of the UAV equations of motion, a single parameter was defined that represents the relative wind effect on the UAV. Performance indices were selected to minimize the average power required per cycle with either variable or constant power. These optimal control problems were converted into parameter optimization with a collocation technique and solved numerically.

Sachs & da Costa [2003] has also studied the problem of energy extraction from wind shear using optimization techniques. Deittert et al. [2006] includes a review of the art of dynamic soaring. The dynamic soaring equations are derived and solved and the results are discussed with respect to generic UAV models.

The optimization approach used in this paper is based on the Direct Method of Taranenko [Yakimenko, 2000]. This method permits the solution of trajectory optimization problems in the output space. Control histories are obtained by dynamic inversion without any requirement to solve the integral equations. It should be noted that the use of a virtual time argument allows the temporal

⋆ This work was supported by BAE Systems and EPSRC.

and spacial requirements to be decoupled. As the method is very efficient it is able to find near-optimal trajectories rapidly enough to allow real-time implementation [Yakimenko, 2000] thereby allowing the exploitation of dynamic soaring for fuel efficient UAV operations.

In the next section, the vehicle and wind models are given and in Section 3 the inverse dynamic equations are presented. Section 4 describes the Direct Method and its application to the dynamic soaring problem. In Section 5 the results are presented and compared with those from Zhao [2004a] and some obtained using a simple constrained optimization approach.

2. DYNAMIC SOARING MODEL

In a wind gradient field, the horizontal component increases with altitude and wind gradients occur across various altitude ranges. Typically, reasonably stable conditions exist close to the sea surface with the wind velocity nearly zero at the surface and increasing gradually with altitude. In this paper only horizontal wind is considered. It is assumed that this component is static being a function of altitude only. The linear wind profile can be described as:

$$W_x(h) = \beta h. \tag{1}$$

The values of β for various wind conditions are defined in Zhao [2004a]. The UAV equations can be represented by a three dimensional point mass model in a stationary flat earth reference system [Zhao, 2004a]. The equations of motion are given by:

$$m\dot{V} = T - D - mg\sin\gamma - m\dot{W}_x\cos\gamma\sin\psi \tag{2}$$
$$mV\cos\gamma\dot{\psi} = L\sin\phi - m\dot{W}_x\cos\psi \tag{3}$$
$$mV\dot{\gamma} = L\cos\phi - mg\cos\gamma + m\dot{W}_x\sin\gamma\sin\psi \tag{4}$$
$$\dot{h} = V\sin\gamma \tag{5}$$
$$\dot{x} = V\cos\gamma\sin\psi + W_x(h) \tag{6}$$
$$\dot{y} = V\cos\gamma\cos\psi \tag{7}$$

It is assumed that the mass is constant. Note that the state variables are $[V, \psi, \gamma, x, y, h]$ and the control variables are $[C_L, \phi, T]$. Now the lift and drag forces are represented as:

$$L = \frac{1}{2}\rho V^2 S C_L \tag{8}$$
$$D = \frac{1}{2}\rho V^2 S C_D \tag{9}$$

and

$$C_D = C_{D_0} + K C_L^2 \tag{10}$$

The induced drag factor, K, can be determined from the aerodynamic efficiency E_{max} and the zero lift drag coefficient C_{D_0} as:

$$K = \frac{1}{4E_{max}^2 C_{D_0}}, \tag{11}$$

where

$$E_{max} = \left(\frac{C_L}{C_D}\right)_{max} = \left(\frac{C_L}{C_{D_0} + KC_L^2}\right)_{max}. \tag{12}$$

The above equations of motion are then normalized as follows:

$$\bar{V} = \frac{\beta}{g}V, \qquad \bar{x}, \bar{y}, \bar{h} = \frac{\beta^2}{g}(x, y, h), \tag{13}$$
$$\bar{T} = \frac{T}{mg}, \qquad \tau = \beta t, \tag{14}$$

and we have

$$(\cdot)' = \frac{d(\cdot)}{d\tau} = \frac{1}{\beta}\frac{d(\cdot)}{dt}. \tag{15}$$

The normalized equations of motion are then obtained as [Zhao, 2004a]

$$\bar{V}' = \bar{T} - \bar{\rho}\bar{V}^2(C_{D_0} + KC_L^2) - \sin\gamma - \bar{V}\sin\gamma\cos\gamma\sin\psi \tag{16}$$
$$\psi' = \bar{\rho}\bar{V}C_L\cos\mu - \tan\gamma\cos\psi \tag{17}$$
$$\gamma' = \bar{\rho}\bar{V} - \frac{\cos\gamma}{\bar{V}} + \sin^2\gamma\sin\psi \tag{18}$$
$$\bar{h}' = \bar{V}\sin\gamma \tag{19}$$
$$\bar{x}' = \bar{V}\cos\gamma\sin\psi + \bar{h} \tag{20}$$
$$\bar{y}' = \bar{V}\cos\gamma\cos\psi \tag{21}$$

Note that for presentation of the simulation results, the normalized equations are multiplied by t_f.

The wind parameter is defined as

$$\bar{\rho} = \frac{\rho g^2}{2(mg/S)\beta^2}. \tag{22}$$

3. DIFFERENTIAL FLATNESS

Differential flatness is the property of the system that allows to describe state and controls in terms of outputs and their derivatives. For a system to be differentially flat and therefore possessing a flat output it requires a set of variables such that:

(1) Every system variable may be expressed as a function of the output y;
(2) Conversely every component of y may be expressed as a function of the system variables and of a finite number of time derivatives.

By manipulating equations of motion, the state and input vector can be expressed as a function of the output vector. The outputs of the system are x, y, and h and the inputs are $\bar{T}$, C_L and ϕ. This gives the inverse dynamics as:

$$V = \sqrt{\dot{x}^2 + (\dot{y} - \beta\dot{h})^2 + \dot{h}^2} \tag{23}$$
$$\gamma = \arcsin(\dot{h}/V) \tag{24}$$
$$\psi = \text{atan2}((\dot{y} - \beta m\dot{h}), \dot{x}) \tag{25}$$
$$\dot{\gamma} = \frac{\ddot{h}}{\sqrt{V - \dot{h}^2}} - \frac{\dot{h}(\dot{x}\ddot{x} + (\dot{y} - \beta\dot{h})(\ddot{y} - \beta\ddot{h})) + \dot{h}\ddot{h}}{V^2\sqrt{V - \dot{h}^2}} \tag{26}$$

$$\dot{\psi} = \frac{\dot{x}(\ddot{y} - \beta\ddot{h}) - (\dot{y} - \beta\dot{h})\ddot{x}}{\dot{x} + (y - \beta\dot{h})^2} \quad (27)$$

$$\bar{T} = \bar{V}' + \rho\bar{V}^2(C_{D0} + KC_2^2) + \sin\gamma + \bar{V}\sin\gamma\cos\gamma\sin\psi \quad (28)$$

$$\phi = \arctan\left(\cos\gamma\frac{\psi' + \tan\gamma\cos\gamma}{\gamma' + (\cos\gamma)/\bar{V} - \sin^2\gamma\sin\psi}\right) \quad (29)$$

$$C_L = \frac{\bar{V}\gamma' + \cos\gamma - \bar{V}\sin^2\gamma\sin\psi}{\bar{\rho}\bar{V}^2\cos\phi} \quad (30)$$

4. THE DIRECT METHOD OF TARANENKO

This is a non-linear constrained optimization method where some reference polynomials are determined by the boundary conditions. The speed profile can be separated from trajectory by introduction of a virtual arc instead of time. The inequality constraints are direct functions of the output due to differential flat properties of the system, which helps to accelerates the process for on board implementation. For further details, see Yakimenko [2000] and Whidborne et al. [2008].

4.1 Parametrization

In the parametrization process the polynomial coefficients are the varied parameters of the optimization algorithm. and can be determined analytically [Etchemendy, 2007]. The degree of the reference polynomials is given by the number of boundary conditions that have to be met to calculate all the coefficients. The minimum degree of the polynomial must be equal to $n = d_0 + d_f + 1$ with $d_{0,f}$ being the maximum order of the time derivative of the UAV coordinates. If the initial and final acceleration coordinates are preset ($d_0 = d_f = 2$), the reference polynomial will be fifth order. An addition of one fictive boundary condition ($x'''_{o,f}$) gives a more flexible reference trajectory. These fictive boundary values are added as additional optimization variables. They are free to vary to find more solutions that are near-optimal. In this case $n = 7$ and this gives us a total of 24 coefficients to calculate. The coefficients associated with the x coordinate are:

$$a_{x_0} = x_0 \quad (31)$$

$$a_{x_1} = x'_0 \quad (32)$$

$$a_{x_2} = x''_0 \quad (33)$$

$$a_{x_3} = x'''_0 \quad (34)$$

$$a_{x_4} = -\frac{2x'''_f + 20x'''_0}{\tau_f} + \frac{30x''_f - 60x''_0}{\tau''_{f^2}} - \frac{180x'_f + 240x'_0}{\tau_{f^3}} + 420\frac{x_f - x_0}{\tau_{f^4}} \quad (35)$$

$$a_{x_5} = -\frac{10x'''_f + 20x'''_0}{\tau_{f^2}} + \frac{140x''_f - 200x''_0}{\tau''_{f^3}} - \frac{780x'_f + 900x'_0}{\tau_{f^4}} + 420\frac{1020x_f + 1080x_0}{\tau_{f^5}} \quad (36)$$

$$a_{x_6} = -\frac{15x'''_f + 20x'''_0}{\tau_{f^3}} + \frac{195x''_f - 225x''_0}{\tau''_{f^4}} - \frac{1020x'_f + 1080x'_0}{\tau_{f^5}} + 2100\frac{x_f - x_0}{\tau_{f^6}} \quad (37)$$

$$a_{x_7} = -7\frac{x'''_f + x'''_0}{\tau_{f^4}} - 84\frac{x''_f - x''_0}{\tau''_{f^5}} + 420\frac{x'_f + x'_0}{\tau_{f^5}} + 420\frac{x_f - x_0}{\tau_{f^6}} - 840\frac{x_f - x_0}{\tau_{f^7}} \quad (38)$$

where τ_f is the final value of the individual arc, and is a free parameter of the optimization. The reference function is then

$$x(\tau) = \sum_{k=0}^{7}\frac{a_{xk}\tau^k}{\max(1, k(k-1))}; \quad (39)$$

An identical process can be performed for the two other coordinates, y and h.

4.2 The Virtual Arc

The use of a virtual arc, τ, enables the speed profile to be separated from the trajectory [Etchemendy, 2007]. This allows the velocity to be varied independently from the reference trajectory so that a UAV can follow the same trajectory but with different speed histories. If we set $\tau = t$ then the speed is fixed and equal to:

$$V = \sqrt{\dot{x}^2 + \dot{y}^2 + \dot{h}^2}. \quad (40)$$

The introduction of a virtual arc linked to the time by the variable speed parameter, λ, allows us to vary speed along the trajectory. The speed is then:

$$V = \lambda\sqrt{x'^2 + y'^2 + h'^2}. \quad (41)$$

4.3 The Optimization Problem

The differential flatness properties allow us to set the optimization problem in output space [Cowling et al., 2007]:

$$\min\left\{\Phi : y(t) \in \mathbb{R}^4, t \in [0, t_f]\right\} \quad (42)$$

such that:

$$\dot{y} - g(y) = 0 \quad (43)$$

$$\dot{y} - g(y_0) = 0 \quad (44)$$

$$\dot{y} - g(y_f) = 0 \quad (45)$$

$$d(y) \leq 0. \quad (46)$$

where Φ is the cost function and represents the value to be minimized and $d(y)$ represents the constraints. The computation time is reduced as d is only a function of the output. The problem has been programmed in MatLab™ using the parametrization described and solved with the optimization function `fmincon` with a cost function defined as:

$$\Phi(C_L, \mu, \bar{T}, \bar{V}_0, \psi_0, \tau_f) = \frac{1}{\tau_f}\int_0^{\tau_f}\bar{T}\bar{V}d\tau \quad (47)$$

4.4 Constraints

Some constraints are specified to avoid singularities in the dynamic inversion equations whereas others are imposed to represent real-world limitations such as available control power and minimum flight speed (stall). Possible singularities are:

$$\cos(\gamma) = 0 \quad (48)$$

$$\cos(\phi) = 0 \quad (49)$$

$$g\cos(\gamma) + V\dot{\gamma} = 0. \quad (50)$$

Thus the constraints are:

$$-90^o < \phi, \gamma < 90^o \quad (51)$$
$$60 \text{ m/s } < V < 123 \text{ m/s} \quad (52)$$
$$-30^o < \gamma < 30^o \quad (53)$$
$$\bar{T} > 0 \quad (54)$$
$$0.6 < n < 1.0 \quad (55)$$

4.5 Inverse dynamics

The numerical solution is obtained by splitting the virtual arc $[0,\ \tau_f]$ into N equally placed points [Cowling et al., 2007] with an interval of:

$$\Delta\tau = \frac{\tau_f}{N-1} \quad (56)$$

With $\tau_0 = 0$ the next value of the virtual arc is computed as:

$$\tau_j = \tau_{j-1} + \Delta\tau \text{ for } j = 1 \ldots N \quad (57)$$

The reference polynomials are found as polynomials of τ and these polynomials only depend on the boundary conditions. The initial conditions are converted from time derivatives to virtual arc derivatives using the following relationship:

$$\lambda(\tau) = \frac{d\tau}{dt} \quad (58)$$

This gives us the following relationships:

$$\dot{x} = \frac{dx}{d\tau}\frac{d\tau}{dt} = \lambda x' \quad (59)$$
$$\ddot{x} = \frac{d((\lambda x')}{d\tau}\frac{d\tau}{dt} = \lambda^2 x'' + \lambda\lambda' x' \quad (60)$$
$$\dddot{x} = \frac{d(\lambda^2 x'' + \lambda\lambda' x')}{d\tau}\frac{d\tau}{dt} \quad (61)$$
$$= \lambda^3 x''' + 3\lambda^2\lambda' x'' + x'(\lambda^2\lambda'' + \lambda\lambda'^2). \quad (62)$$

After rearrangement we get expressions for the virtual arc's first and second derivatives of the coordinates:

$$x' = \dot{x}\lambda^{-1} \quad (63)$$
$$x'' = \ddot{x}\lambda^{-2} - \dot{x}\lambda'\lambda^{-1}. \quad (64)$$

For the boundary, the values of:

$$\lambda_{0,f} = V_{0,f} \quad (65)$$
$$\lambda'_{0,f} = \dot{V}_{0,f} V_{0,f}^{-1} \quad (66)$$

may be chosen but the scaling of λ does not really matter as allowing the virtual speed and the actual speed to be equal at the boundaries just implies that the virtual arc τ_f will be of the order of the path length. The current time is computed as follows:

$$t_j = t_{j-1} + \Delta t_{j-1} \quad (67)$$

where:

$$\Delta t_{j-1} = 2\frac{\sqrt{(x_j - x_{j-1})^2 + (y_j - y_{j-1})^2 + (h_j - h_{j-1})^2}}{V_j - V_{j-1}} \quad (68)$$

Therefore the current value of the speed factor is:

$$\lambda_j = \frac{\Delta\tau}{\Delta t_{j-1}}. \quad (69)$$

5. RESULTS

Figures 1 to 9 show the optimal UAV state and control variables. Note that all are within constraints. Figure 1 shows a three dimensional view of the minimum variable power dynamic soaring flight trajectory for β =0.02965/sec which corresponds to $\bar{\rho} = 140$, a wind conditioning parameter that describes the strength of the wind and is defined by (22). The zero lift drag coefficient, C_{D_0}, was set to 0.01 and E_{max} =25 [Zhao, 2004a].

The UAV would first climb into the wind with a positive climbing angle to trade kinetic energy for potential energy. It loses speed as shown in Figure 2 while gaining altitude. After reaching the maximum altitude possible within the constraints, it then dives along the wind using a negative flight path angle to trade potential energy for speed. During simulations it was noted that as the wind condition parameter $\bar{\rho}$ increased, the peak altitude decreased.

The airspeed reaches a minimum at the peak altitude and a maximum at the lowest altitude, see Figure 2. The lowest airspeed corresponds to the peak lift coefficient and maximum bank angles (Figures 5 and 9). The peak normalized thrust occurs around the maximum velocity and is much lower or close to zero for the rest of the cycle, see Figure 4.

This problem has been solved previously by the author using a constrained optimization method. In this case, a solution to the optimization problem was achieved in 28 seconds however using the method described in this paper reduced the solution time to eight seconds. No data was presented in Zhao [2004a] regarding the time taken to optimize the trajectory. However it was stated that the method was not applicable to real time trajectory generation applications suggesting that the solution time was significant.

The peak value of normalized thrust obtained in our case is 0.06 as compared to 0.25 for Zhao [2004a]. Note that the average normalized thrust used was 0.0085.

6. CONCLUSIONS

The direct method method has a clear advantage over the method of Zhao [2004a] because it could be implemented in real time as the optimization time is just eight seconds compared to a trajectory loop time of 176 seconds. This short time would allow computation of the next loop during the current trajectory loop. Furthermore it predicts a much lower peak thrust requirement suggesting that the UAV will require a smaller sized engine. No direct comparison can be made of average thrust as this was absent in Zhao [2004a].

Note that results in Zhao [2004a] showed a greater distance in the x direction and also a greater height. The direct method can achieve similar results by increasing the thrust usage.

Results have been obtained for various other values of the wind condition parameter, $\bar{\rho}$, for both the minimum variable power and minimum constant power cost functions. Other cost functions that have been considered are

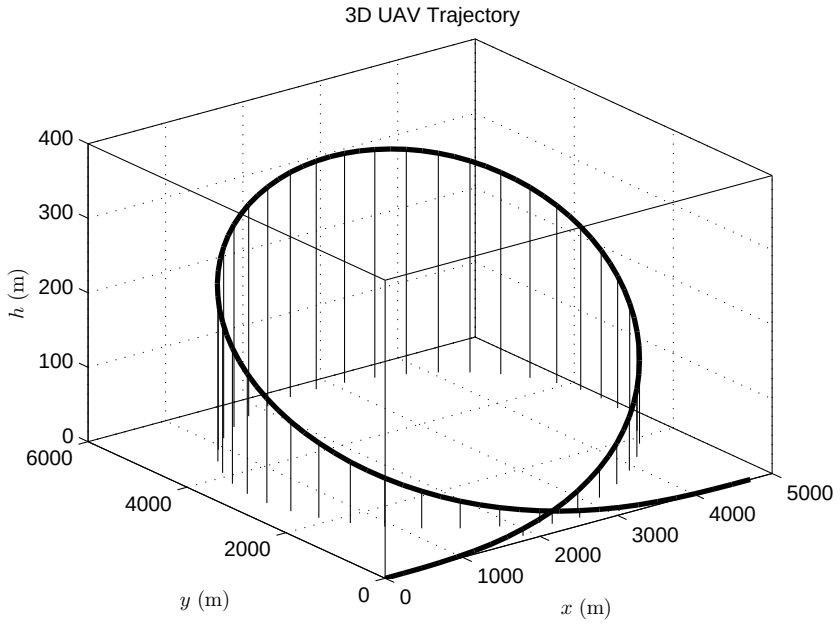

Fig. 1. Optimal tajectory for minimum peak power problem

maximum height and minimum time, but the results are not presented here.

REFERENCES

I.D. Cowling, O.A. Yakimenko, J.F. Whidborne, and A.K. Cooke. A prototype of an autonomous controller for a quadrotor UAV. *Proc. European Contr. Conf. 2007*, Kos, Greece, July 2007.

M. Deittert, C. Toomer, A.G. Pipe. Biologically inspired UAV propulsion. *21st Bristol Conference on UAVS*, April 2006.

M. Etchemendy. *Flight Control and Optimal Path Planning for UAVs*, MSC Thesis, Cranfield University, 2007.

G. Sachs and O. da Costa. Optimization of Dynamic Soaring at Ridges. *AIAA Atmospheric Flight Mechanics Conference and Exhbit*, Austin, Texas, August 2003.

J.F. Whidborne, I.D. Cowling, O.A. Yakimenko. A Direct Method for UAV Guidance and Control. *23rd Bristol Conference on UAVS*, April 2008.

O.A. Yakimenko. Direct method for rapid prototyping of near-optimal aircraft trajectories. *J. Guid. Control Dynam.*, 23(5):865–875, 2000.

Y.J. Zhao. Minimum fuel powered dynamic soaring of unmanned aerial vehicles utilizing wind gradients. *Optimal Control Applications and Methods*, 25:211-233, 2004a.

Y.J. Zhao. Optimal Dynamic Soaring. Optimal Control Applications and Methods. *Optimal Control Applications and Methods*, 25:67-89, 2004b.

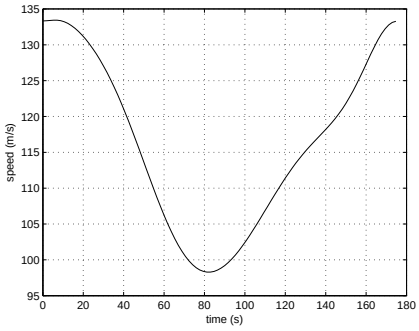

Fig. 2. Speed profile for minimum peak power problem

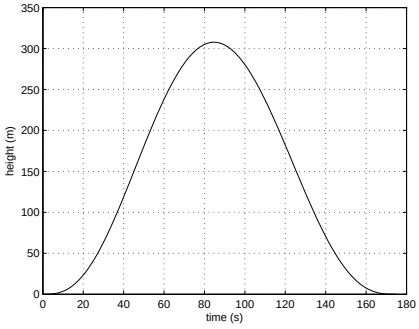

Fig. 3. Height profile for minimum peak power problem

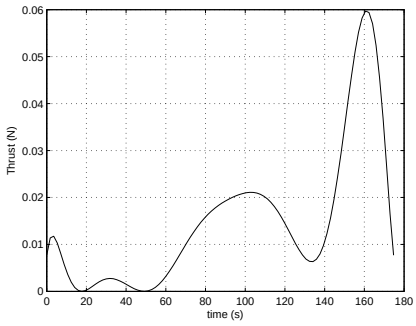

Fig. 4. Thrust profile for minimum peak power problem

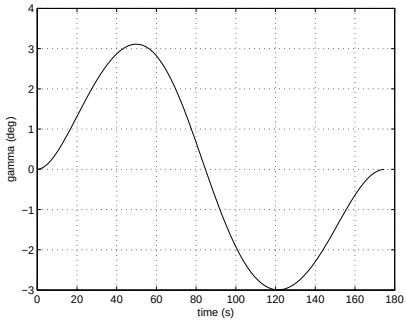

Fig. 7. Climbing angle profile for minimum peak power problem

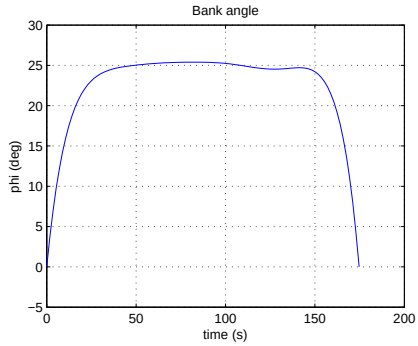

Fig. 5. Bank angle profile for minimum peak power problem

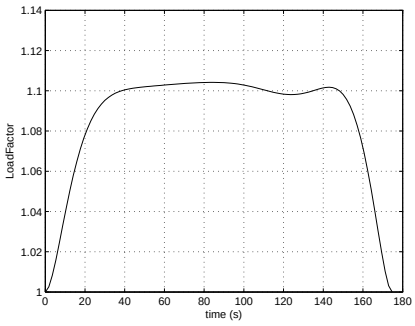

Fig. 8. Load factor profile for minimum peak power problem

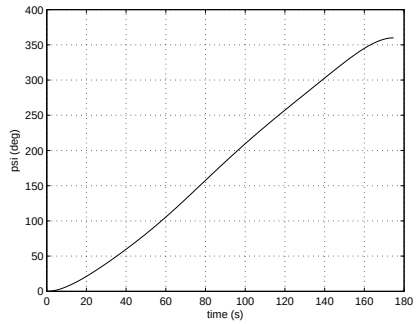

Fig. 6. Heading angle profile for minimum peak power problem

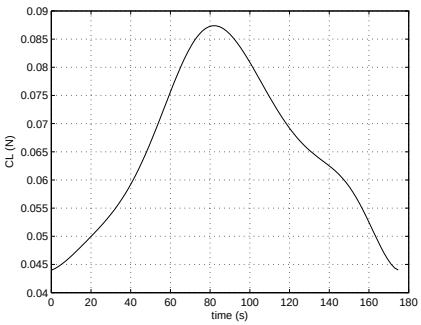

Fig. 9. Lift coefficient profile for minimum peak power problem

Appendix F

SIMULINK Models

In this appendix block diagram of the Simulink program used for thermal soaring and wind shear is shown along with the blocks of submodules. Figure F.1 shows the inputs to various blocks in the Simulink program, including aerodynamics, equations of motion, air data, navigation, angular motion transformation, forces due to gravity, power plant, wind addition, wind estimation and along and off track errors. The inputs to each block are listed on the left side and outputs to the right side.

In the navigation block the body velocity components are converted to earth rates and outputs are integrated to get position in north, east and altitude. The air data block outputs airspeed, angle of attack, side slip angle and dynamic pressure. The gravity module determines body forces due to weight and moments due to cg offset.

Figures F.2 to **??** show the submodules of the aerodynamic module. The inputs and the outputs of the submodules are labeled on left and right side respectively. The moments and forces generated by wing and tailplane, lateral forces generated by the fin, tailplane contribution, fuselage drag, spoiler and fin drag submodules are shown.

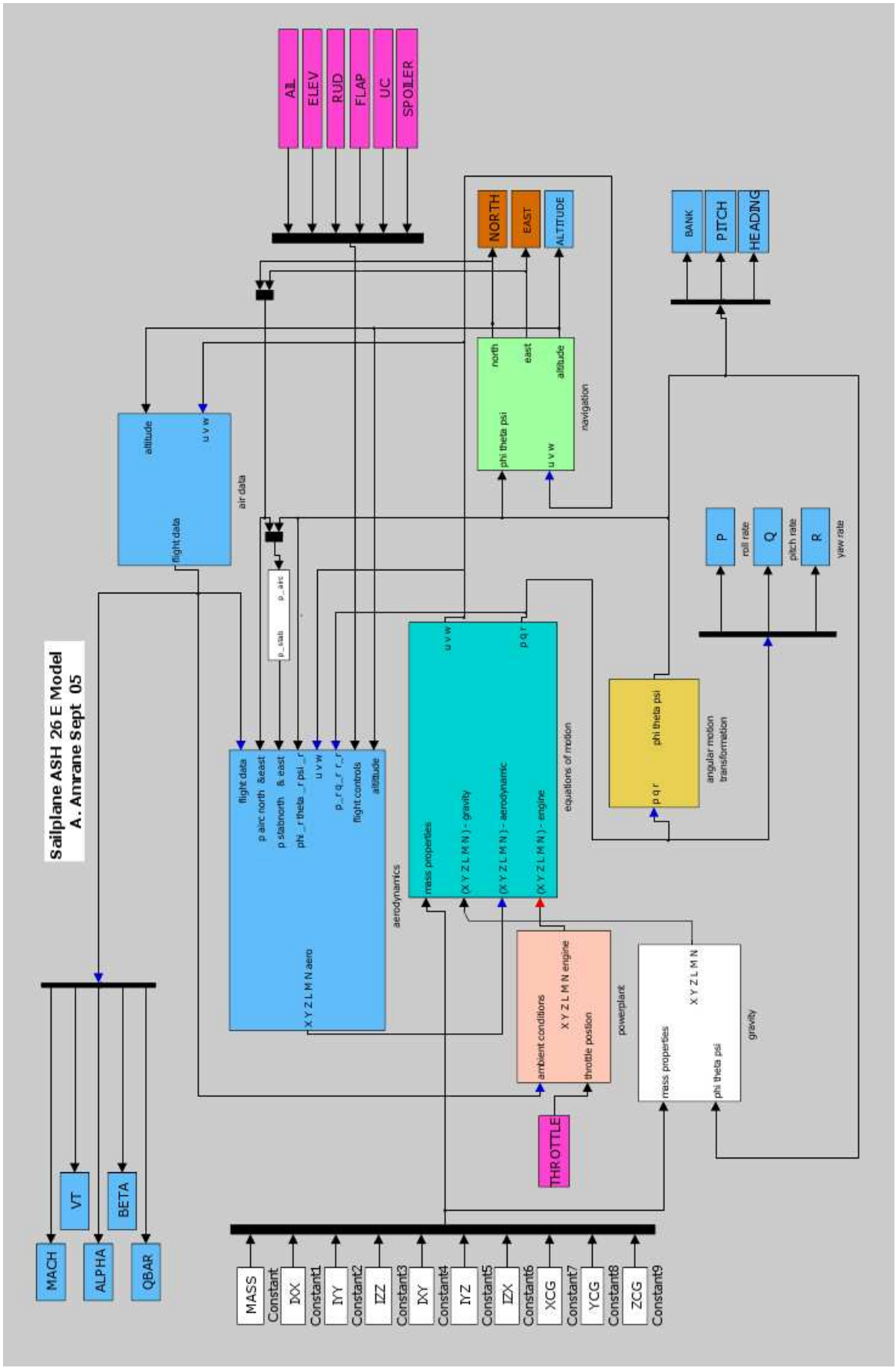

Figure F.1: The blocks of the Simulink program

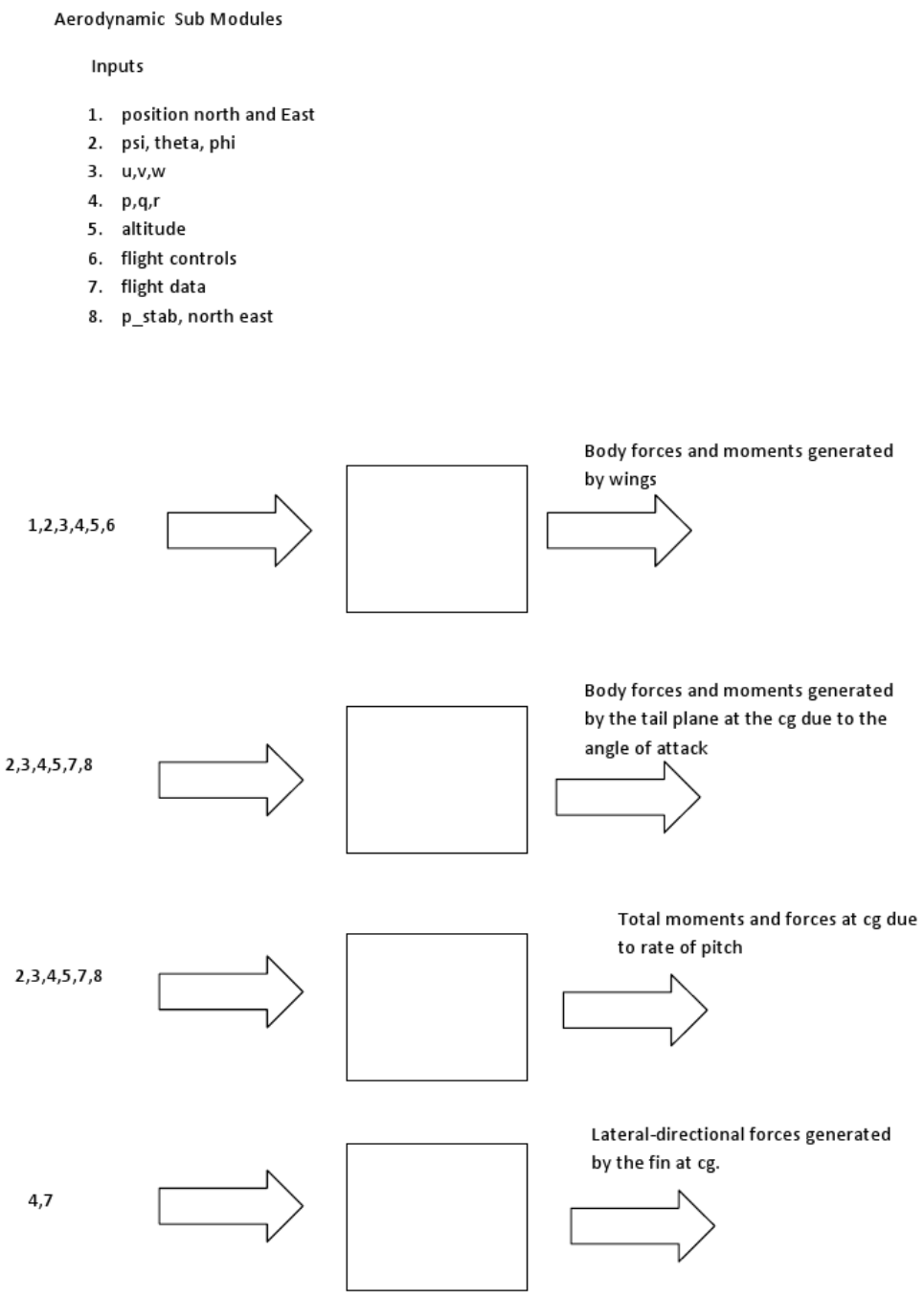

Figure F.2: Submodules 1 of aerodynamic block

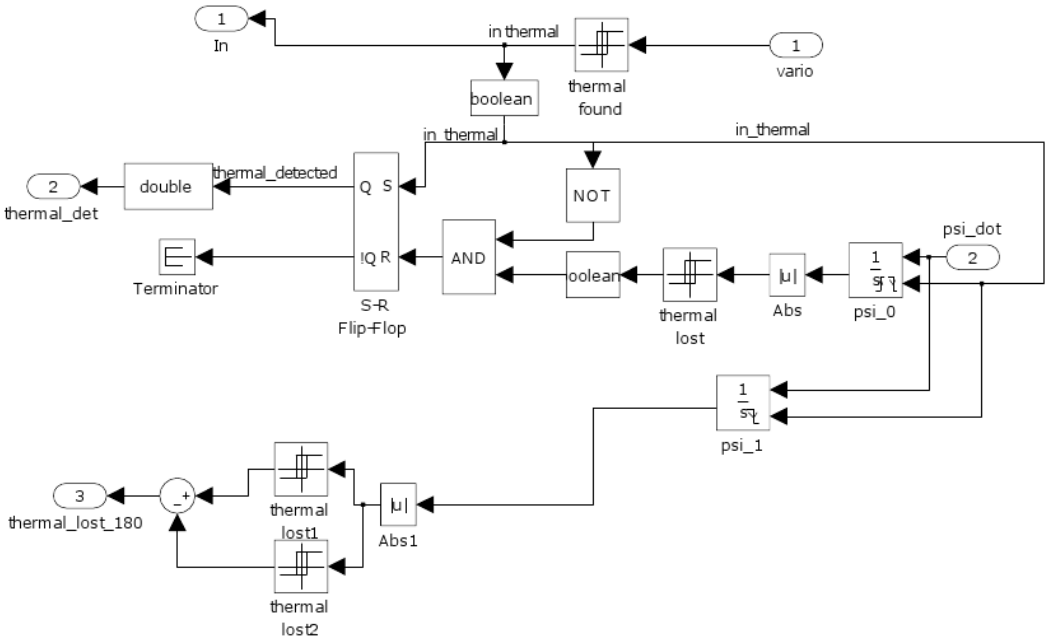

Figure F.3: Thermal detection logic

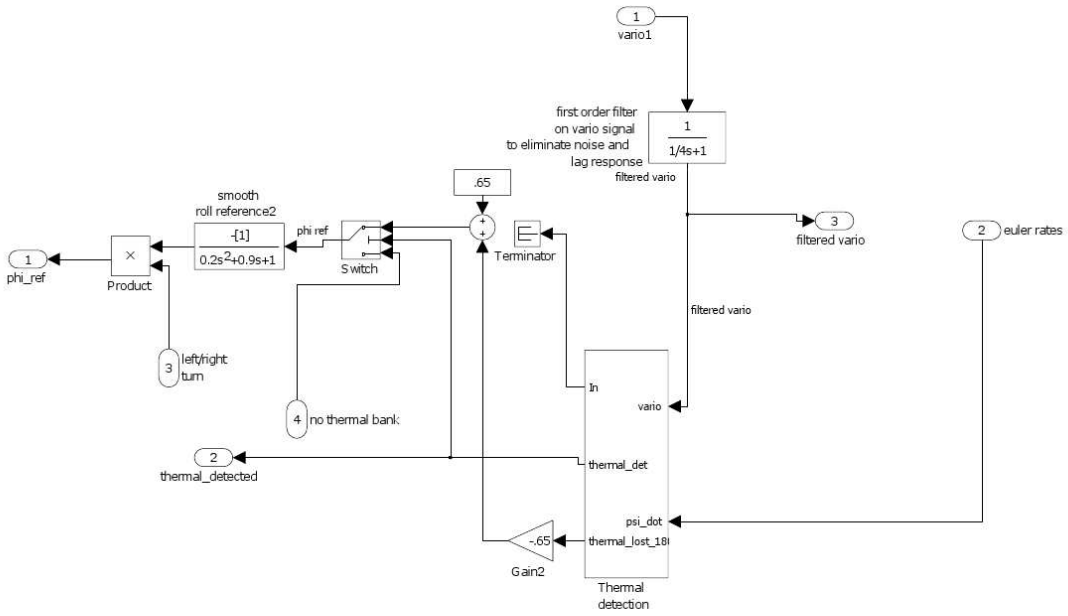

Figure F.4: Bank command generation block

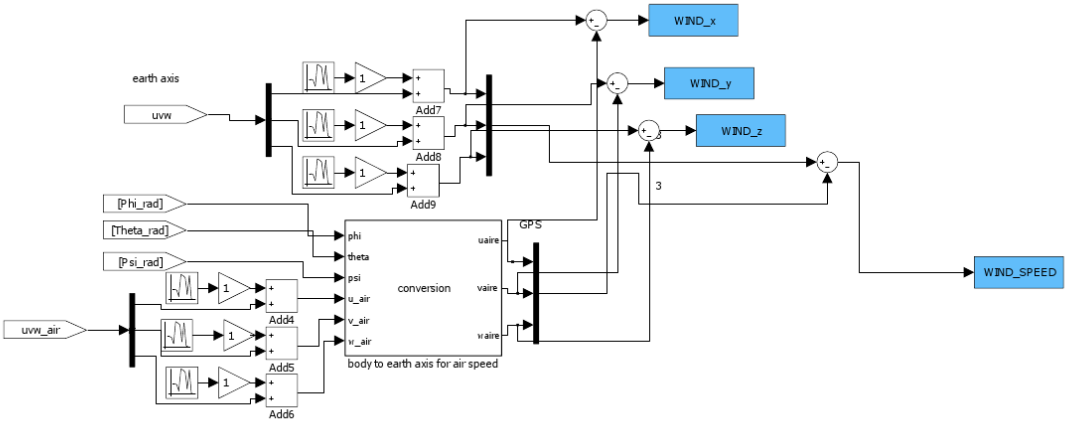

Figure F.5: Wind speed estimation block